Analysis and Modeling of Foundry Compatible Programmable Metallization Cell Materials

by

Mehmet Bugra Balaban

A Dissertation Presented in Partial Fulfillment
of the Requirements for the Degree
Doctor of Philosophy

Approved April 2020 by the
Graduate Supervisory Committee:

Michael Kozicki, Chair
Hugh Barnaby
Dragica Vasileska
Michael Goryll

ARIZONA STATE UNIVERSITY

May 2020

ABSTRACT

Programmable Metallization Cell (PMC) devices are, in essence, redox-based solid-state resistive switching devices that rely on ion transport through a solid electrolyte (SE) layer from anode to cathode. Analysis and modeling of the effect of different fabrication and processing parameter/conditions on PMC devices are crucial for future electronics. Furthermore, this work is even more significant for devices utilizing back-end-of-line (BEOL) compatible materials such as Cu, W, their oxides and SiO_x as these devices offer cost effectiveness thanks to their inherent foundry-ready nature. In this dissertation, effect of annealing conditions and cathode material on the performance of Cu-SiO_x vertical devices is investigated which shows that W-based devices have much lower forming voltage and initial resistance values. Also, higher annealing temperatures first lead to an increase in forming voltage from 400 °C to 500 °C, then a drastic decrease at 550 °C due to Cu island formation at the Cu/SiO_x interface. Next, the characterization and modeling of the bilayer Cu_2O/Cu-WO_3 obtained by annealing the deposited Cu/WO_3 stacks in air at BEOL-compatible temperatures is presented that display unique characteristics for lateral PMC devices. First, thin film oxidation kinetics of Cu is studied which show a parabolic relationship with annealing time and an activation energy of 0.70 eV. Grown Cu_2O shows a cauliflower-like morphology where feature size on the surface increase with annealing time and temperature. Then, diffusion kinetics of Cu in WO_3 is examined where the activation energy of diffusion of Cu into WO_3 is calculated to be 0.74 eV. Cu was found to form clusters in the WO_3 host which was revealed by imaging. Moreover, using the oxidation and diffusion analyses, a Matlab model is established for modeling the bilayer for process and annealing-condition optimization. The model is built to produce the

resulting Cu_2O thickness and Cu concentration in Cu-WO_3. Additionally, material characterization, preliminary electrical results along with modeling of lateral PMC devices utilizing the bilayer is also demonstrated. By tuning the process parameters such as deposited Cu thickness and annealing conditions, a low-resistive Cu_2O layer was achieved which dramatically enhanced the electrodeposition growth rate for lateral PMC devices.

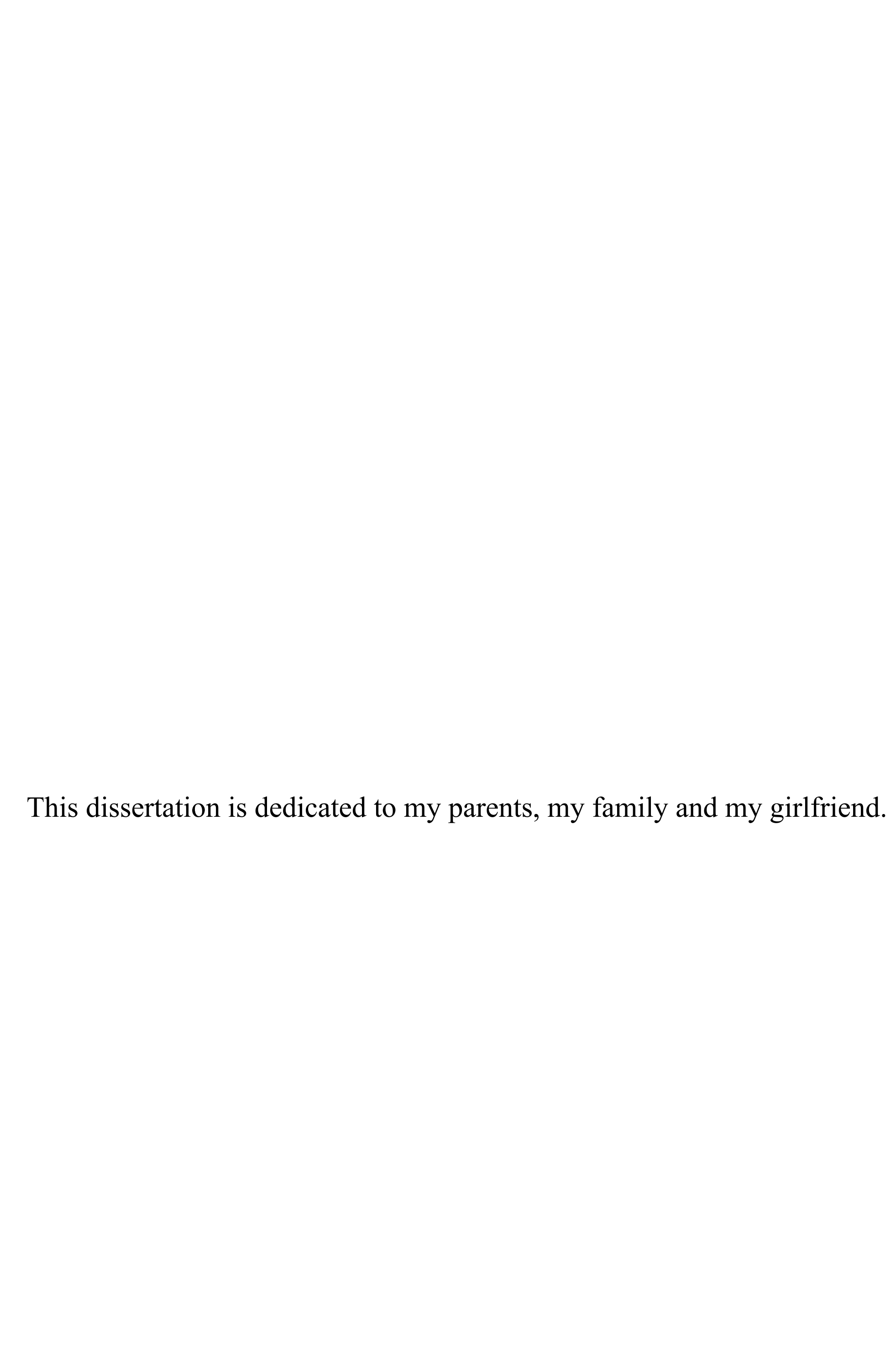

This dissertation is dedicated to my parents, my family and my girlfriend.

ACKNOWLEDGMENTS

I would like to sincerely thank my supervisor, Prof. Michael N. Kozicki, for his outstanding guidance on my Ph.D. research, his mentorship and his support throughout my years at Arizona State University (ASU). I am particularly grateful for the degree of freedom I was given to pursue my interest in material analysis. I would also like to thank Prof. Hugh J. Barnaby and Prof. Yago Gonzalez-Velo whom I see as co-advisors. Their invaluable support and encouragement made my years at ASU special.

I am also thankful to my other committee members, Prof. Dragica Vasileska and Prof. Michael Goryll, for their suggestions and interest in my research.

I would also like to thank the funding agencies, Arizona Board of Regions and Air Force Research Labs, for their financial support that made the work done by our research group possible.

I would also like to thank my colleagues/friends, whom I had the pleasure to work with, Dr. Weijie Yu, Dr. Debayan Mahalanabis, Dr. Adnan Mahmud, Dr. Runchen Fang, Dr. Wenhao Chen, Dr. Jennifer Taggart, Ninad Chamele, Smitha Swain, Arshey Patadia, Anand Krishnan, Priyanka Apsangi, Kiraneswar Muthuseenu and many others for their support, their teamwork, and the pleasant research environment they created.

I am also very grateful for the helpful and friendly staff at ASU Eyring Materials Center. Special thanks to Dr. Emmanuel Soignard, Diana Convey, Timothy Karcher, Dr. Thomas Groy and many others for their help, assistance and trainings. I am also thankful for the staff at School of Electrical, Computer and Energy Engineering for their help throughout my years at ASU.

Most important of all, I would like to thank my parents, Numan Balaban and Gonca Uygun, for their unconditional love and support in every step of my life. I would never have accomplished all of this without them. I would also like to extend my thanks to the rest of my family. Their encouragement and support played a tremendous role over the years. Finally, I'd like to thank my girlfriend, Shannon Winans, for her support, friendship and love. Thank you for making the last part of my Ph.D. years fun.

Mehmet Bugra Balaban

May 2020,

Tempe, Arizona, USA

TABLE OF CONTENTS

Page

LIST OF TABLES……………………………………………………………………….ix

LIST OF FIGURES………………….…….…..….………………………………...……x

CHAPTER

1 INTRODUCTION…………………………………………………………………...1

1.1 Redox Reactions and Mass Transport of Ions in Programmable

Metallization Cells…….………………………………………………….…1

1.2 Resistive Memory Technologies………………………………………….4

1.3 Requirements for the Universal Non-Volatile Memory (NVM) Cell……..9

1.4 Versatility of PMCs and Their Applications……….…………….……….10

1.5 Bilayer Switching in PMCs……………….….….………………………14

2 INTRODUCTION TO MATERIAL CHARACTERIZATION…………………16

2.1 X-Ray Diffraction (XRD)……………………………………………...…16

2.2 X-Ray Reflectivity (XRR)………………………………………………..17

2.3 X-Ray Photoelectron Spectroscopy (XPS)………………………………17

2.4 Auger Electron Spectroscopy (AES)……………………………………..18

2.5 Secondary Ion Mass Spectroscopy (SIMS)………………………………19

2.6 Electron Microscopy……………………………………………………...19

2.7 Ellipsometry………………………………………………………………21

2.8 Atomic Force Microscopy (AFM)………………………………………..21

3 EFFECT OF CATHODE MATERIAL AND ANNEALING CONDITIONS ON

FORMING VOLTAGE AND INITIAL RESISTANCE………………………...22

CHAPTER Page

3.1 Introduction to PMC Device Performance……………………………….22

3.2 Fabrication of Cu-SiO_x PMC Devices……………………………….....25

3.3 Electrical Characterization………………………………………………..28

3.4 Material Characterization (TEM & EDX)………………………………..32

3.5 Statistical Analysis of Forming Voltage………………………………….35

3.6 Discussion………………………………………………………………...40

4 COPPER OXIDATION…………………………………………………………….44

4.1 Brief Review of Copper Oxidation……………………………………….44

4.2 Oxidation Phases and Kinetics of E-beam Evaporated Copper at Low Temperatures……………………………………………………………..49

4.2.1 XRD………………………………………………………...…50

4.2.2 XPS…………………………………………………………….53

4.2.3 AFM………………………………………………………...…56

4.2.4 Spectroscopic Ellipsometry……………………………………...60

5 DIFFUSION OF COPPER………………………………………………………63

5.1 Brief History of Integration of Copper and Diffusion Kinetics…………63

5.2 Diffusion of Cu in WO_3……………………………………………………67

5.2.1 XPS……………………………………………………….…...…67

5.2.2 SIMS………………………………………………………………..73

5.2.3 TEM………..……………………………………………………..78

5.2.4 XRD………………………………………………………...…83

CHAPTER Page

6 MODELING THE OXIDATION & DIFFUSION OF Cu/WO_3……………….…85

6.1 Building the Model……………………………………………………85

6.2 Copper Oxidation Model………………………………………….…86

6.3 Simulations of the Oxidation & Diffusion Model of Cu/WO_3…………..87

7 LATERAL PMC DEVICES USING $Cu_2O/Cu\text{-}WO_3$ BILAYER……………….92

7.1 Fabrication of Lateral PMC Devices……………………………………92

7.2 Characteristics of the Bilayer Solid Electrolyte…………………………93

7.3 Results and Discussion………………………………………………..94

8 CONCLUSION…………………………………………………………106

REFERENCES……………………………………………………………………109

APPENDIX……………………………………………………………………..131

A IMAGEJ SCRIPT FOR PARTICLE SIZE ANALYSIS OF AFM IMAGES….131

B MATLAB CODE OF OXIDATION AND DIFFUSION MODEL FOR $Cu\text{-}WO_3$ SYSTEM……………………………………………………………….133

C MATLAB CODE OF LATERAL PMC DEVICE SIMULATION………..…137

LIST OF TABLES

Table Page

3.1. ANOVA (CE: W) 36

3.2. Effect Estimate Summary (CE: W) 37

3.3. Ranking of the Importance of the Factors (CE: W) 37

3.4. ANOVA (CE: Ni) 39

3.5. Effect Estimate Summary (CE: Ni) 39

3.6. Ranking of the Importance of the Factors (CE: Ni) 39

4.1. Standard Thermodynamic Properties of Cu_2O and CuO 44

4.2. Oxidation Kinetics Rate Law Formulas 46

4.3. Summary of the Activation Energy of Diffusion (E_a) Values 48

4.4. Summary of the Average Particle Sizes Calculated with ImageJ 58

5.1. Summary of the Reported E_a of Diffusion of Cu in SiO_2 and Silica by BTS 65

5.2. Diffusion Coefficients for Each XPS Sample (Cu-WO_3) 72

5.3. Fabrication/Annealing Conditions of the Blanket Films for TEM & XRD 78

6.1. Variables Used in the Model for Cu-WO_3 System 85

LIST OF FIGURES

Figure Page

1.1. The Schematic of Electrodeposition 2

1.2. Ionic Hopping Barriers in Ag-doped Amorphous Chalcogenide Showing the Wannier-Stark Ladder 3

1.3. Resistive Switching Effects and Random Access Memory Names 5

1.4. a) Unipolar Switching and (b) Bipolar Switching 7

1.5. Illustration of the Mechanism of Resistive Non-volatile Switching in an Ag-ChG PMC 8

1.6. Schematic of Set and Reset Operation of Cu-SiO_2 PMC 9

1.7. Vertical and Lateral PMC Structures 11

1.8. Lateral PMC Device Structure with 3 Electrodes 12

1.9. Radial PMC with Metallic Electrodeposits 13

3.1. Cu Doping Techniques in Cu-SiO_x PMCs 24

3.2. W (Ni) Deposited on Top of Si_3N_4/Si by Sputtering 25

3.3. Cathode Stripes Patterning by Photolithography 26

3.4. Wet Etching to Create the Cathodes 26

3.5. Switching Layer Deposition by E-beam Evaporation 26

3.6. Anode Creation After Wet Etching 27

3.7. Deposition of Capping Silica Layer by E-beam Evaporation 27

3.8. Idealized Cross-section of the Devices 28

3.9. Forming Voltage vs. Annealing Time for Devices Annealed at 450 °C 29

3.10. Forming Voltage vs. Annealing Time for Devices Annealed at 550 °C 29

Figure Page

3.11. Initial Resistance vs. Annealing Time for Devices Annealed at 450 °C 30

3.12. Initial Resistance vs. Annealing Time for Devices Annealed at 550 °C 30

3.13. Retention Test on W/SiO_x/Cu Device Annealed at 500 °C for 10 min 31

3.14. I-V Characteristics of the Forming Process in W/SiO_x/Cu PMCs 32

3.15. (a) TEM Cross-section Image of Ni/SiO_x/Cu/SiO_x Annealed at 550 °C for 10 Minutes, (b) EDX Line Scan Result of the Dashed Line 32

3.16. (a) TEM Cross-section Image of W/SiO_x/Cu/SiO_x Annealed at 550 °C for 10 Minutes, (b) EDX Line Scan Result of the Dashed Line 33

3.17. (a) TEM Cross-section Image of W/SiO_x/Cu Annealed at 550 °C for 10 Minutes, (b) EDX Line Scan Result within the Dashed Circle 34

3.18. (a) TEM Cross-section Image of W/SiO_x/Cu/SiO_x Annealed at 400 °C for 10 Minutes, (b) EDX Line Scan Result of the Dashed Line 34

3.19. (a) TEM Cross-section Image of W/SiO_x/Cu/SiO_x Annealed at 400 °C for 10 Minutes, (b) EDX Line Scan Over the Switching Layer 35

3.20. TEM Cross-section Image of the Devices Annealed for 10 Minutes 35

3.21. Cube Plot, CE: W (2^2 Design Replicated 4 Times) 36

3.22. Normal Probability Plot for V_F (CE: W) 38

3.23. Cube Plot, CE: Ni (2^2 Design Replicated 4 Times) 38

3.24. Normal Probability Plot for V_F (CE: Ni) 40

4.1. Cu-O Phase Formation for Samples Annealed in Air 45

4.2. Control Sample for Oxidation Experiments 49

4.3. Copper Oxidation Samples After Annealing 50

Figure Page

4.4. XRD Patterns of Cu Control Sample and Increasing Temperatures 51

4.5. XRD Patterns of Cu Annealed at 125 °C 52

4.6. XRD Patterns of Cu Annealed at 155 °C 52

4.7. Control Sample (Left) and the Samples After Annealing (Right) for XPS 53

4.8. Cu 2p XPS Spectra of the Sample Shown in Figure 3.7 Annealed at 125 °C . 54

4.9. Cu 2p XPS Spectra of the Sample Shown in Figure 3.7 Annealed at 140 °C . 55

4.10. Cu 2p XPS Spectra of the Sample Shown in Figure 3.7 Annealed at 155 °C . 55

4.11. AFM Images of the Oxidation Samples 56

4.12. AFM Images of the Oxidation Samples at 155 °C 57

4.13. Image of the Cu_2O Sample Pre- and Post-Processing 58

4.14. Particle Size Histograms of Samples Annealed for 70 Minutes 59

4.15. Particle Size Histograms of Samples Annealed at 155 °C 59

4.16. Cu_2O Thickness (d_{ox}) vs. Annealing Time 60

4.17. d^2_{ox} vs. Annealing Time 61

4.18. Arrhenius Plot of ln (k_p) vs 1/T 62

5.1. Samples Before Annealing (Left) and After Annealing (Right) for XPS 68

5.2. Depth Profile of Cu (at%) 69

5.3. Depth Profile of Cu (at%) of XPS Sample #1 70

5.4. Depth Profile of Cu (at%) of XPS Sample #2 70

5.5. Depth Profile of Cu (at%) of XPS Sample #3 71

5.6. Plot of ln (C) vs x^2 for the Diffusion Data for XPS Sample #1 72

5.7. Plot of ln (D) vs 1/T 73

Figure Page

5.8. Si_3N_4/Si Sample on the Left and WO_3/Si_3N_4/Si Sample on the Right 74

5.9. Blanket Films of Cu/WO_3/Si_3N_4/Si 74

5.10. SIMS Profile of Si_3N_4/Si Sample 75

5.11. SIMS Profile of WO_3/Si_3N_4/Si Sample 75

5.12. SIMS Profile of Unannealed Cu/WO_3/Si_3N_4/Si Sample 76

5.13. SIMS Profile of Annealed Cu/WO_3/Si_3N_4/Si Sample 76

5.14. Structure of the As-deposited Blanket Films for TEM Analysis 78

5.15. Cross-section TEM Image of the Sample 1, Cu_2O/Cu-WO_3/Si_3N_4/Si 79

5.16. TEM Image (Left) and the EELS (Cu Mapping) of the Box (Right) 79

5.17. HR-TEM Image of the Cross-section of Sample 1 81

5.18. TEM Analysis of the Sample 1 81

5.19. *d*-spacing Calculation of the Cluster in Figure 5.18b, $d\sim$ 2.134 Å 82

5.20. *d*-spacing Calculation of the Cluster in Figure 5.18c, $d\sim$ 2.187 Å 82

5.21. XRD Patterns of TEM Samples Shown in Table 5.3 84

6.1. Cu Concentration vs. Depth for Case 1 87

6.2. Cu Concentration vs. Depth for Case 2 88

6.3. Cu Concentration vs. Depth for Case 3 89

6.4. Cu Concentration vs. Depth for Case 4 90

6.5. Cu Concentration vs. Depth for Case 5 91

7.1. Idealized Cross-section of the Devices After Annealing 93

7.2. Current-time Plots of Device 1 and Device 3 95

7.3. Optical Micrographs of (a) Device 1 and (b) Device 3 Post-Biasing 96

Figure Page

7.4. (a) Optical Micrograph of the Device Post-Bridging, (b) SEM Image of the Same Device…………………………………………………….. 98

7.5. TEM Analysis of the Electrodeposit.. 99

7.6. Bilayer Resistance Model 100

7.7. Simplified Bilayer Resistance Model 100

7.8. Simulation Result Showing Filament Length vs Time 102

7.9. Simulated Cation Concentration vs Filament Length 103

7.10. Current Density vs Filament Length.. 104

7.11. Simulated Current Through the Entire Resistance Model 105

CHAPTER 1

INTRODUCTION

1.1 Redox Reactions and Mass Transport of Ions in Programmable Metallization Cells

Redox reactions mean that there are reactions involving both reduction and oxidation of ions/atoms. Oxidation of atoms means gain of oxygen or loss of electrons which are described by equation (1.1) and equation (1.2) respectively. Reduction of ions means loss of oxygen or gain of electrons which are described by equation (1.3) and equation (1.4) respectively [1].

$$aM + bO_2 \rightarrow M_aO_{2b} \quad (1.1)$$

$$M \rightarrow M^{n+} + ne^- \quad (1.2)$$

$$M_aO_{2b} \rightarrow aM + bO_2 \quad (1.3)$$

$$M^{n+} + ne^- \rightarrow M \quad (1.4)$$

where M denotes an element (usually a metal), e^- is electron, and a, b, n denote an integer.

Redox reactions are the core of electrodeposition which is defined as an electrolytic process where a metal is deposited at the cathode from a solution of its ions. This process, shown in Figure 1.1, is also commonly seen in solid state devices such as Programmable Metallization Cell (PMC) devices. Electrodeposition starts with positively biasing the anode material which is oxidizable. Atoms lose electron(s) and ionize which then drift towards the cathode under electric field within the solid solution (solid electrolyte film in PMCs). Then, when they reach the cathode, they get deposited by reduction to atoms which become immobile. If the cathode is chemically inert (the case of PMCs), the process is also reversible. In order to reverse the process, the anode is then negatively biased, and the

deposited atoms will get oxidized and transport back to the anode. When they reach the anode, they will be reduced and deposited on to the anode. Equation (1.2) is known as the anodic dissolution and equation (1.4) is known as the electrocrystallization in PMCs.

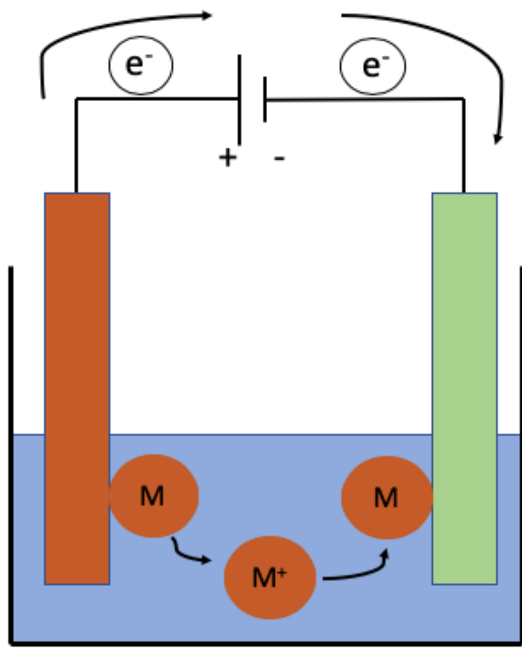

Figure 1.1: The schematic of electrodeposition.

Redox reactions in PMCs occur at the electrode/solid electrolyte interface. The current density for charge transfer at the interface can be described as Butler-Volmer equation [2]:

$$J = J_0[\exp\left(\frac{\alpha z q \eta}{kT}\right) - \exp\left(-\frac{(1-\alpha) z q \eta}{kT}\right)] \tag{1.5}$$

where J_0 is the exchange current density, α is the cathodic charge transfer coefficient, η is the electrochemical overpotential, z is the number of electrons, q is the electron charge, k is the Boltzmann constant and T is the temperature in Kelvin. For high cathodic potential $\eta \gg kT/ne$, the equation becomes

$$\ln (J) = \frac{\alpha z q}{kT}\eta + \ln\ (J_0) \tag{1.6}$$

When compared to the volume/size of the electrolyte, the electrode/electrolyte interface is quite small. Due to this enormous difference, the switching kinetics in a PMC may be governed by the mass transport of the ions, especially when the ion migration is quite slow. It is recognized that ion conduction in solid electrolytes is accomplished by ionic hopping. Ion transport within the solid electrolyte (SE) in PMCs can be explained by the electric field driven thermally activated Mott-Gurney model [3], [4]. For example, in the case of PMCs utilizing Ag-doped SE (can also be Cu-doped), Ag^+ ions reside in potential wells in the electrolyte and can hop through these small barriers, changing its location. All of these barriers under no-bias have the same potential energy, therefore the ions can jump towards any of the surrounding wells. However, when there is applied voltage (i.e. existing electric field), the barrier heights become lower along a certain direction, hence dramatically increasing the chances of the ions moving in the direction of the electric field. This barrier lowering effect is called the Wannier-Stark ladder [5]. This process is shown in Figure 1.2.

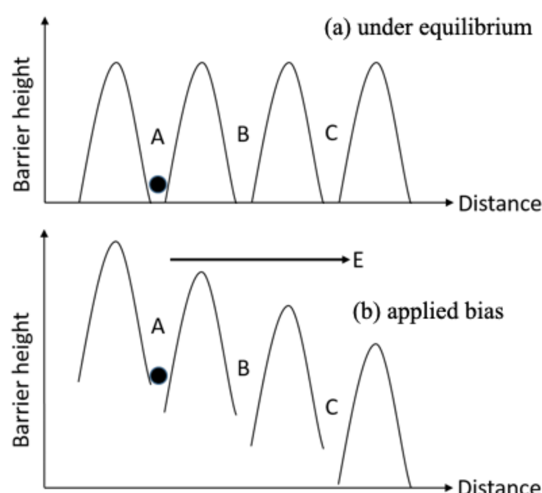

Figure 1.2: Ionic hopping barriers in Ag-doped amorphous chalcogenide showing the Wannier-Stark ladder.

The ionic hopping is significantly affected by the electric field, E, and the electric field is defined as the potential drop in the solid electrolyte (SE), $\Delta\varphi_{SE}$, across the film thickness, d.

$$E = \Delta\varphi_{SE} / d \tag{1.7}$$

The current density for hopping, then, can be defined as,

$$J_{hop} = 2zqN_i av \exp\left(-\frac{E_0}{kT}\right) \sinh\left(\frac{azqE}{2kT}\right) \tag{1.8}$$

where J_{hop} is the ion current density, z is the number of charge, q is the charge of an electron, N_i is the concentration of cations, a is the is the mean hopping distance of the ions, v is the hopping frequency, E_0 is the height of the energy barrier, k is the Boltzmann constant, T is the temperature in Kelvin, E is the electric field. For high electric fields ($E >> 2kT/azq$), sinh behavior becomes an exponential and the equation can be written as,

$$J_{hop} = 2zqN_i av \exp\left(-\frac{E_0}{kT}\right) \exp\left(\frac{azqE}{2kT}\right) \tag{1.9}$$

whereas for low electric fields ($E << 2kT/azq$), the dependence of J_{hop} on E becomes linear and the equation can be written as,

$$J_{hop} = \frac{(zq)^2 N_i E}{kT} a^2 v \exp\left(-\frac{E_0}{kT}\right) \tag{1.10}$$

where $a^2 v \exp\left(-\frac{E_0}{kT}\right)$ represents the diffusion coefficient.

1.2 Resistive Memory Technologies

There has been a search for new materials to be used in memory devices with the ongoing scaling of semiconductor devices which was first introduced by Gordon Moore in 1965 [6]. Constantly evolving devices such as memory devices promise higher density,

faster response, and lower power consumption [7]. Higher density enables more data storage for the same area, faster response means more computation for the same amount of time, and lower power consumption means longer battery life. After the long use of magnetic hard disk drives (HDD) and NAND Flash in the electronics industry [8], resistive memory technologies are promising to replace existing technologies in the future [9]. Devices such as phase-change random access memory (PCRAM) [10]–[13], spin-torque transfer random access memory (STTRAM) [14]–[16], and other resistive memory technologies [17]–[19] offer the industry novel non-volatile technologies. While all these technologies are based on the changes in resistance value of the cell, the physical mechanism of the resistance change is different.

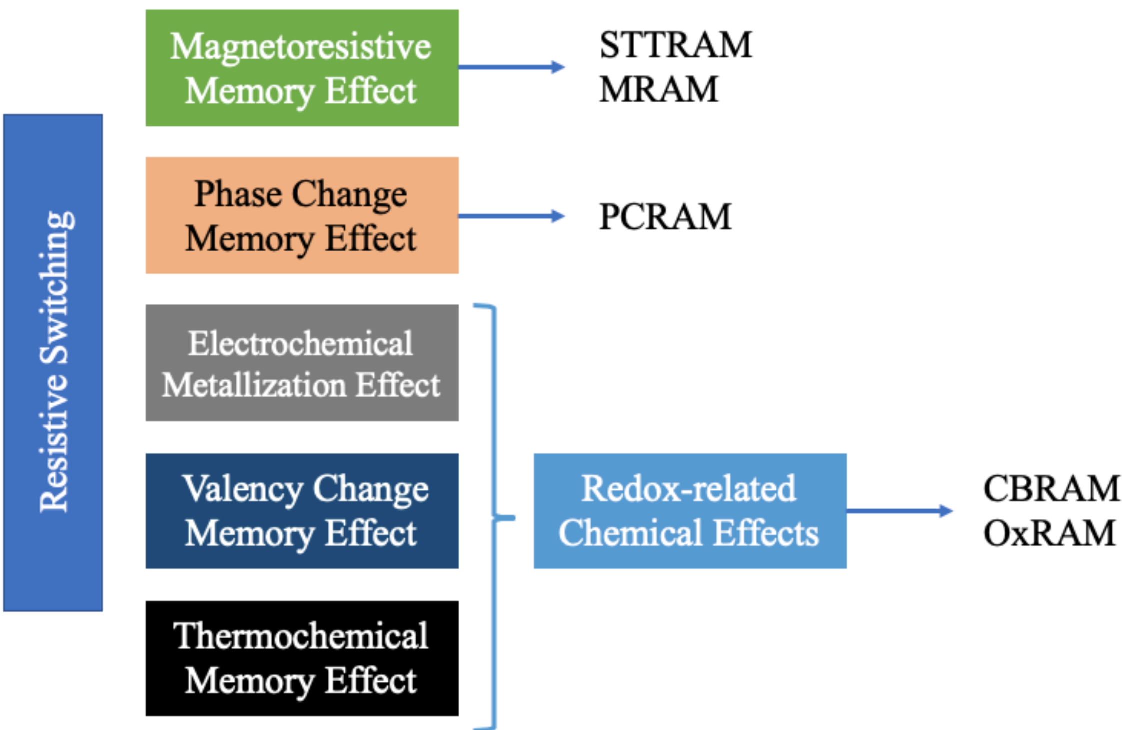

Figure 1.3: Resistive switching effects and random access memory names.

The resistance change in a PCRAM occurs with thermal activation of the cell, where the phase of the material changes between amorphous and crystalline state [11]. While the resistance of the amorphous cell is high (programmed to be ‘0’), the resistance of the crystalline state is low (programmed to be ‘1’). In a STTRAM cell, the resistance change is based on switching the spin-torque transfer in the magnetic tunnel junction (MTJ) [20] and the cell stores the information according to the spin of the electron [21]. While the spin on the fixed layer remains unchanged, with the applied bias, spin on the free layer can be altered. When the spins of two layers are in the opposite direction, the resistance of the cell is high (programmed to be ‘0’). On the other hand, when the spins are in the same direction, the resistance of the cell is low (programmed to be ‘1’). The resistance change in a redox-related memory (Re-RAM) cell occurs with the formation and dissolution of a conductive filament when there is an applied bias [22]. So far for Re-RAM, three variants have been developed which are unipolar switching, anion-based bipolar switching and cation-based bipolar switching.

Unipolar switching occurs when the write and erase of the cell is done by the same polarity of applied voltage. For example, the resistance of the cell can be switched from high to low by a positive voltage, and this process can be reversed by a smaller positive voltage. Unipolar switching is reported in NiO_x-based devices [23]–[25], TiO_x-based devices [26]–[28], HfO_x-based devices [29], [30], TaO_x-based devices [31] and using La-$SrTiO_3$ perovskite thin films [32]. Other than NiO_x-based devices, unipolar behavior in devices is achieved by using high compliance currents.

Bipolar, unlike unipolar, switching occurs when the resistance state of the cell can switch back and forth high to low with opposite polarity of the applied voltage. In anion-

based bipolar switching devices, the resistance change occurs because of the drift of the oxygen anions (O^{2-}), hence they are based on valency change memory effect. These devices have been reported to utilize Al_2O_3 [33], TiO_x [34]–[37], HfO_x [38]–[42], MoO_x [43], TaO_x [44]–[46] and $SrTiO_3$ [47]–[49] for the switching layer. The electrodes of such devices are made of inert materials.

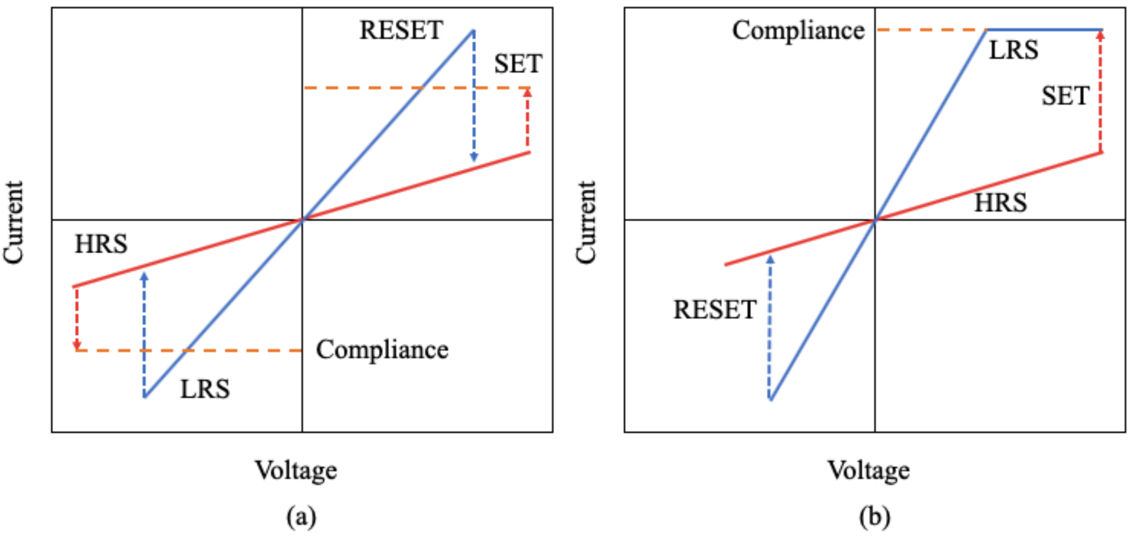

Figure 1.4: a) Unipolar switching and (b) bipolar switching.

In cation-based bipolar switching devices, the resistance change is due to the growth and dissolution of a metallic filament. These devices are also called PMCs, electrochemical metallization (ECM) cells, or conductive bridging random access memory (CBRAM) for memory applications. During this process chemical redox reaction and metal ion transport occur and the drifting ions are typically Ag or Cu ions [50]. These ions come from the electrode material which is chemically oxidizable (anode), whereas the cathode is an inert material such as Pt, W or TiN. Some of the reported switching layers for PMCs are chalcogenide glasses (ChG) such as Ge_xSe_{1-x} [51]–[59] or Ge_xS_{1-x} [60]–[66], oxide

electrolytes such as SiO_x [67]–[73], WO_3 [74]–[78], Al_2O_3 [79]–[82] or GdO_x [83], Ta_2O_5 [84]–[87] and a-Si [88], [89].

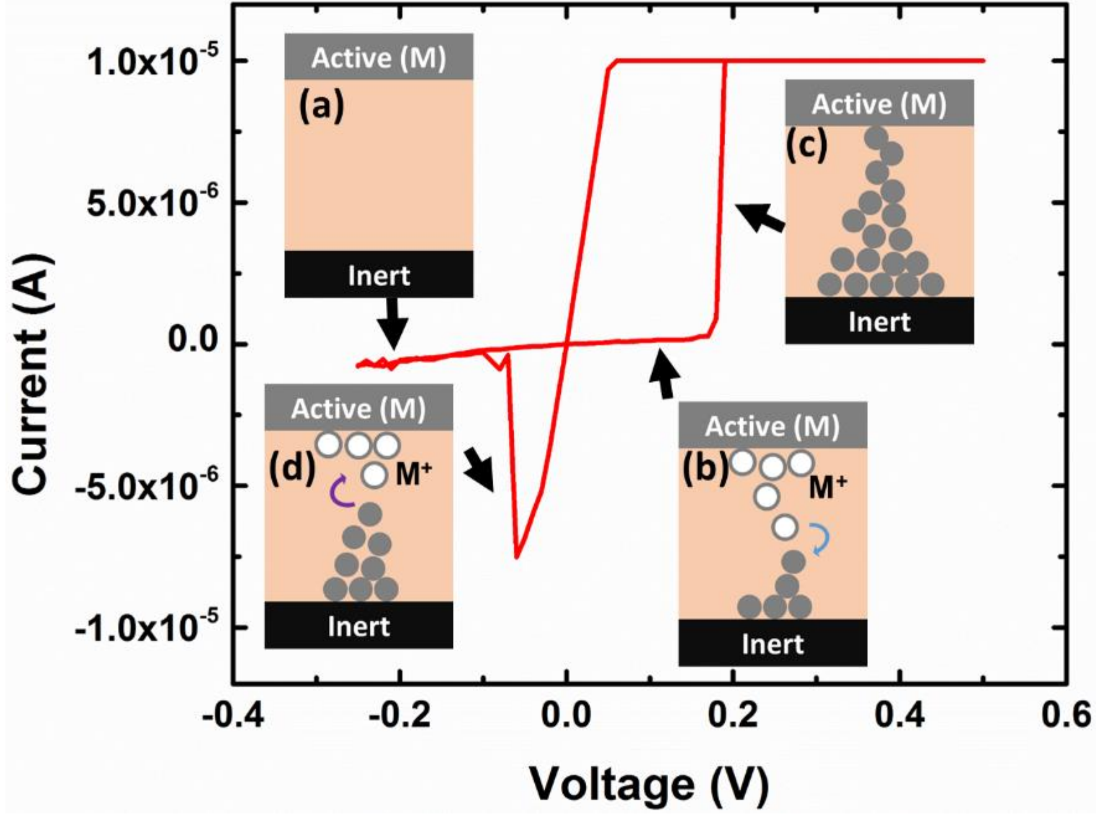

Figure 1.5: Illustration of the mechanism of resistive non-volatile switching in an Ag-ChG PMC. © 2016 IEEE. Reprinted with permission [59].

The filament growth in ChG-based PMCs, shown in Figure 1.5, is well studied and it is shown that filament growth occurs from the cathode towards the anode [50], [90] and this is due to the high ion mobility in chalcogenide glasses. However, many oxides possess low ion mobility compared to chalcogenide glasses and some reported that filament growth in oxides is in the opposite direction, from the anode to the cathode [89], [91], [92]. This behavior is believed to change the filament growth direction and proposed example of switching is shown in Figure 1.6.

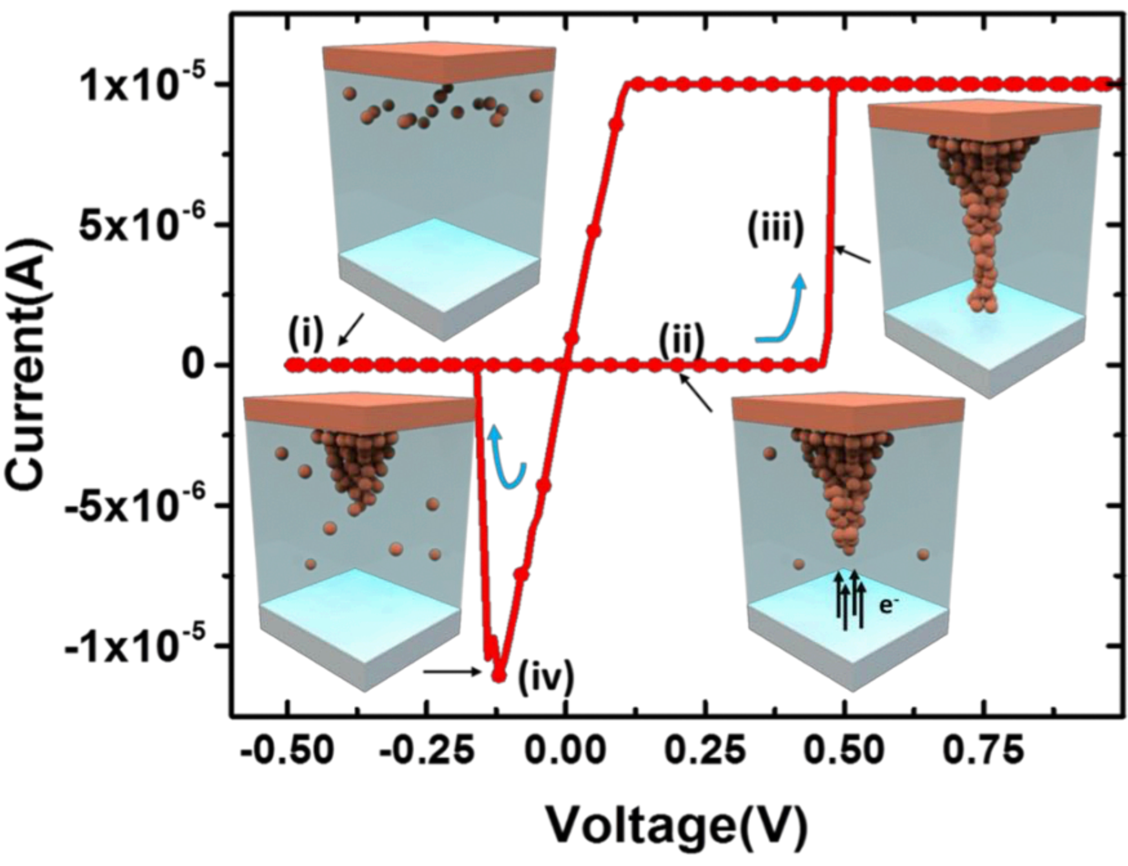

Figure 1.6: Schematic of set and reset operation of Cu-SiO_2 PMC. © 2015 IEEE. Reprinted with permission [93].

1.3 Requirements for the Universal Non-Volatile Memory (NVM) Cell

The universal NVM cell should compare or improve the existing technologies. Flash at its current state suffers from high programming voltages (V_{wr}) and high programming times (t_{wr}). In order to improve upon that, programming voltages should be less than few volts to be better than Flash and ideally be around few mV to be compatible with CMOS. Programming speed of the ultimate NVM should be much better than Flash (~10 μs), compete with DRAM specifications (<100 ns) and come close to the speed of SRAM (<10 ns). Read voltages, while being significantly lower than the write voltages, cannot be less than about one-tenth of the V_{wr} due to circuit design constraints. The read

time (t_{rd}) must ideally be shorter than t_{wr}. Because the resistance state of the cell must be read quickly by small sense amplifiers, the read current cannot be less than 1 μA. Due to the use of these small sense amplifiers, a minimum ratio of 10 should be achieved between the on and off resistance values (R_{OFF}/R_{ON}). The universal NVM cell should also at least compete or be better than Flash which has write cycles (endurance) between 10^3 and 10^7. And lastly, the data retention of the cell must be minimum 10 years and it should withstand thermal stress up to 85 °C while being stressed by small electrical pulses [94]. CBRAM, at its current state, shows extremely promising results regarding the requirements mentioned above [50], [52].

1.4 Versatility of PMCs and Their Applications

Versatility of PMCs is one of their great properties. They can be made in vertical, lateral and radial structures. The vertical structures are generally used as a memory cell as described above. The lateral structures can be used in radio frequency (RF) switches [95], optical switches [96], [97], microfluidic valves [98], tunable resonators [99], tuning elements in MEMS devices [100] and timing devices [101], [102]. Radial structures can be utilized as physical unclonable functions (PUFs) [103] due to its easy-to-evaluate but hard-to-predict nature.

The solid electrolyte layer is sandwiched between two metal electrodes in a vertical structure. PMC, initially, has a high-resistance state (HRS). However, when there is an applied positive voltage between the anode and the cathode, a conductive filament (CF) can be formed between the electrodes as shown in Figure 1.5 and 1.6. After the formation

of the CF, the resistance of the cell drops significantly which depicts the low-resistance state (LRS). Switching to LRS is known as the set (also known as “write” or “program”) process. The switching back to HRS is known as the reset (also known as “erase”) process where the biasing is reversed between the anode and the cathode. Vertical and lateral PMC structures are shown in Figure 1.7.

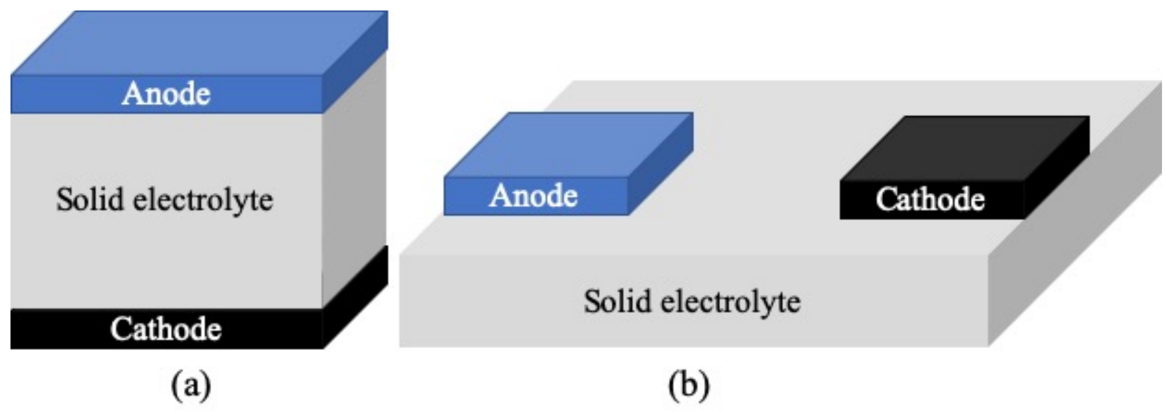

Figure 1.7: (a) Vertical and (b) lateral PMC structures.

Using PMCs as timing devices is in the early stages of its development. It uses the PMC properties of non-volatility and filament growth. When the power is on for a circuit, the timing device will also be powered. Then, the conductive filament between the two electrodes will start to form. As the power is turned off, the filament will stop growing and retain its latest state. This is superior to the conventional solid-state relays as they do not retain their state when the power is off. The proposed structure is shown in Figure 1.8 and it is a lateral structure with a minor adjustment, the sensing electrode. The third electrode is designed and placed on to the lateral structure so that when needed it can measure the impedance of the device. The change in the filament will cause a change in the impedance

reading. Because the filament will change its length only when the power is on, the impedance-lifespan can be calibrated, and the device can be used as a timer.

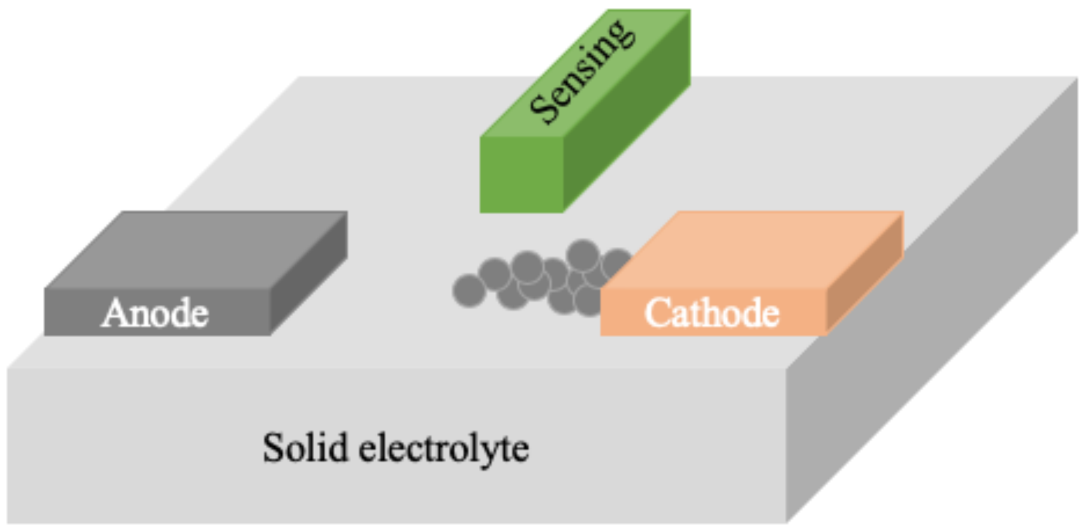

Figure 1.8: Lateral PMC device structure with 3 electrodes.

Ag-ChG memory devices offer great advantages thanks to its retention capabilities, low power consumption, fast switching, low cost and scalability. They have already been commercialized which shows that they can meet the industry requirements [62]. When memory applications are concerned, Ag-ChG devices show great properties. However, one of the main disadvantages of such devices is the difficulty to integrate them into integrated circuits (ICs). Ag and GeSe/S are not foundry compatible materials which means that they are not currently being used in IC fabrication. Low power consumption, low cost and non-volatility of PMCs enable them to be great candidates for RF switches [95]. But current PMCs do need some improvements. Requirement of very low resistance in LRS (because of the low insertion loss requirement) means that the CF must be thick enough. Thicker filaments, on the other hand, requires higher energy to be erased. The necessity of higher

energy can create problems with Joule heating effect which can result in some remaining metals, which then will create problems with cycling. PUF applications of PMCs are also in the early stages of development. They offer low power consumption, strong attack resistance and robustness which make them strong candidates to be used in security electronics. For PUF applications, the radial devices seem to be the best structure because multiple devices can be formed at the same time while the dendrites will all be unique showing different optical properties. Radial structure is shown in Figure 1.9.

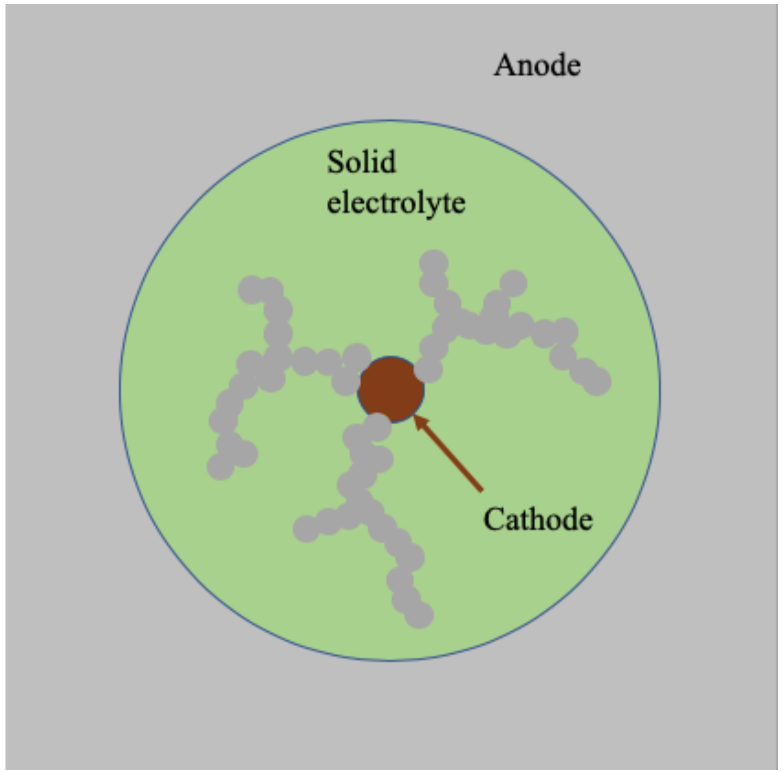

Figure 1.9: Radial PMC with metallic electrodeposits.

Copper-doped SiO_x ($Cu\text{-}SiO_x$) PMC devices also exhibit great capabilities and applications such as non-volatile memory cell, selector behavior, multilevel cell (MLC) capabilities and electronic synapse for neuromorphic computation [59], [73], [76]. Moreover, these materials are already being used in the back-end-of-line (BEOL)

processing which means that they are foundry compatible, so that the inclusion of such applications will be cost effective. More detail on the Cu-SiO_x system is presented in Chapter 3.

1.5 Bilayer Switching in PMCs

In addition to single switching layers mentioned in 1.3, there are memory cells that utilize bilayers as the switching layer. Some of the bilayer combinations presented in the literature are Cu_xO/SiO_2 [104], $TiO_x/TaSiO_y$ [105], $CuInO_2/CuO$ [106], $GeSe_x/TaO_x$ [107], [108], Cu_xO/Cu_xS and SiO_2/Cu_xS [109], $GeSe_x/SiO_x$ [110], CuGeTe/Al_2O_3 [111], Cu-MoO_x/GdO_x [112]. Classification of the resistive switching effect in the bilayer devices mentioned above is the electrochemical metallization effect which means that the resistive switching is due to the growth and dissolution of a metallic filament. Because these bilayers either have copper compounds with metal electrodes deposited on top; or they do not have copper compounds, but they have copper as the active electrode, the metallic filament is copper. The compounds such as Cu_xO, CuGeTe are believed to be the ion supply layer in the devices without a Cu electrode. In devices that have Cu_xO as one of the bilayers and Cu as a top electrode, Cu_xO is believed to assist the ionization process. In other bilayer devices without copper compounds such as $TiO_x/TaSiO_y$, $GeSe_x/TaO_x$ and $GeSe_x/SiO_x$, one layer is used as a buffer layer. This improves switching performance due to filament length confinement. Furthermore, these buffer layers help regulate the overgrowth of the filament.

As mentioned previously in 1.4, PMCs are versatile devices that can be in different configurations and can be used in different applications. Lateral PMCs can also utilize

bilayers such as Cu_2O/Cu-WO_3 or Cu_2O/Cu-SiO_x which show great promise to be used for various applications. Annealing the deposited stack of Cu/WO_3 or Cu/SiO_x in air at low temperatures without a capping layer results in Cu_2O/Cu-WO_3 and Cu_2O/Cu-SiO_x respectively. This is due to Cu being oxidized from the top and its diffusion at the Cu/WO_3 or Cu/SiO_x interface. This offers a few advantages for the PMC. First of all, oxidizing from the top ensures that there will be no metallic Cu left on the surface that would cause the devices to short. Moreover, the as-deposited structure (pre-annealing) can have thicker deposited Cu layer that enables better roughness-to-deposition thickness ratio and uniform doping in the WO_3 or SiO_x layer during annealing. The resulting Cu_2O thickness and the Cu concentration in the WO_3 or SiO_x layer can be controlled by the annealing conditions and the deposited thickness of Cu which both play a role in switching.

The following chapters of this dissertation consist of some introductory information about the material characterization tools used in this dissertation, analysis of the effect of the counter (bottom) electrode material and the annealing conditions on the Cu-SiO_x vertical devices, oxidation of copper at low temperatures including oxidation kinetics, diffusion of copper in WO_3, oxidation and diffusion model built in Matlab to assist fabrication of lateral PMC devices using Cu-WO_3 system, and preliminary results of lateral PMC devices utilizing the bilayer Cu_2O/Cu-WO_3 as the switching medium.

CHAPTER 2

INTRODUCTION TO MATERIAL CHARACTERIZATION

2.1 X-Ray Diffraction (XRD)

XRD is widely used to determine the crystal structure of samples where the result of the analysis does not depend on the composition of the sample which was first discovered in 1912 by Max von Laue [113]. The beam is a relatively large (50 – 500 μm) Cu Kα x-ray with the λ=0.15418 nm (8.04 keV). The incident beam goes under coherent scattering, which means that the angle and the energy of the beam do not change during the interaction. During the interaction, matrix electrons, also known as scatterers, produce an array of spherical waves. These waves cancel out one another in most directions except for the ones that add constructively under Bragg's Law:

$$n\lambda = 2d\sin\theta \tag{2.1}$$

where n is an integer, λ is the wavelength of the beam, d is the spacing between the planes in atomic lattice, and θ is the angle between the incident beam and the scattering plane [114]. After diffraction, x-rays are collected, and the structure/phase information can be obtained from the intensity-2θ plots [115].

There are two widely used XRD configurations. The first one, θ:θ, utilizes a fixed sample and the beam rotates with θ°/min while the detector rotates at θ °/min. The other one, θ:2θ, uses a fixed beam and the sample rotates with θ °/min while the detector rotates at 2θ °/min. Less commonly used detector scan enables the researchers to focus the beam near the surface where thin film characterization is of interest.

2.2 X-Ray Reflectivity (XRR)

XRR is one of the most useful material characterization tools for metrology. It is used to determine the density, the thickness and the roughness of multilayer thin films. Incident beam, usually Cu Kα, has a very low incident angle (ω) up to 3 degrees and is reflected from the sample. The reflected intensity will deviate from that of the incident beam according to the Fresnel reflectivity [116] and is analyzed to determine the layer properties.

Proper fitting of data is difficult when the average roughness of layers exceeds 3 nm. In order to determine thickness, the reflectivity fringes must be observed. Very rough surfaces may make these fringes disappear; hence the thickness determination may become challenging. XRR is very sensitive to surface layers due to low penetration of the incident beam and the low incidence angle [117].

2.3 X-Ray Photoelectron Spectroscopy (XPS)

XPS is a surface characterization tool that is based on Einstein's photoelectric effect [118]. The incident beam is made of photons (x-rays specifically) usually Al Kα (1486.6 eV) or Mg Kα (1253.6 eV). When the incident beam hits the sample, core electrons are excited to high energy states above the vacuum level. The core hole, with the core binding energy E_b, later decays either through a photon emission or an Auger process. The detector then collects the emitted core electrons and measure their kinetic energy (E_k).

$$E_k = h\upsilon - E_b - \phi \tag{2.2}$$

where $h\upsilon$ is the incident beam energy and ϕ is the work-function of the spectrometer. After measuring the kinetic energy, given the fact that the incident beam energy is known, the software calculates the binding energy. This allows the researchers to determine what type of bond exists on the surface, often providing insight about the oxidation state. The collected electrons have low energies, typically lower than 1.5 keV. Because the electrons have low energies, ultra-high vacuum (UHV) inside the chamber must be achieved. Even though synchrotron sources enable scientists to use continuous photon energies for the incident beam, they are not widely available.

2.4 Auger Electron Spectroscopy (AES)

In AES, the incident beam is composed of electrons with energies typically less than 20 keV. After the incident electron knocks off the core level electron, internal transition occurs, and sometimes instead of an x-ray coming off the sample, the sample ejects an Auger electron [119]. Then, these electrons can be detected to obtain elemental information.

Auger electrons have energies less than 2 keV, usually around 500 eV, with a typical escape depth of few nanometers from the surface, thus providing to be an excellent surface characterization tool. Due to the low energies of the Auger electrons, the chamber must be kept in UHV. Because there has to be at least three electrons in order for auger process to occur, the lightest detectable element is Li. Furthermore, due to the use of an electron incident beam, the lateral resolution of AES tools can be as good as few nanometers.

2.5 Secondary Ion Mass Spectroscopy (SIMS)

SIMS is one of the most surface sensitive tools to analyze composition of thin films. A high energy primary ion beam is focused on the sample and sputters the sample layer by layer. Ejected secondary ions (coming from the sample matrix) are then collected by a mass spectrometer and their mass/charge ratios are analyzed. Primary ion beam is usually Ar^+ ions with an energy of several keV, while some other SIMS instruments utilize Xe^+, O_2^-, O_2^+, and C_{60}^+. Particularly C_{60}^+ is gaining more and more popularity because its depth resolution of sputtering is much better than other beams due to the low damage and the partitioning of the energy [120].

2.6 Electron Microscopy

The two most popular electron microscopy tools are scanning electron microscopy (SEM) and transmission electron microscopy (TEM). In SEM, there is a variety of modes that is available to choose from such as secondary electron imaging (SEI), backscattering electron imaging (BEI), energy dispersive spectroscopy (EDS), wavelength dispersive spectroscopy (WDS), and etc. The incident beam is composed of electrons which has energies up to 30 keV, and since the beam utilizes electrons it has a beam spot in the range of nanometers. The information in SEI is gathered from the secondary electrons coming from the matrix which have very low energies ranging from 1 to 50 eV. SEI mode has a depth resolution of about 1 nm and lateral resolution of 0.5 nm – 5 nm which is great for surface topography of any solid sample. BEI mode is excellent to use for surface imaging especially when there is a Z-contrast on the surface. Heavier elements will appear brighter as they make more electrons scatter back compared to lighter elements. The information in

EDS and WDS is obtained from the x-rays coming out of the matrix with energies of 1-20 keV. The difference between the two modes is on their output plot. EDS gives the information related to the energy of the x-rays, while WDS presents the wavelength of the collected x-rays. Because the information is obtained from x-rays, EDS and WDS modes have an escape depth (depth resolution) larger than SEI mode has. The performance of an SEM tool, which is the combination of the lateral resolution and signal-to-noise ratio, is determined by the probe current and its diameter [121].

TEM also utilizes electrons as primary beam, and the data is collected from the electrons that pass through the sample. Since the primary beam energy is known and the energy of the electrons at the other end can be measured, we can determine the material on the sample. The beam energy of the electrons is much higher compared to SEM, typically in the hundreds of keV. By using TEM in various modes such as contrast imaging, or diffraction; thickness of the material, phase of the material, types and position of defects, etc. can be determined [122].

When the sample is thin enough, while being very challenging to prepare it, obtaining electron diffraction (ED) patterns becomes possible. These patterns can be obtained from volumes as small as 1 nm^3 after short exposure times (a few seconds). Crystal defects, lattice parameter measurements, local strain and crystal orientations can be obtained using convergent-beam ED and large-angle convergent-beam ED [123].

2.7 Ellipsometry

Ellipsometry is a contactless, non-destructive technique that measures the changes in polarization of the reflected light with respect to the incident light [124]. It is mainly used to determine the thickness of dielectric films, line width and optical constants of films [125] while advanced ellipsometry techniques such as spectroscopic ellipsometry (SE) is also reported to be used for measuring the temperature during semiconductor processing [126]. SE measurements advanced the range of ellipsometry by using more than one wavelength [127]. SE also allows the users to change the angle of incidence which offers another degree of freedom for optimization of a material parameter of interest [128].

2.8 Atomic Force Microscopy (AFM)

AFM, first proposed in [129] by G.K. Binnig in 1986, utilizes a very sharp probe which scans the area of interest on a surface that produces a very high resolution image of the sample. The height resolution can be as low as sub-nanometer depending on the sharpness of the probe tip and the technique. The probe sits near the end of a cantilever arm which scans the area of interest and the topographic features are obtained as the probe interacts with the surface features. During the scan, a light source (laser) is focused on the probe which is then deflected on to a photodetector. Common modes of AFM are contact mode and tapping mode. While contact mode is considered to be 'static' as it is constantly in contact with the surface, the tapping modes, 'dynamic,' retracts and engages with the surface as the cantilever is oscillated close to its resonant frequency. Contact mode creates more lateral forces on the probe which can damage the tip. Therefore, it is better to use the AFM in tapping mode when the sample has steep edges [130].

CHAPTER 3

EFFECT OF CATHODE MATERIAL AND ANNEALING CONDITIONS ON FORMING VOLTAGE AND INITIAL RESISTANCE

3.1 Introduction to PMC Device Performance

Vertical PMC devices, also known as electrochemical metallization (ECM) cells utilize, for the most part, Cu or Ag as the active electrode (AE), or top electrode (TE), due to their high ion mobility in solid electrolytes (SE). One of the main applications of vertical PMCs is their memory application (CBRAM). As an emerging memory technology, it only makes sense for these devices to be made of materials that are foundry compatible. Silicon oxide (SiO_x, $x \leq 2$) has been used in the CMOS fabrication for many decades, however thermally grown SiO_2 is not the "perfect" SE layer for PMC devices [131], [132] as the oxide is very dense and requires high energy to switch. Foundry-compatible PMCs require a porous switching layer for Cu to drift and diffuse more easily as the filament formation and dissolution speed and energy consumption are crucial parameters. Back-end-of-line (BEOL) compatible silicon-rich oxide, SiO_x where $x < 2$ (SRO, silica), appears to be much more suitable for this application. Comparing Ag and Cu in silica, Ag makes weaker bonds to the silica matrix compared to Cu, therefore Cu has lower mobility [133]. In this sense, Ag is a better AE for fast switching. But, Cu is already being used in the BEOL process as the metal interconnect material [134] making it cost effective. Cu-silica PMCs also exhibit good enough switching speed [50]. Electrochemically inert metals are best suited for use as counter electrode (CE), or bottom electrode (BE), as they do not go under redox reactions. However, recent studies have shown that platinum group metals (PGM) such as

Pt and Pd migrate in SiO_x under electric field [135], [136]. Therefore, research on suitable materials for CE need to be conducted more in depth.

As previously explained in Chapter 1, PMCs operate under redox reactions at the electrode/SE interface and ion transport of the AE ions through the SE. The slowest of the three (because there are two electrode/SE interfaces) will limit the overall rate. Moreover, the water molecules (moisture), OH^- (hydroxyl ions) and H^+ (protons) can dramatically impact the electroforming at the interfaces [70]. Effect of moisture is also different for different electrodes as they have different electrocatalytic activities towards moisture [137]. In addition to the effects of moisture on the CE, electroforming can also be influenced by roughness of the electrode [138] and nucleation process [139].

Density of the silica layer, another important parameter, can be adjusted by tweaking fabrication parameters. One of the easiest ways to obtain different densities is depositing the silica layer by using different deposition techniques, e.g. e-beam evaporation, sputtering or various chemical vapor deposition (CVD) techniques. In order to first determine which deposition technique to use as less dense silica is desired, two different tools were used: e-beam evaporation and remote plasma CVD (RPCVD). The density of the e-beam evaporated and the RPCVD silica were measured using x-ray reflectivity (XRR) in PANalytical X'Pert PRO MRD. E-beam evaporated silica resulted in a less dense silica (2.08 g/cm^3) compared to RPCVD silica (2.20 g/cm^3) which were both less dense than the theoretical density value of the thermally grown α-quartz SiO_2 (2.65 g/cm^3). Therefore, e-beam evaporation was chosen to deposit the silica layer for devices.

There are two main ways to dope the silica layer with copper, another important step for optimization, which are "delta-doping" and "electrode-diffusion-doping"

(displayed in Figure 3.1). Because the Cu layer in electrode-diffusion-doping is exposed to air, a capping layer must be deposited on top of it before annealing, which is then removed post-annealing. It can also be annealed in vacuum to avoid oxidation of Cu, but this may be more challenging. Doping the SE layer with the AE material is done to improve the device performance as introducing AE material in the SE host takes care of the initial step of electrochemical oxidation of the AE [137]. It is also important to note that oxidation of the TE is unwarranted for these devices as the primary application is the memory application. Delta-doping is usually used for very thin SE layers (< 20 nm). Because the thickness of the silica layer was chosen to be 100 nm, electrode-diffusion-doping method was chosen.

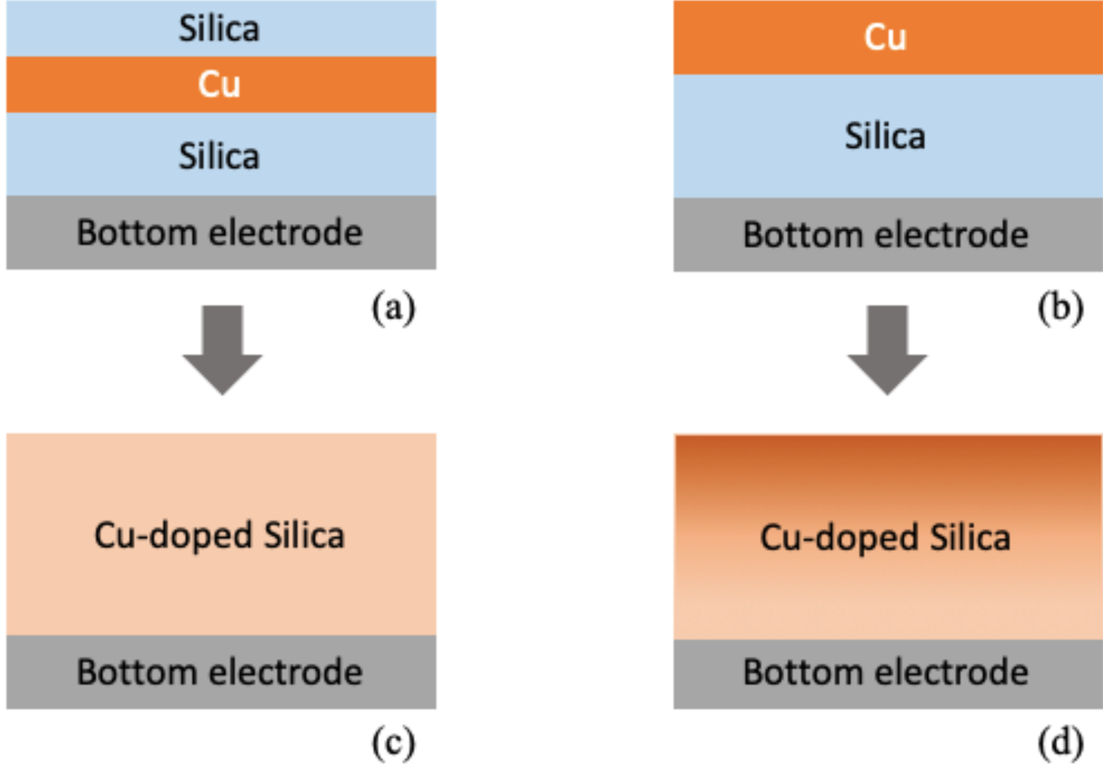

Figure 3.1: Cu doping techniques in Cu-SiO_x PMCs. (a, b) As-deposited, (c) and (d) post-annealing. Delta-doping (a→c), electrode-diffusion-doping (b→d).

In order to study the effects of the bottom electrode material, two different materials, W and Ni, were deposited while all the other fabrication parameters such as deposition technique and layer thicknesses were kept the same. Then, in order to find out the effect of the annealing temperature on the PMCs, the cathode material was kept the same, W, and the annealing temperature was varied from 400 °C up to 550 °C in 50 °C increments for 10 minutes. The fabrication process is detailed below in Figures 3.2-8. The devices were characterized electrically using an Agilent 4156C, and cross-sectional TEM images were obtained along with EDX analysis using JEOL ARM200F. TEM sample preparation was done by focused ion beam (FIB) cut.

3.2 Fabrication of Cu-SiO_x PMC Devices

Starting with a 4-inch Si wafer, a 200-nm Si_3N_4 was deposited using low-pressure chemical vapor deposition (LPCVD). This silicon nitride layer was used to isolate the wafer from the PMC. Then, the bottom electrode (60 nm), either W or Ni, was sputtered using Lesker PVD 75, shown in Figure 3.2. Then the cathode was patterned using photolithography, shown in Figure 3.3. Then, the cathodes were created by wet etching (W: $H_2O_2 + H_2O$; Ni: $HNO_3 + H_2O$), shown in Figure 3.4.

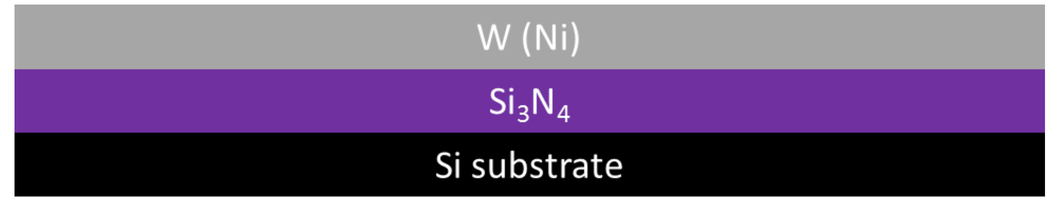

Figure 3.2: W (Ni) deposited on top of Si_3N_4/Si by sputtering.

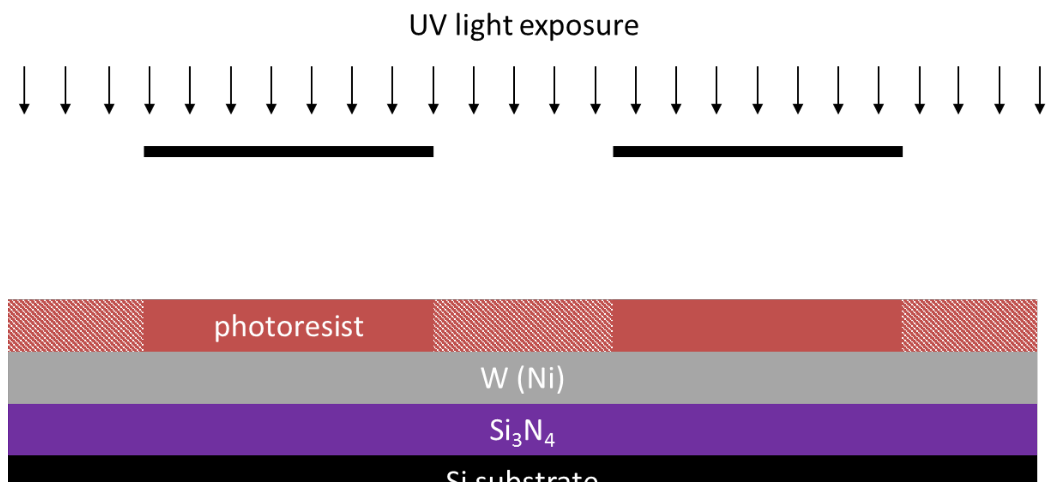

Figure 3.3: Cathode stripes patterning by photolithography.

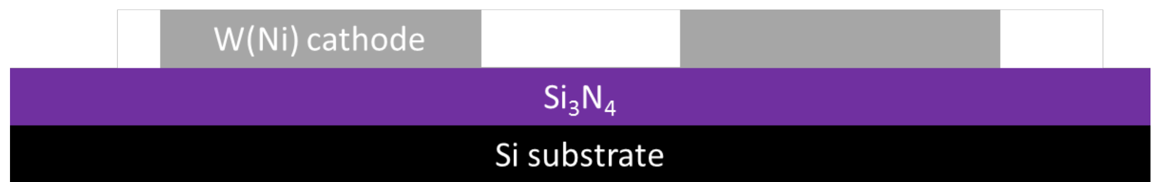

Figure 3.4: Wet etching to create the cathodes.

After the creation of cathodes, 100-nm switching layer, silica, was deposited using e-beam evaporation, shown in Figure 3.5. Then, 150 nm of Cu, was deposited using e-beam evaporation, which was then patterned by photolithography, and wet-etching ($NH_4OH+H_2O_2+H_2O$) was used to create the anode, shown in Figure 3.6.

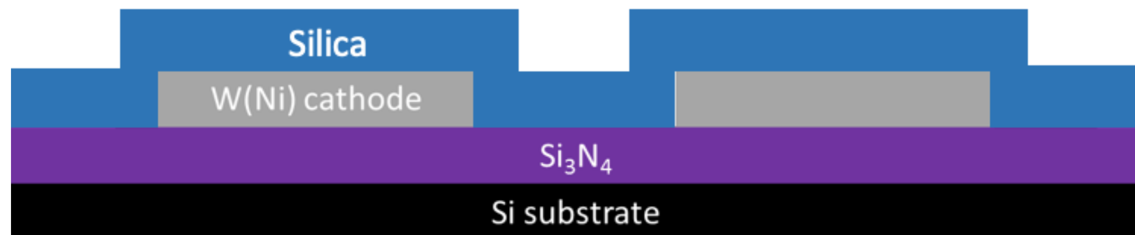

Figure 3.5: Switching layer deposition by e-beam evaporation.

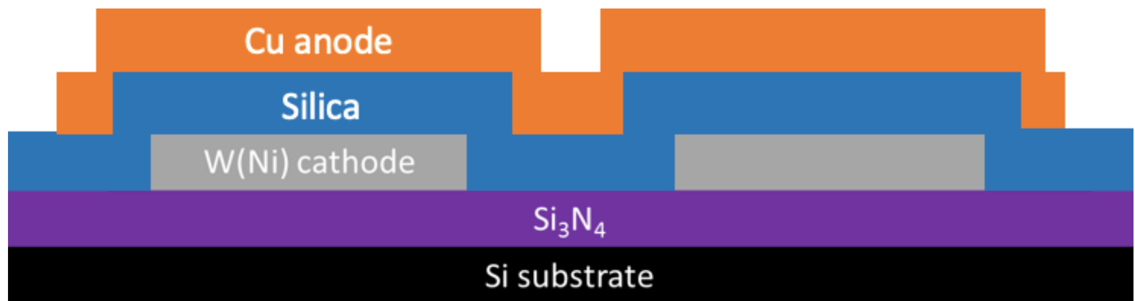

Figure 3.6: Anode creation after wet etching.

After the deposition and patterning of the Cu anode, a 500 nm-thick capping silica layer was deposited on top by e-beam evaporation, shown in Figure 3.7. This step was done in order to prevent the oxidation of the copper layer during annealing. Instead of this step, the annealing could also be carried out in a vacuum chamber as copper does not oxidize under vacuum pressure.

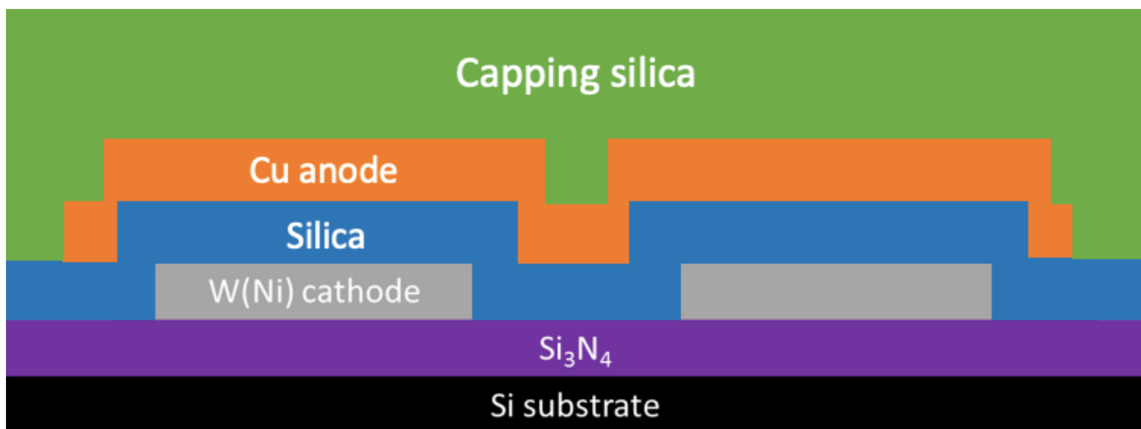

Figure 3.7: Deposition of capping silica layer by e-beam evaporation.

The devices were annealed at 400 °C - 550 °C for 5 or 10 minutes with continuous N_2 gas flow. After the annealing process, the devices, which were in a 32 x 32 crosspoint array, were patterned one last time by photolithography, and wet etching (HF + H_2O) was done for contact pad exposure. The idealized cross-section of the final structure is shown in Figure 3.8.

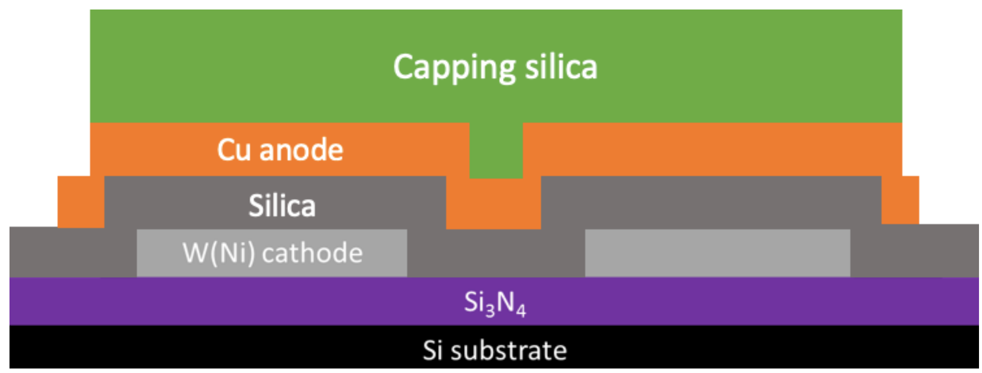

Figure 3.8: Idealized cross-section of the devices.

3.3 Electrical Characterization

Forming (electroforming) voltage (V_F) and initial resistance (read at 10 mV) of four annealed devices at 450 °C and 550 °C for 5 and 10 minutes were measured (32 total measurements). PMCs with Ni cathode (Ni-based devices) had much higher V_F than PMCs with W cathode (W-based devices) for both thermal conditions. The results are summarized in Figures 3.9-12. Detailed discussion on the electrical results is given in 3.6.

Electroforming is a one-time necessary event for reversible switching. After electroforming, set process of devices generally requires much less power. In order to overcome the hurdle of high V_F, the size of the nearby circuits and transistors needs to be larger. This can lead to lower memory density as the available area for memory devices will shrink. Because electroforming is a one-time event, sacrificing memory density due to high V_F is inefficient. Therefore, devices with lower V_F are more desirable in order to maximize the performance of the chip.

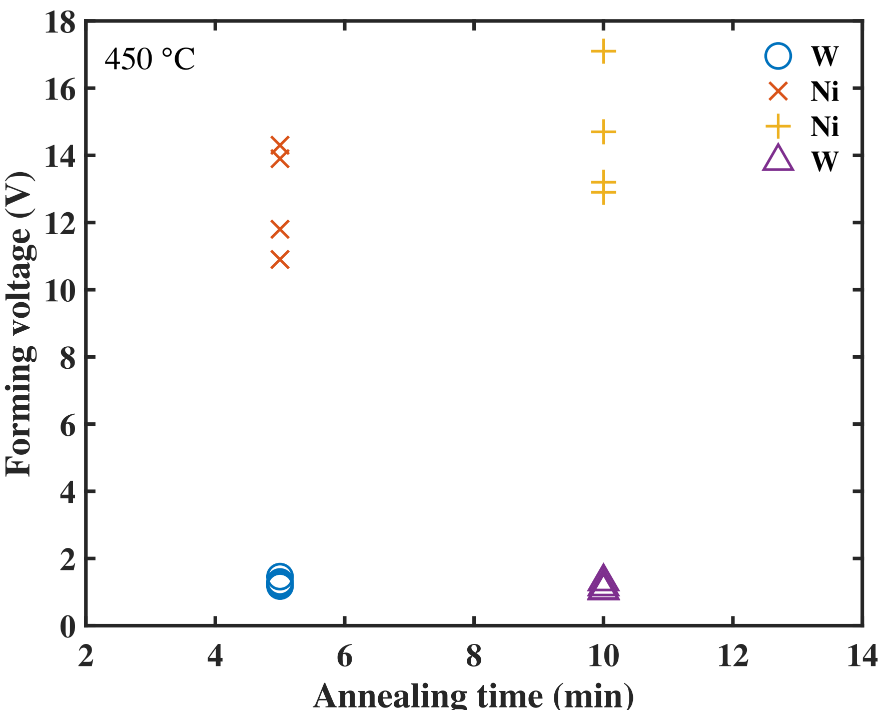

Figure 3.9: Forming voltage vs. annealing time for devices annealed at 450 °C.

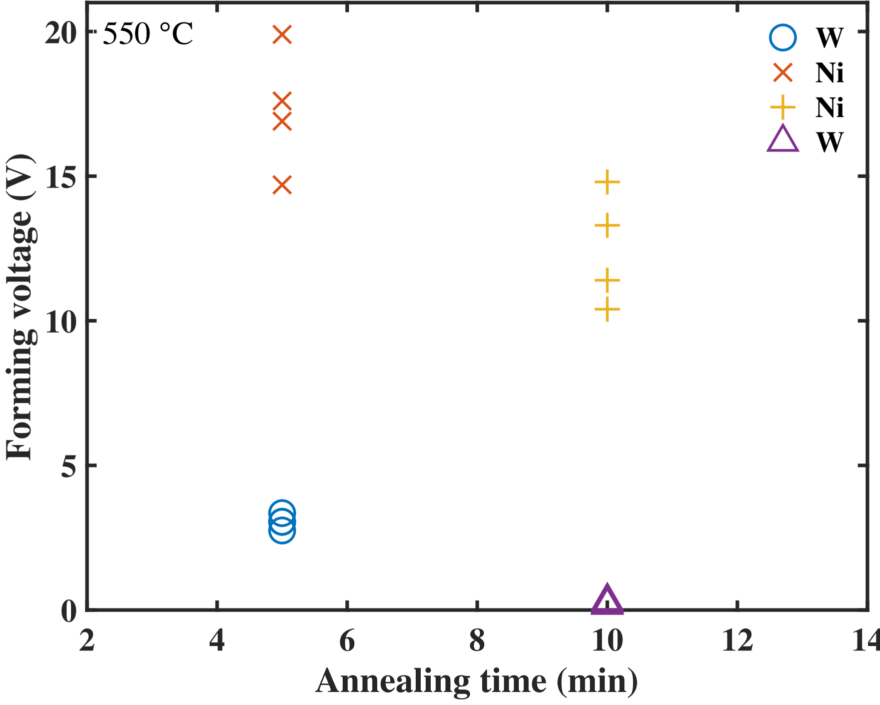

Figure 3.10: Forming voltage vs. annealing time for devices annealed at 550 °C.

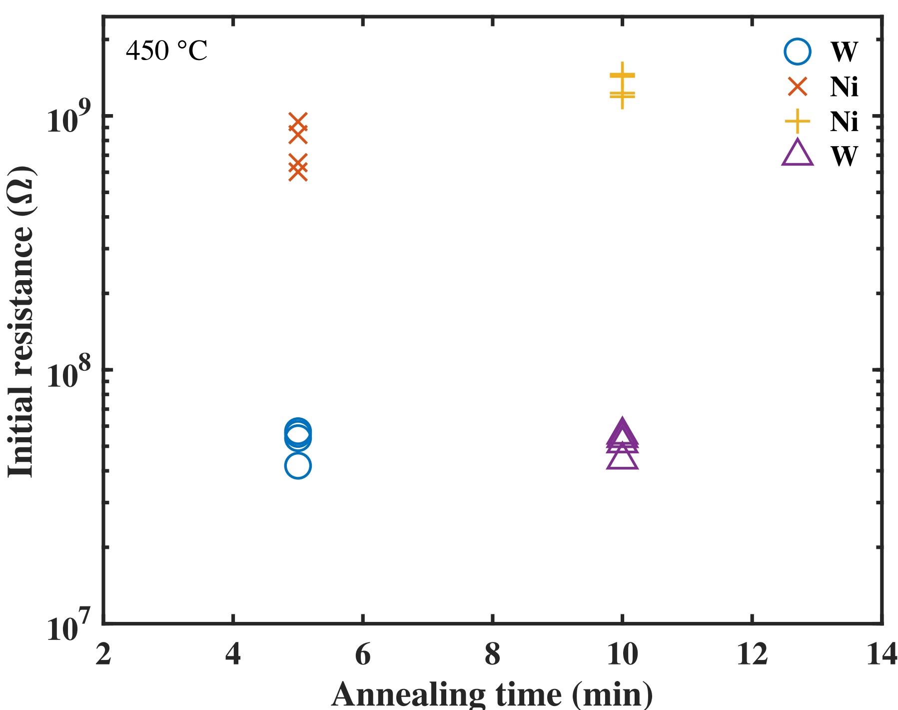

Figure 3.11: Initial resistance vs. annealing time for devices annealed at 450 °C.

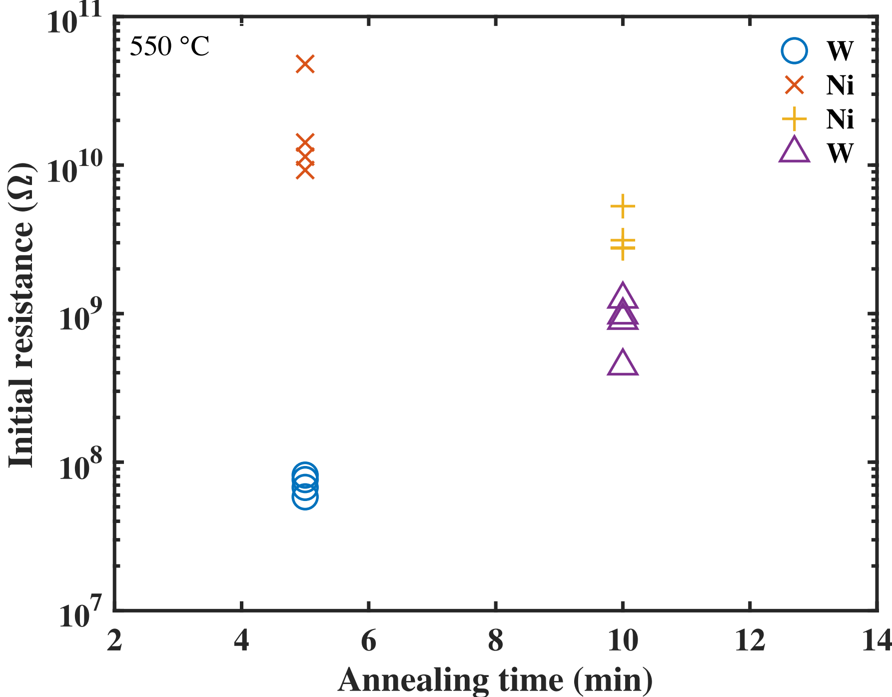

Figure 3.12: Initial resistance vs. annealing time for devices annealed at 550 °C.

A retention test (1200 seconds, read at 50 mV) was also done on the device with tungsten as CE which was annealed at 500 °C for 10 minutes and it is presented in Figure 3.13. Average resistance of the LRS and HRS was about 4.3 kΩ and 40 kΩ respectively in Figure 3.13. R_{OFF}/R_{ON} of about 10 was achieved which is one of the important parameters. Figure 3.14 shows the I-V characteristics of the forming process of the W-based devices for different annealing temperatures. V_F increases with annealing temperature until 500 °C and then decreases significantly at 550 °C. Assuming that the effect of process variation is negligible at this point, it is clear that the annealing process caused differences in the electrical results.

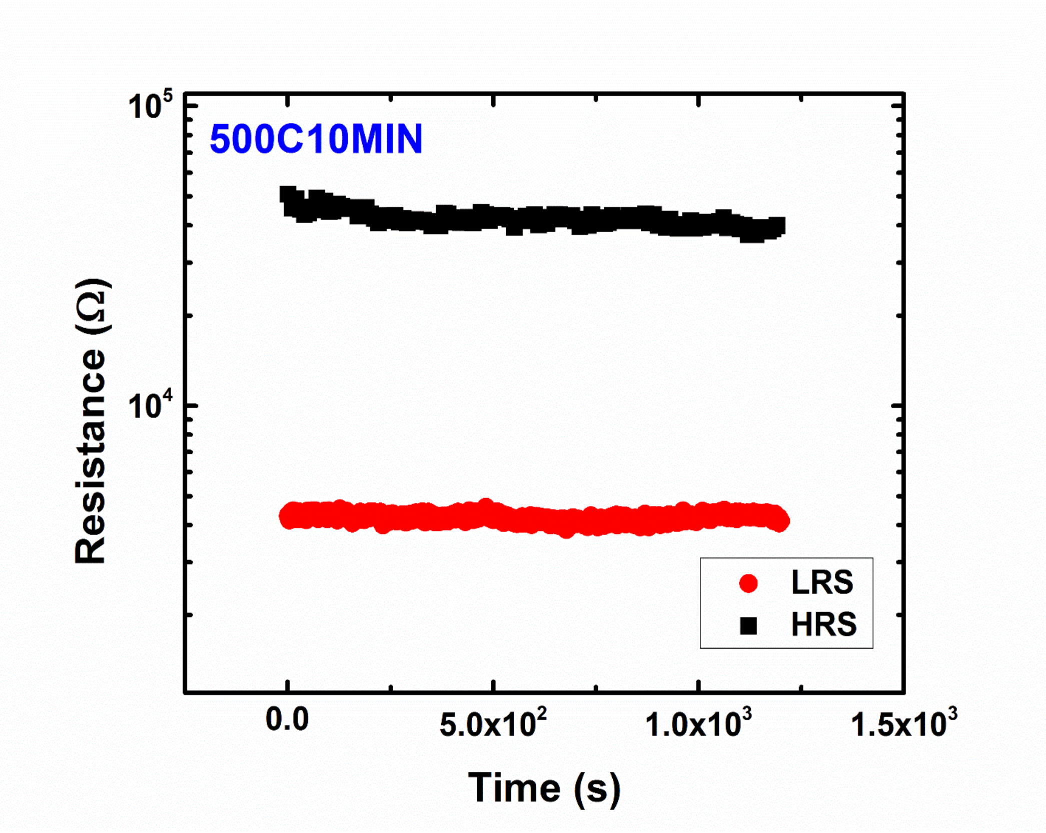

Figure 3.13: Retention test on $W/SiO_x/Cu$ device annealed at 500 °C for 10 min.

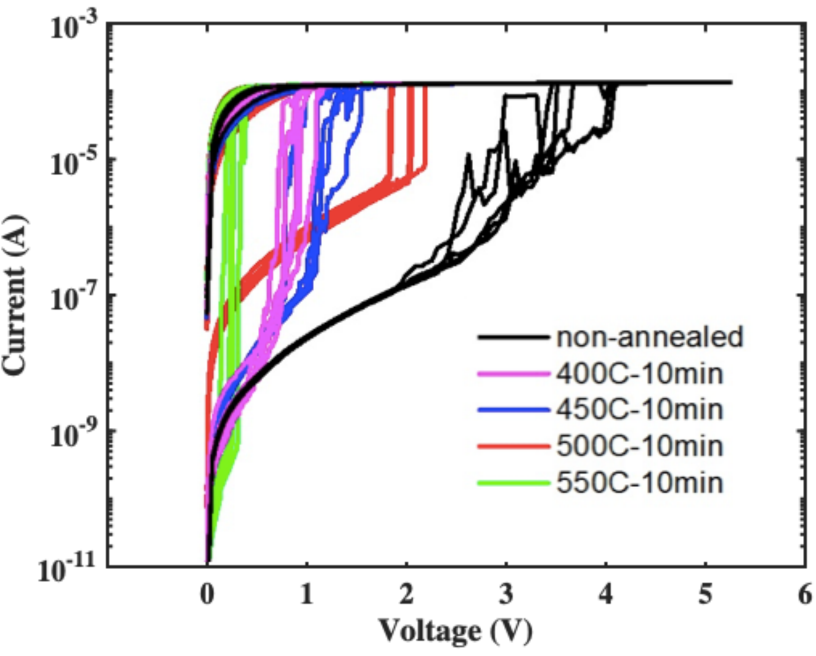

Figure 3.14: I-V characteristics of the forming process in W/SiO_x/Cu PMCs.

3.4 Material Characterization (TEM & EDX)

In order to further understand the effects of annealing, TEM imaging with EDX was utilized. The results are shown in Figures 3.15-21.

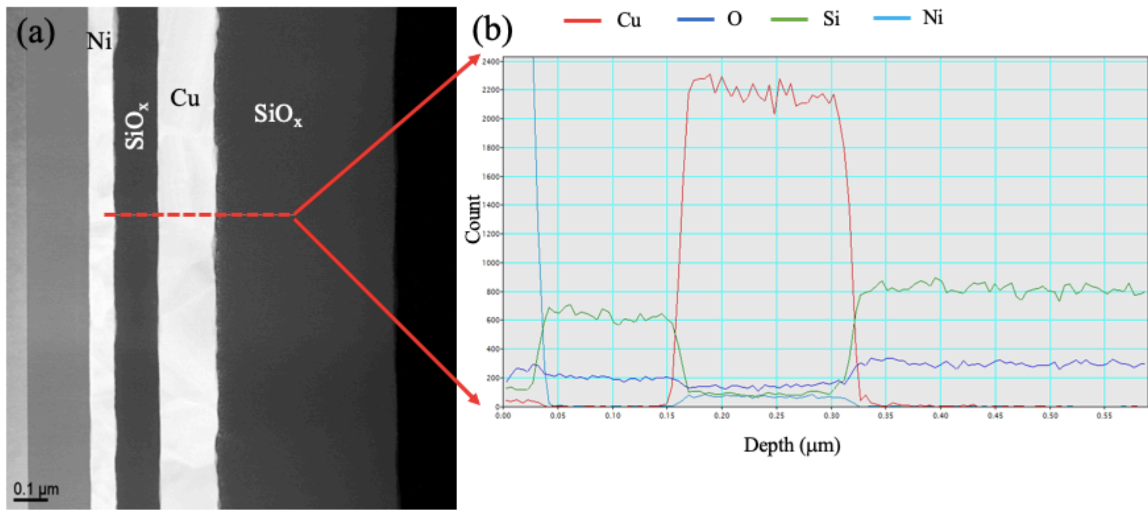

Figure 3.15: (a) TEM cross-section image of Ni/SiO_x/Cu/SiO_x annealed at 550 °C for 10 minutes, (b) EDX line scan result of the dashed line.

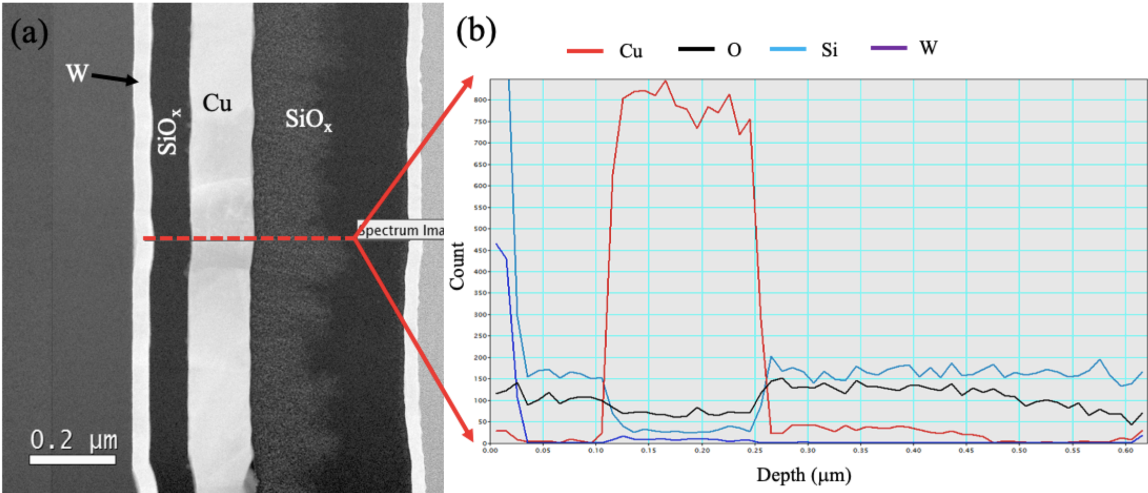

Figure 3.16: (a) TEM cross-section image of $W/SiO_x/Cu/SiO_x$ annealed at 550 °C for 10 minutes, (b) EDX line scan result of the dashed line.

TEM and EDX analysis, Figures 3.15-16, showed Cu diffusion into the capping SiO_x and the switching SiO_x layer following annealing in both cases. Furthermore, for both types of devices, Cu diffused through the SE and resided at the CE/SE interface. This is most likely due to the higher density of defects at the interface. EDX also showed that there is more Cu within the SE (even though it is a small difference) for the W-based device compared to the PMC with Ni as CE. Higher Cu concentration in $W/SiO_x/Cu$ PMC explains both the lower initial resistance and the lower forming voltage compared to the $Ni/SiO_x/Cu$ PMC. The only difference between the two PMCs were the cathode material. Possible explanation of the significant differences is given further in 3.6.

Higher magnification TEM image of the $W/SiO_x/Cu$ annealed at 550 °C for 10 minutes (Figure 3.17) along with the EDX line scan show the Cu island formation at the Cu/SE interface. This annealing condition resulted in very small V_F values ~ 0.25 V and it is believed that these islands play a role in this dramatic decrease in the V_F values. It is

clear in Figure 3.20 that while annealing at 550 °C instigates Cu island formation at the Cu/SiO_x interface for the W/SiO_x/Cu, annealing at 400 °C does not. Cu islands also did not form for the Ni/SiO_x/Cu device that was annealed at 550 °C for the same duration.

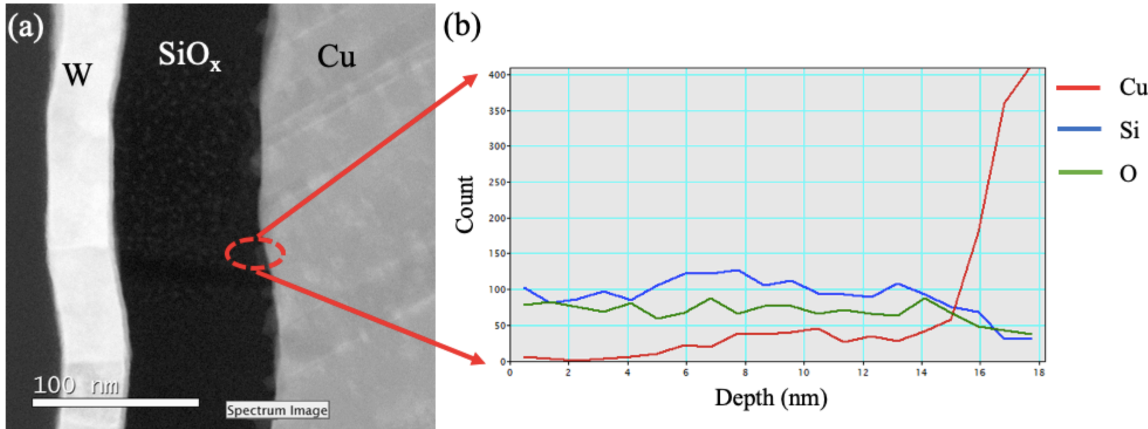

Figure 3.17: (a) TEM cross-section image of W/SiO_x/Cu annealed at 550 °C for 10 minutes, (b) EDX line scan result within the dashed circle.

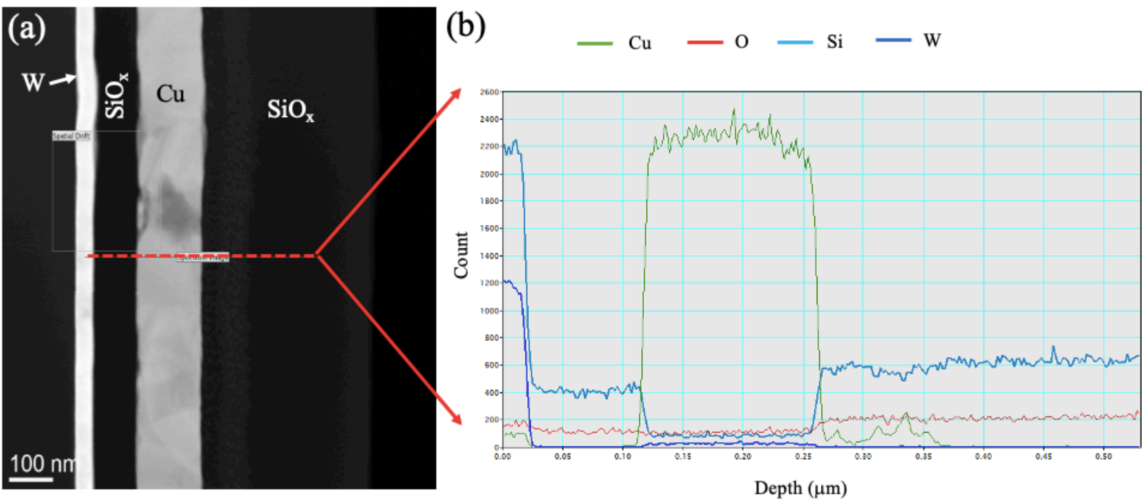

Figure 3.18: (a) TEM cross-section image of W/SiO_x/Cu/SiO_x annealed at 400 °C for 10 minutes, (b) EDX line scan result of the dashed line.

TEM and EDX analysis of W-based PMCs annealed at 400 °C is displayed in Figures 3.18 and 3.19. Compared to the cells annealed at 550 °C, Cu diffusion into the SE is much less,

if at all. Given that the V_F of the devices annealed at 400 °C is larger than the devices annealed at 550 °C, this behavior was expected.

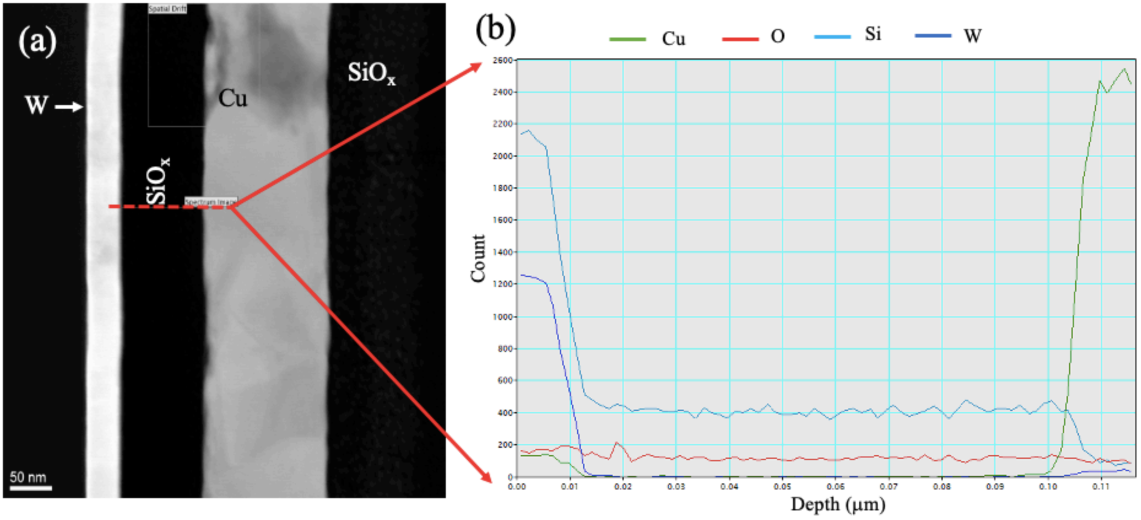

Figure 3.19: (a) TEM cross-section image of W/SiO_x/Cu/SiO_x annealed at 400 °C for 10 minutes, (b) EDX line scan over the switching layer.

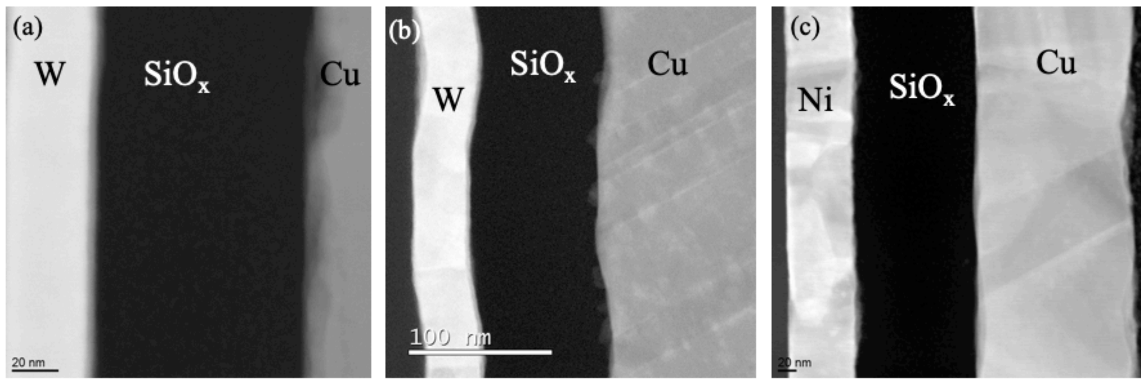

Figure 3.20: TEM cross-section image of the devices annealed for 10 minutes. (a) W/SiO_x/Cu at 400 °C, (b) W/SiO_x/Cu at 550 °C and (c) Ni/SiO_x/Cu at 550 °C.

3.5 Statistical Analysis of Forming Voltage

The statistical analysis of the V_F results was carried out by the software JMP. The analysis includes the analysis of variance (ANOVA) table, effects estimate summary for the factors, ranking of importance of factors and normal probability plot that can help

explain the effects better. Note that the design is replicated 4 times and the numbers at each corner of the cube plots denotes the average of all replicates for that treatment combination. CE material (W and Ni) is not used as an independent variable (IV) as having it as an IV violates the assumption of equal variances.

The cube plot for the 2^2 design with 4 replicates for the PMCs with W as the CE is shown in Figure 3.21. Table 3.1 and 3.2 show the ANOVA table and the effect estimate summary respectively. It is clear from Table 3.2 that both of the main effects, temperature and time, and the interaction of them are statistically significant.

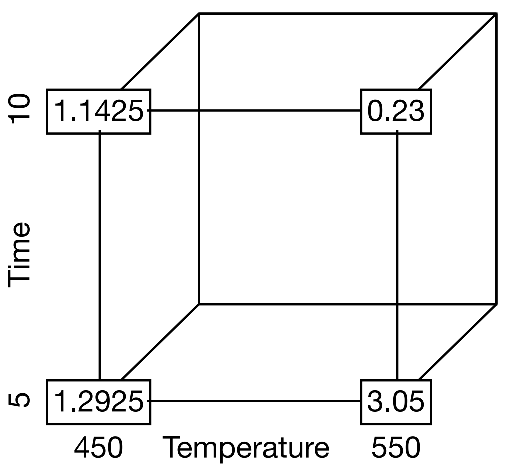

Figure 3.21: Cube plot, CE: W (2^2 design replicated 4 times).

Table 3.1: ANOVA (CE: W)

Source	DF	Sum of Squares	Mean Square	F Ratio
Model	3	16.663825	5.55461	237.588
Error	12	0.280550	0.02338	**Prob > F**
C. Total	15	16.944375		<.0001*

Table 3.2: Effect Estimate Summary (CE: W)

Term	Estimate	Std Error	t Ratio	Prob>|t|
Intercept	1.54375	0.400914	3.85	0.0023*
Temperature	0.004225	0.000765	5.53	0.0001*
Time	-0.297	0.01529	-19.42	<.0001*
(Temperature-500)*(Time-7.5)	-0.00534	0.000306	-17.46	<.0001*

The ranking of the importance of the factors by the analysis is given in Table 3.3 and it shows that annealing time is the most important variable followed by the interaction of time and temperature and the least important factor is the annealing temperature. Normal probability plot (Figure 3.22) shows that the data is adequately described by normal distribution.

Table 3.3: Ranking of the Importance of the Factors (CE: W)

Source	LogWorth		PValue
Time	9.707		0.00000
Temperature*Time	9.170		0.00000
Temperature	3.884		0.00013

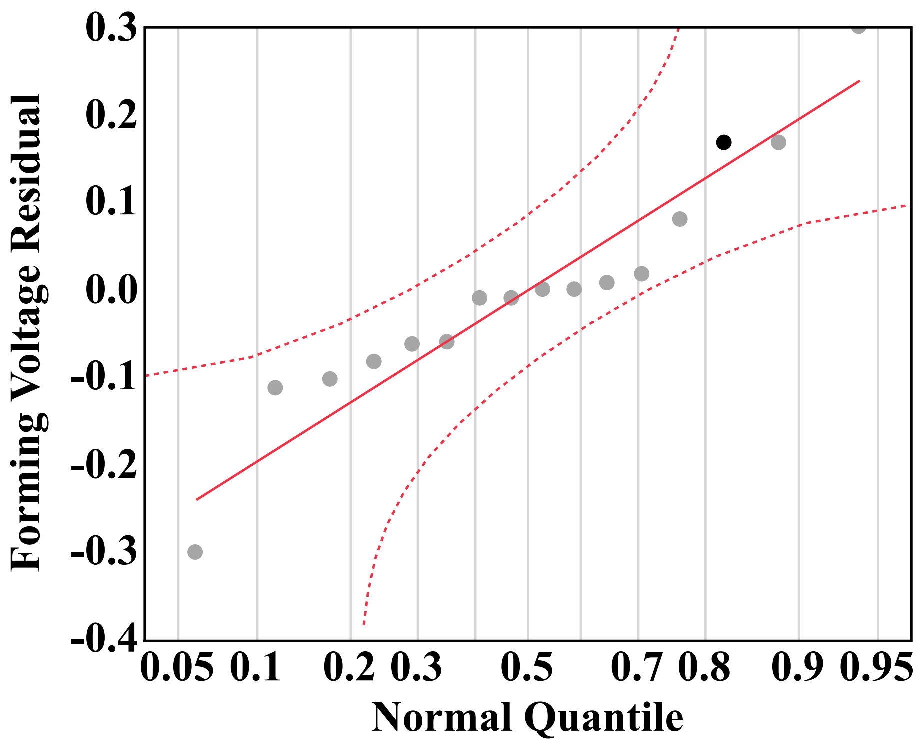

Figure 3.22: Normal probability plot for V_F (CE: W).

The cube plot for the 2^2 design with 4 replicates for the PMCs with Ni as the CE is shown in Figure 3.23. Table 3.4 and 3.5 show the ANOVA table and the effect estimate summary respectively. It is clear from Table 3.5, unlike the W-based PMCs, only the interaction between annealing time and temperature is statistically significant.

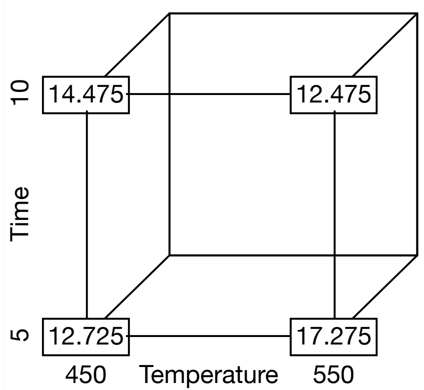

Figure 3.23: Cube plot, CE: Ni (2^2 design replicated 4 times).

Table 3.4: ANOVA (CE: Ni)

Source	DF	Sum of Squares	Mean Square	F Ratio
Model	3	58.7075	19.5692	5.2878
Error	12	44.4100	3.7008	**Prob > F**
C. Total	15	103.1175		0.0149*

Table 3.5: Effect Estimate Summary (CE: Ni)

Term	Estimate	Std Error	t Ratio	Prob>|t|
Intercept	10.15	5.044128	2.01	0.0672
Temperature	0.01275	0.009619	1.33	0.2097
Time	-0.305	0.192376	-1.59	0.1389
(Temperature-500)*(Time-7.5)	-0.0131	0.003848	-3.40	0.0052*

The ranking of the importance of the factors by the analysis is given in Table 3.6 and it shows the interaction of annealing time and temperature is the most important (the only significant) factor. Normal probability plot (Figure 3.24) shows that the data is adequately described by normal distribution.

Table 3.6: Ranking of the Importance of the Factors (CE: Ni)

Source	LogWorth	PValue
Temperature*Time	2.282	0.00522
Time	0.857	0.13885 ^
Temperature	0.678	0.20968 ^

^ denotes the effects with containing effects above them

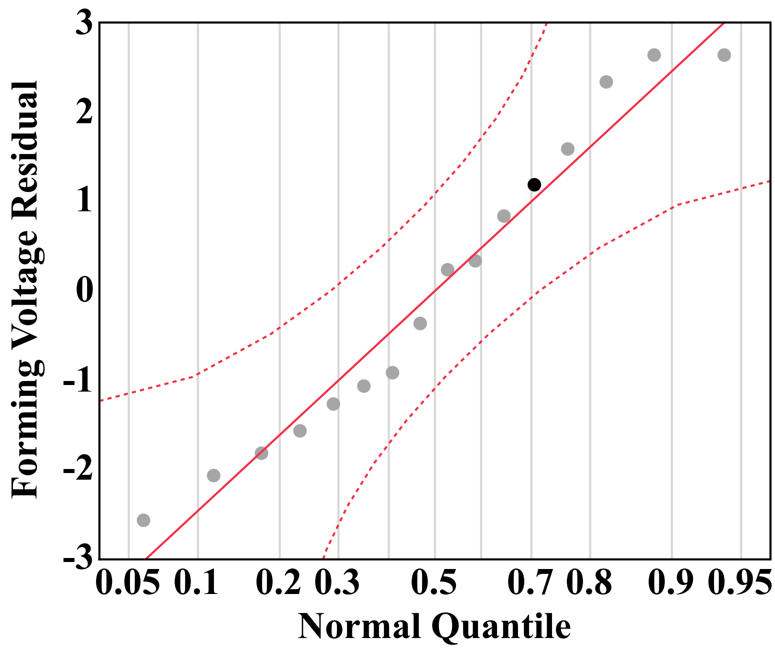

Figure 3.24: Normal probability plot for V_F (CE: Ni).

3.6 Discussion

It is interesting to see that the results of the statistical analysis show that the factors and their impact on the forming voltage results differ between the two CE materials. When PMCs have tungsten as the CE, annealing temperature, annealing time and the interaction between them all have significant impact on the V_F. However, when the PMCs have nickel as the CE, only the interaction between the annealing temperature and time shows up as the significant factor. This means that it was easier to impact the V_F of W-based devices by tweaking the annealing conditions, but for Ni-based devices, careful adjustment of both needed to be done.

The only difference was the CE materials and the large difference between the V_F values can be explained due to this difference. Sputtering of the CE will result in different surface roughness at the CE/SiO_x. Because W has a higher melting temperature (3422 °C)

than the melting temperature of Ni (1455 °C), W layers will have a much rougher surface [140]. This increase in roughness suggest greater self-shadowing effects during the SiO_x evaporation [141] and there could be more columnar structures within the SE [142]. Because the e-beam evaporation of the SE was done at room temperature, well below the temperature that would assist with the surface diffusion and enhance uniformity [143], [144], this effect could be even further enhanced. These columnar structures within the SE provide favorable regions for the filament formation [145] and result in less dense (more porous) regions. Even though increased porosity has been shown to decrease local Cu^{z+} mobility in materials such as SiCOH [146], [147], in SiO_x thin-film PMCs, which are also columnar, the grain boundaries significantly enhances Cu^{z+} mobility [148]–[150]. Also, more moisture can be absorbed in these less dense regions which serves as "dissolving agent" improving ion mobility [145]. Both electrodes were created by wet etching which can lead to moisture related defects (H^+ and OH^-) in the SE [131] coming from the electrode/SE interfaces. Another important role of moisture is to provide the counter charge reaction (equation 3.1) at the SE/CE to Cu^{z+} ionization happening at the AE/SE interface to electroform or set the device [151].

$$2H_2O + 2e^- \rightarrow H_2 + 2OH^- \quad (3.1)$$

This effect of moisture on the V_F decreasing with density was also previously reported for $Cu/Ta_2O_5/Pt$ and $Cu/SiO_2/Pt$ devices [70]. Furthermore, the columnar structures in the SE were also stated as the preferred location for filament formation and AE material-rich regions in $Ag/Ge_{40}S_{60}/Pt$ PMC devices [66].

It is also clear that different annealing conditions also lead to different V_F values. It is expected that higher annealing temperatures can lead to densification of the SiO_x layer

[152] and reduction of defects [153], both of which can lead to increase in V_F values. Extended annealing time can also lead to densification of the SiO_x layer by promoting Si-O cross linkage [152]. This effect, in fact, was observed in Cu/sputtered-SiO_2 by XRR measurements in PMC devices up to 600 °C [154]. Prolonged annealing and/or higher annealing temperatures can not only densify the SiO_x layer, but also can enhance Cu diffusion into the SE [67]. These two will lead to conflicting behaviors in the expected V_F shifts. Puthen Thermadam et. al. [67] investigated the effects of annealing temperature on Cu diffusion in the e-beam SiO_x at higher temperatures, 560°C – 720 °C, and found out that Cu concentration in the SiO_x increased with annealing temperature. It is clearly seen in Figure 3.14 that increased annealing temperature results in rise in V_F from 400 °C to 500 °C, and then a drastic decrease at 550 °C for 10-minute annealing duration. Therefore, it is believed that the effect of the densification of the SiO_x layer is more pronounced than increased Cu diffusion in the temperature range of 400°C - 500 °C. But, annealing at 550 °C for 10 minutes, Cu diffusion is greatly enhanced which lowers the V_F. In fact, this effect can evidently be seen in Figure 3.17, 3.20a and b where annealing at 550 °C led to significantly more Cu in the SiO_x and Cu island formation at Cu/SiO_x interface for W-based device. When the annealing time was only 5 minutes, the impact of densification was still the dominant factor over Cu diffusion.

CE material and annealing conditions also influence the initial resistance of a PMC. Initial resistance of a cell should be dictated by the resistance of the SiO_x layer as the resistance of both electrodes will be much smaller. Moreover, increased Cu inclusion in the SiO_x will further decrease the initial resistance. W-based devices have lower initial resistance values compared to the Ni-based devices. As discussed earlier, TEM and EDX

results show more Cu in the SiO_x layer for W-based devices. Also, they are prone to having more defects in the SiO_x layer. When large number of defects cluster together in certain regions, TEM studies show that Si nanocrystals can form in the SiO_x [155]–[157], and this also can lead to drastic reduction in the initial resistance. Figure 3.11 shows that annealing at 450 °C for different durations does not significantly alter the initial resistance value. However, when annealed at 550 °C, W-based devices show increase in the initial resistance with increased annealing time unlike the devices with Ni as the CE which display a decrease. Higher annealing temperature, for W-based devices, instigates Cu island formation at the AE/SE interface. Given that the W-based devices would possibly have more columnar structures as discussed earlier, this island formation ("clustering") is conceivably due to Cu gathering together in these defective spots instead of more uniform doping. This clustering causes a very thin layer (~5-10 nm) near the AE/SE to have low resistance but leads to higher resistance throughout the rest of the SE which would still dominate the overall initial resistance leading to higher resistance values.

Because Cu/SiO_x/Ni devices result in significantly larger V_F values, W is the recommended CE here for low-power applications. Further improvements, however, can be made if Ni is the desired material for CE. Such improvements can be made by optimizing the annealing conditions such as changing the annealing temperature range and/or duration. More research can also be done to check the effects of the different gases used during annealing as the gas ambient is shown to have an impact [158] as well. Moreover, different thickness for the SE layer can be considered as the V_F value should decrease with the thickness of the SE [159].

CHAPTER 4

COPPER OXIDATION

4.1 Brief Review of Copper Oxidation

Copper (Cu), Copper (I) Oxide (cuprous oxide, cuprite – Cu_2O) and Copper (II) Oxide (cupric oxide, tenorite – CuO) are some of the widely used materials. Copper is used in the semiconductor industry as the interconnect material due to its lower resistivity [160]. Cu_2O has been extensively studied and used in large-area electronics such as solar cells [161], spintronics [162] and catalysis [163], while CuO gained interest in photo-thermal and photoconductive applications [164] as well as high temperature (T_c) superconductivity [165]. Cu_2O has a cubic structure and it is a p-type semiconductor with a bandgap in the range of 1.8 – 2.5 eV, while CuO has a monoclinic structure and it is a p-type antiferromagnetic semiconductor with a bandgap in the range of 1.2 – 2.0 eV [166], [167]. Copper can oxidize, although slowly, even at room temperature [168] and this is one of the main obstacles in the nanoelectronics. But, due to the versatility in applications, Cu-based materials attract more and more researchers. For further data, the standard thermodynamic properties of Cu_2O and CuO are given in Table 4.1 [169].

Table 4.1: Standard Thermodynamic Properties of Cu_2O and CuO.

Formula	$\Delta H_f°$ (kJ/mol)	$\Delta G_f°$ (kJ/mol)	S° (J/K mol)
CuO	-157.3	-129.7	42.6
Cu_2O	-168.6	-146.0	93.1

Stable Cu-oxides can be found in two forms in nature, Cu_2O and CuO, while there are two other reported unstable forms, Cu_3O_2 and Cu_4O_3 [170], [171]. There are a few factors that control which Cu-oxide will be the oxidation product, but main two are

temperature and oxygen partial pressure [172]. Figure 4.1 shows the Cu-O phase formation in terms of temperature and oxygen partial pressure for samples annealed in air (past 500 °C combination of Cu_2O and CuO is reported at 1 atm) [167], [173]–[178]. Note that even though Cu_2O is considered to be unstable at room temperature, the transformation kinetics of it to CuO is too slow, so one can consider the cuprous oxide form as stable.

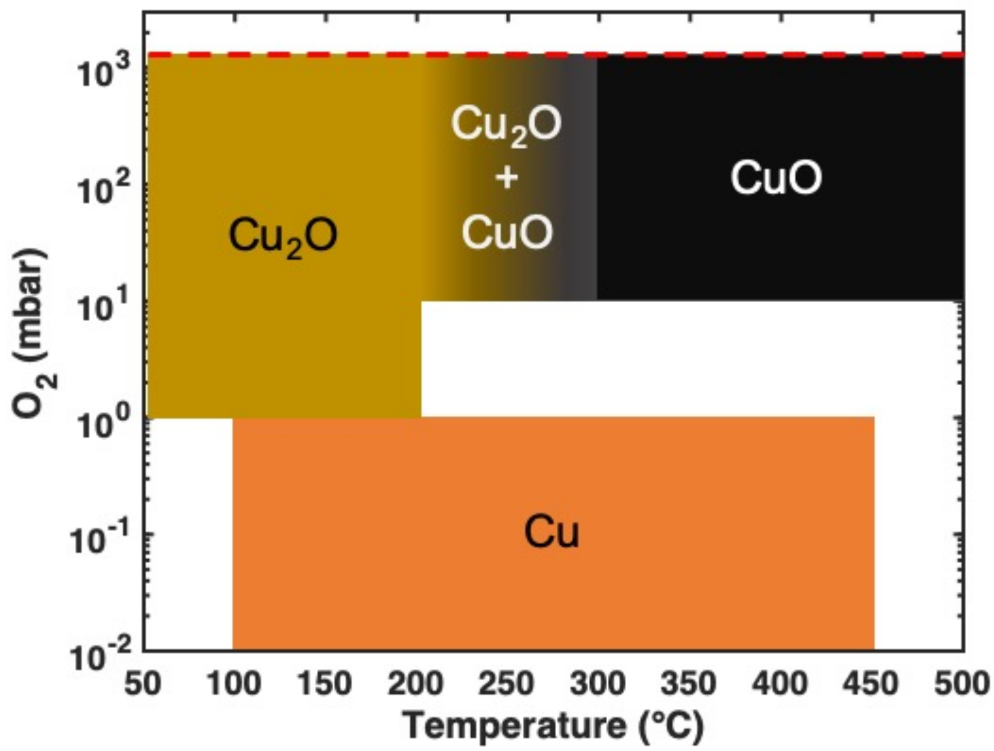

Figure 4.1: Cu-O phase formation for samples annealed in air [167], [173]–[178]. The yellow zone is Cu_2O, the black zone is CuO, the orange zone means that Cu does not oxidize. References are not found for the empty zones. Red dashed line indicates 1 atm.

A lot of research has been done over the years to study the oxidation kinetics of copper. Even though, the parabolic rate law is the most observed one [179]–[183], there are also other reported laws with regard to the kinetics such as logarithmic [176], [184], [185], inverse-logarithmic [186], linear [187], [188] and cubic law [186], [189]. Here, the rate law represents the relationship between the oxide thickness and the annealing time.

The corresponding formulas are given in Table 4.2 where d_{ox} is the oxide thickness, k_p is the rate constant, t is the annealing time, A, B and C are constants.

Table 4.2: Oxidation Kinetics Rate Law Formulas.

Rate Law	Formula
Linear	$d_{ox} = k_p \times t + C$
Parabolic	$d_{ox} = k_p \times t^{\frac{1}{2}} + C$
Cubic	$d_{ox} = k_p \times t^{\frac{1}{3}} + C$
Logarithmic	$d_{ox} = Aln(t) + B$
Inverse-Logarithmic	$\frac{1}{d_{ox}} = A - Bln(t)$

Overall, there has been no consensus on copper oxidation rates. However, there is an understanding of what factors contribute to the resulting oxide thickness. Some of these factors are temperature, oxygen partial pressure, the orientation of Cu, whether the Cu is single-crystal or polycrystalline, whether the Cu is a thin film or a bulk film, purity of copper, deposition technique, ambient gas where Cu is being oxidized and the surface roughness [18], [20]-[23], [27]–[33].

Oxide thickness depends on the oxygen partial pressure through the rate constant. At low pressures for Cu being oxidized into Cu_2O, the relation between the oxidation rate and oxygen partial pressure is $\propto p_{O2}^{1/7}$ and this is explained by the fact that the oxidation proceeds by charged oxygen vacancies. However, at higher pressures (such as close to atmospheric pressure), the dependence becomes $\propto p_{O2}^{1/4}$ and it is explained by the fact that oxidation proceeds by neutral copper vacancies [176], [196], [197]. It is also noted in [20] that even though the oxygen partial pressure changes the oxidation rate, it does not change the oxidation rate law.

Another important factor while studying and modeling the copper oxidation is the factor that accounts for the oxygen incorporation. When Cu oxidizes into Cu_2O, it follows equation (4.1); and when it oxidizes into CuO, it follows equation (4.2). Oxygen incorporation factors for each equation is 1.65 and 1.72 respectively [177]. For example, while full oxidation of 100 nm of Cu into Cu_2O will result in 165 nm of Cu_2O, it will result in 172 nm of CuO if it oxidizes into CuO.

$$2Cu\ (s) + 1/2O_2\ (g) \rightarrow Cu_2O\ (s) \tag{4.1}$$

$$2Cu\ (s) + O_2\ (g) \rightarrow 2CuO\ (s) \tag{4.2}$$

One of the main focuses of studying the oxidation kinetics of Cu is to find the activation energy of diffusion (E_a). This can be calculated by finding out the oxidation rate law and using the temperature dependence of the oxidation rate constant k_p which follows the Arrhenius equation (4.3) [198] where k_0 is a constant, R is the universal gas constant 8.314 J/K-mol (8.617×10^{-5} eV/K) and T is the annealing temperature.

$$k_p = k_0 \exp\left(\frac{-E_a}{RT}\right) \tag{4.3}$$

Plotting $\ln(k_p)$ vs. 1/T will result in a graph with the slope of $-E_a/R$ and from the same graph 1/T=0 intercept will give the $\ln(k_0)$ value. As one can expect, due to differences in a lot of variables such as temperature, oxygen partial pressure, orientation of copper, deposition technique etc., the reported E_a values are different from one another. The summary of E_a values in the literature is given in Table 4.3.

Table 4.3: Summary of the Activation Energy of Diffusion (E_a) Values.

Temperature Range (°C)	Deposition Technique	Resulting Oxide	E_a (eV)
180 – 260	Vacuum evaporation	Cu_2O	0.57 [180]
120 – 150	E-beam evaporation	Cu_2O	0.55 [181]
175 – 400	Sputtering	Cu_2O & CuO	0.31 [179]
40 – 60	Single crystal Cu#	Cu_2O	0.35 [176]
60 – 100	Single crystal Cu#	Cu_2O	0.93 [176]
120 – 160	Single crystal Cu#	Cu_2O	1.03 [176]
250 – 500	Bulk Cu coupons	Cu_2O & CuO	0.74 [186]
250	Evaporation	CuO	0.74 [199]
300 – 550	OFHC* Cu	Cu_2O & CuO	0.87 [200]
550 – 900	OFHC Cu	Cu_2O & CuO	1.63 [200]
300 – 500	99.9999% Cu	Cu_2O & CuO^	0.42 [201]
600 – 800	99.9999% Cu	Cu_2O & CuO^	1.15 [201]

Different annealing temperatures resulted in different oxidation rate laws
* OFHC= Oxygen-free high thermal conductivity
^ CuO growth was whisker-like

As it can be seen from Table 4.3, the reported activation energy differs quite largely with different Cu samples, different deposition techniques, and annealing temperatures. In addition to these factors, the list of variables mentioned previously plays a big role in the oxidation kinetics which results in different activation energies. The transition from Cu_2O to CuO requires one additional oxygen incorporation into the lattice. In addition to the change in structure, the second ionization potential of the Cu atoms must be overcome. Therefore, higher energy (temperature) is needed for CuO to form which results in usually a higher activation energy for CuO [177] even though the heat of formation values are comparable.

It is also important to note here that thin film copper oxidation is a little more complicated. At the initial stages of oxidation at low temperatures, surface diffusion of oxygen is the dominating factor [202], [203]. However, after about 10 nm of copper-oxide is formed, the Cu cation diffusion becomes the limiting factor [204]. Furthermore, the

outward diffusion of Cu cations can introduce inward diffusion of copper vacancies, which is also known as the Kirkendall effect and the number of vacancies will be proportional to the thickness of the resulting oxide [205], [206].

4.2 Oxidation Phases and Kinetics of E-beam Evaporated Copper at Low Temperatures

The samples used to study the oxidation phases and kinetics of copper were Cu (150 nm)/Si_3N_4 (200 nm) deposited on a silicon wafer seen in Figure 4.2 (control sample). Starting with a silicon wafer, a layer of Si_3N_4 was deposited using low-pressure chemical vapor deposition (LPCVD). Copper was e-beam evaporated on top of Si_3N_4/Si using Lesker PVD75 under base pressure 5×10^{-6} Torr at room temperature. The evaporation rate was 1 Å/s with the holding plate rotating for good film uniformity.

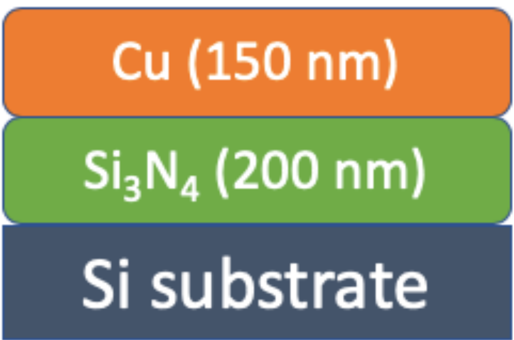

Figure 4.2: Control sample for oxidation experiments.

The annealing was done in air and the temperatures were varied from 125 °C to 170 °C and the annealing time varied from 30 minutes to 90 minutes. Annealing causes copper to oxidize from the top and Cu_2O was formed which was verified by both XPS and XRD and the final sample structures are shown in Figure 4.3. Due to different annealing times and temperatures, the oxide thickness was different in each sample.

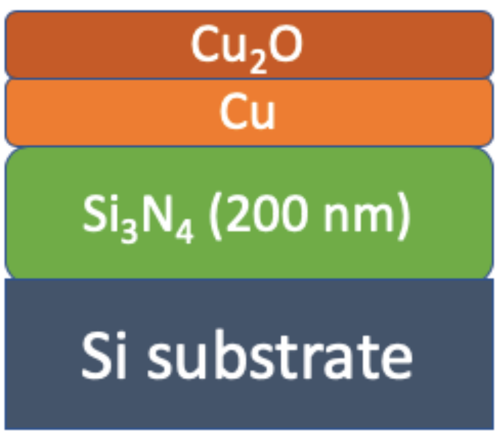

Figure 4.3: Copper oxidation samples after annealing.

4.2.1 XRD

Samples were studied by x-ray diffraction (XRD) using Cu-Kα radiation (λ=0.15406 nm) on Bruker D8 Specialized Powder X-ray Diffractometer with detector scan configuration. The incident beam angle was set to ω=2° and the slit used was 0.6 mm. Figure 4.4 shows the XRD patterns of copper control sample along with the samples annealed at 125 °C, 140 °C, 155 °C and 170 °C for 70 minutes. Figure 4.5 shows the XRD patterns of copper annealed at 125 °C for 30 minutes, 50 minutes and 70 minutes. Figure 4.6 shows the XRD patterns of copper annealed at 155 °C for 30 minutes, 50 minutes and 70 minutes. PDF-04-009-2090 card shows for Cu to be in a cubic structure with Cu (111), Cu (200), and Cu (220) peaks at 43.46°, 50.62°, and 74.40° respectively. PDF-04-007-9767 card shows Cu_2O to be in a cubic structure with Cu_2O (111), Cu_2O (200), and Cu_2O (220) peaks at 36.43°, 42.31°, and 61.38° respectively. The density of the e-beam evaporated Cu layer was measured using XRR and the it was determined to be 8.85 g/cm^3 which is lower than the density of the theoretical Cu (8.96 g/cm^3). The defects (e.g. vacancies) in the deposited Cu layer were believed to lead to unit cell reduction which caused peak shifts

towards the higher angles. With this effect in mind, the XRD peaks were labeled accordingly. Copper before annealing was observed to be in cubic structure and annealing at different low temperatures and times resulted in formation of Cu_2O cubic structure. Furthermore, calibration sample (alumina) was also analyzed at the same incidence angle to find out the effect of the instrument. It was found that the peaks were shifted additionally by $2\theta = +0.22°$. Even though the XRD settings such as the incident beam angle did not change, a Si_3N_4 peak was observed for the oxidation sample annealed at 170 °C for 70 minutes. This is due to the relationship between the intensity (I) and the linear absorption coefficient (μ), $I \propto \exp(-\mu L)$, where L is the distance that x-ray beam travels [207]. Linear absorption coefficient is inversely proportional to the atomic weight. Because Cu_2O has a higher atomic mass (143.09 g/mole) than Cu (63.54 g/mole), x-rays can travel further into the sample and interact with the Si_3N_4 layer.

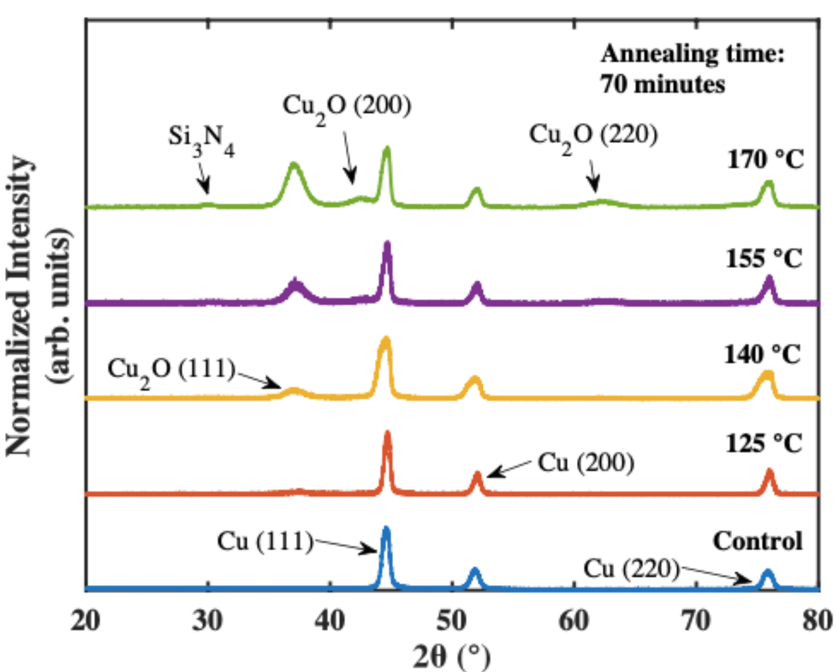

Figure 4.4: XRD patterns of Cu control sample and increasing temperatures. Samples annealed for 70 minutes at 125 °C, 140 °C, 155 °C and 170 °C.

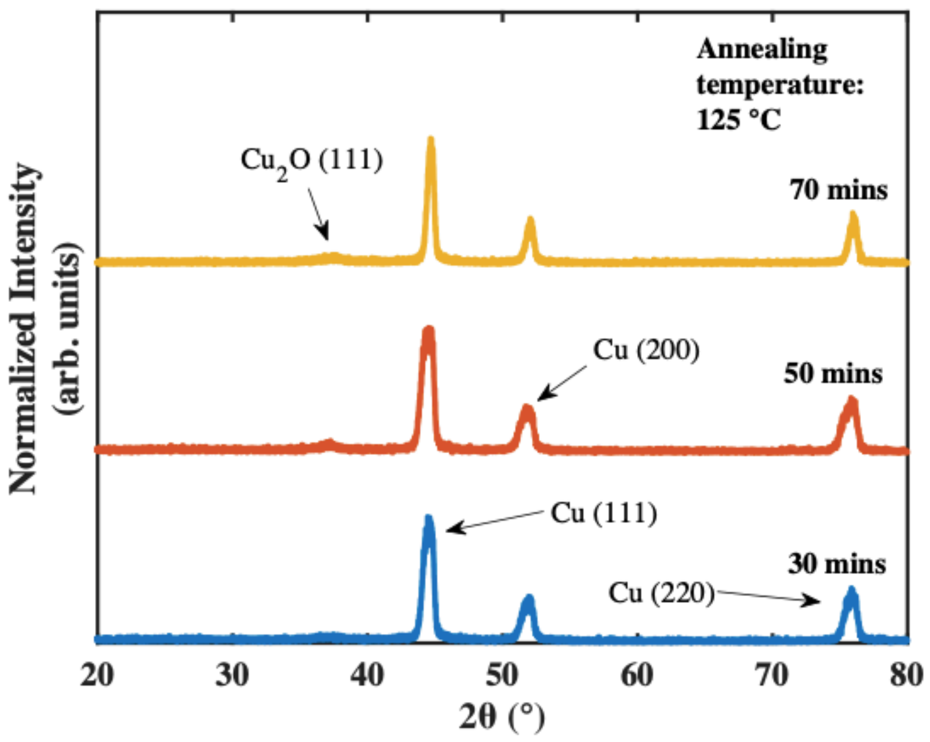

Figure 4.5: XRD patterns of Cu annealed at 125 °C.

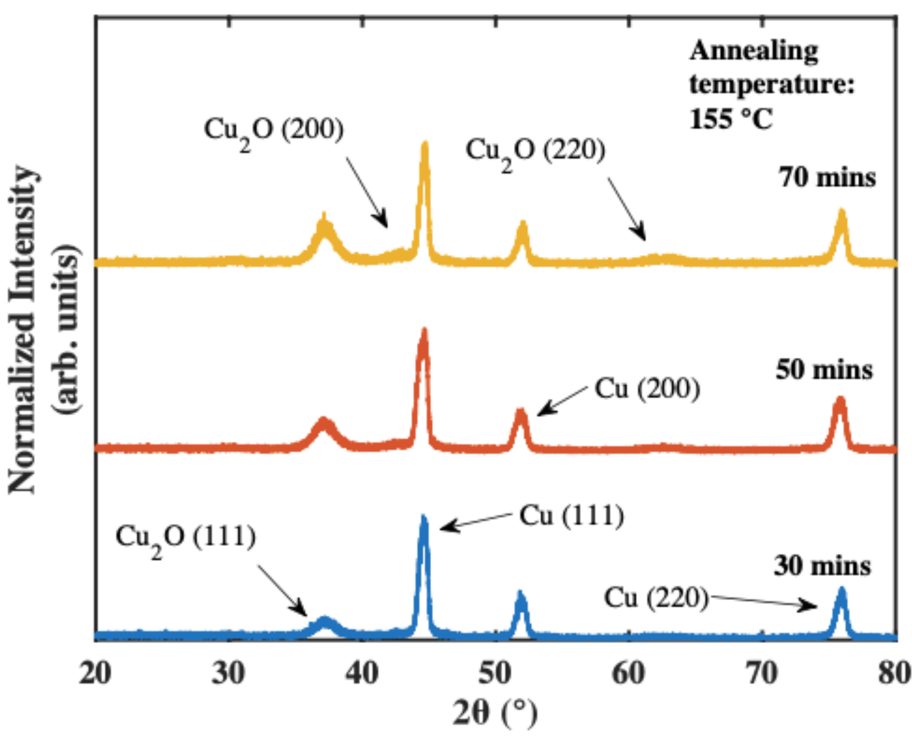

Figure 4.6: XRD patterns of Cu annealed at 155 °C.

4.2.2 XPS

Samples with different top Cu layer thicknesses (20 nm, 23 nm, 26.7 nm) shown in Figure 4.7 were investigated using x-ray photoelectron spectroscopy (XPS) to verify the oxidation state of copper. Cu and WO_3 layers were e-beam evaporated using Lesker PVD 75 and Si_3N_4 was deposited using LPCVD on a Si wafer. The XPS instrument was VG 220i-XL and the incident beam was monochromated Al Kα (E= 1.487 keV). The XPS x-ray source was run at 63 W. The depth profile of the samples was achieved by using Ar^+ sputtering gun with the sputter gun beam energy of 3 keV. The angle of incidence was near 60 degrees. The beam raster was a 2x2 mm^2 area. The annealing times were 20, 40 and 60 minutes while the annealing temperatures were 125 °C, 140 °C and 155 °C which totaled to 9 annealed samples and a control sample.

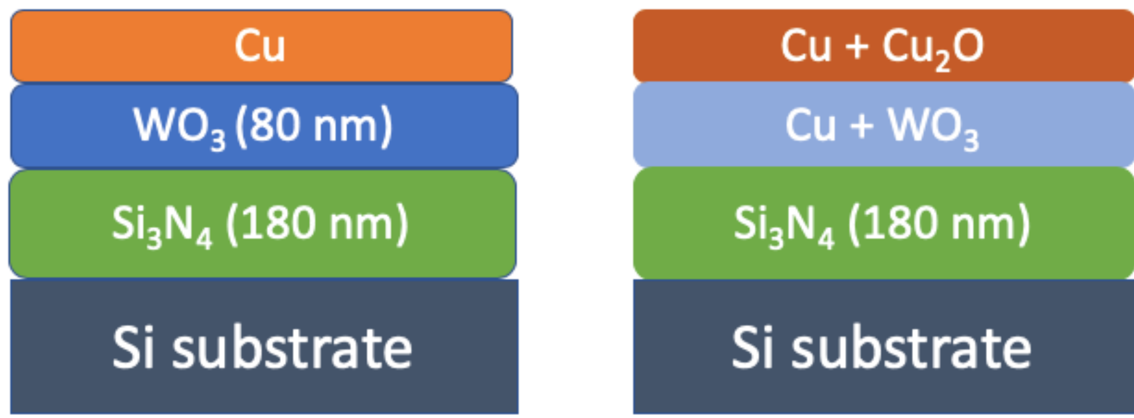

Figure 4.7: Control sample (left) and the samples after annealing (right).

The XPS experiments were carried out as wide scans and Cu 2p scans. The experiment was continued, and the sample was sputtered multiple times until a strong enough N 1s (nitrogen) signal was observed. This was the chosen indicator that Si_3N_4 was reached within the crater instead of the Si signal as Si 2p signal has a very high escape depth with binding energy around 100 eV. On the surface, C peak was detected (data not

shown) and the Cu signal showed existence of CuO for various temperatures with broadening (around 932eV) and a satellite peak (around 943 eV). After a single sputter, the CuO behavior of the Cu signal disappeared and a very weak satellite was observed (around 945 eV) which indicated the presence of Cu_2O. After the second sputter, the same Cu_2O behavior is observed for all conditions. It is noted in [208] that the samples that were exposed to air for a few hours before XPS analysis may absorb carbon and change the Cu_2O into CuO. Also, since the XRD data did not indicate the presence of CuO, it was believed that CuO did not exist in our samples. After multiple sputtering and analysis, the Cu-WO_3/Si_3N_4 interface was reached where Cu was found to be in a metallic state.

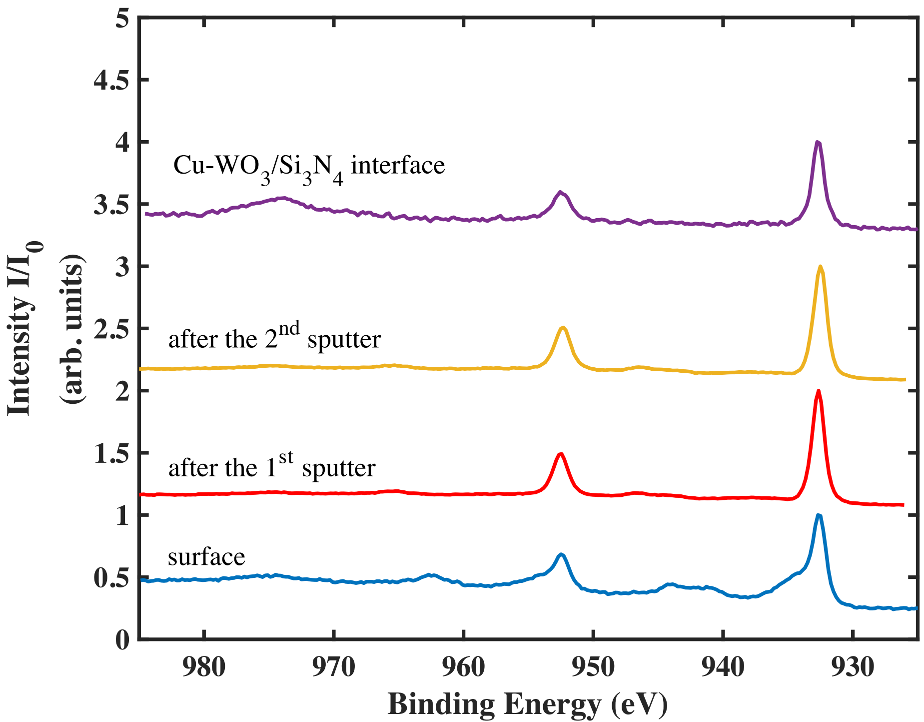

Figure 4.8: Cu 2p XPS spectra of the sample shown in Figure 4.7 annealed at 125 °C.

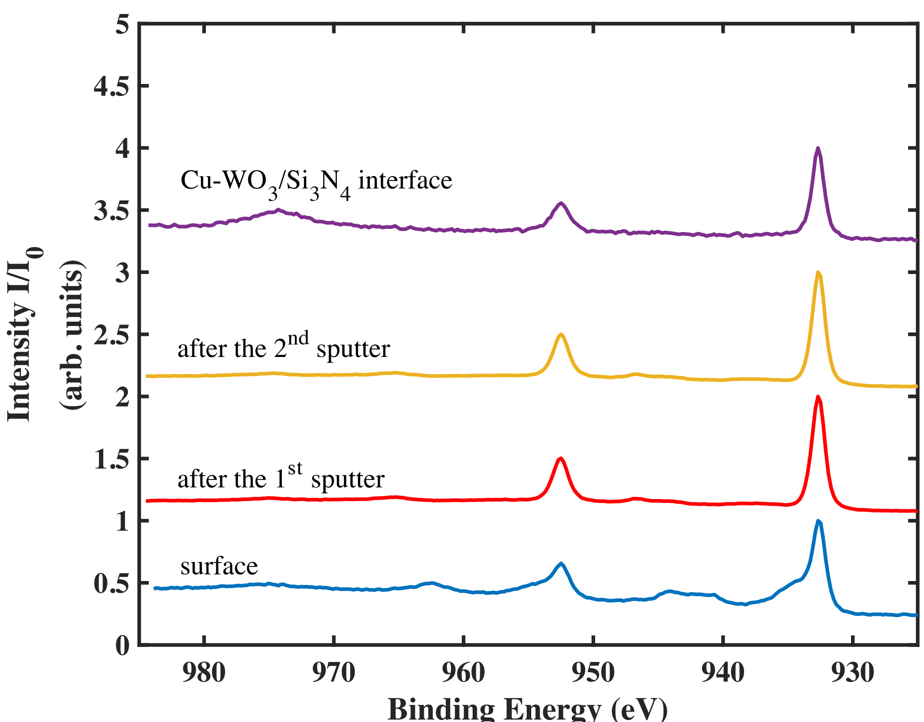

Figure 4.9: Cu 2p XPS spectra of the sample shown in Figure 4.7 annealed at 140 °C.

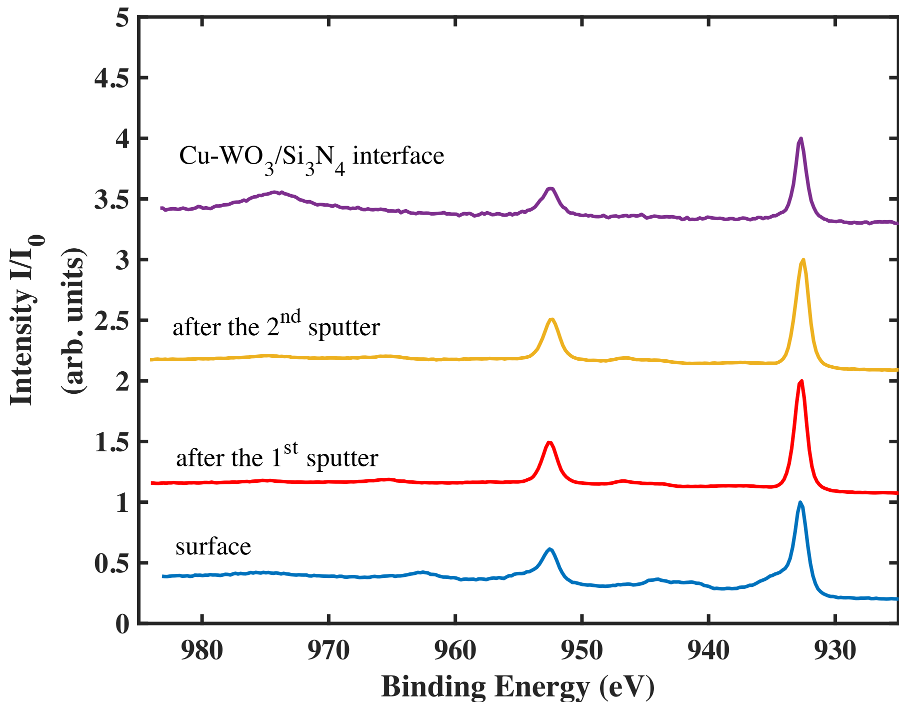

Figure 4.10: Cu 2p XPS spectra of the sample shown in Figure 4.7 annealed at 155 °C.

4.2.3 AFM

In order to study the microstructures on the surface of the Cu_2O, AFM was utilized in tapping mode. The control sample was annealed at different annealing temperatures (125 °C, 140 °C, 155 °C and 170 °C) for different times (30,50, and 70 minutes). The AFM tool was Bruker Multimode while the probe tip used was a silicon etched tip. The raster-scan area was 1 μm x 1 μm. The Cu_2O samples showed an increase in the RMS roughness values with increased annealing temperatures up to 155 °C and then a decrease at 170 °C. The samples annealed for 70 minutes for 125 °C, 140 °C, 155 °C and 170 °C resulted in RMS roughness of 4.8 nm, 8.5 nm, 12.4 nm, and 8.7 nm respectively. The samples annealed at 155 °C for 30, 50 and 70 minutes resulted in RMS roughness of 8.2 nm, 9.4 nm and 12.4 nm respectively. The AFM images are shown in Figures 4.11-12.

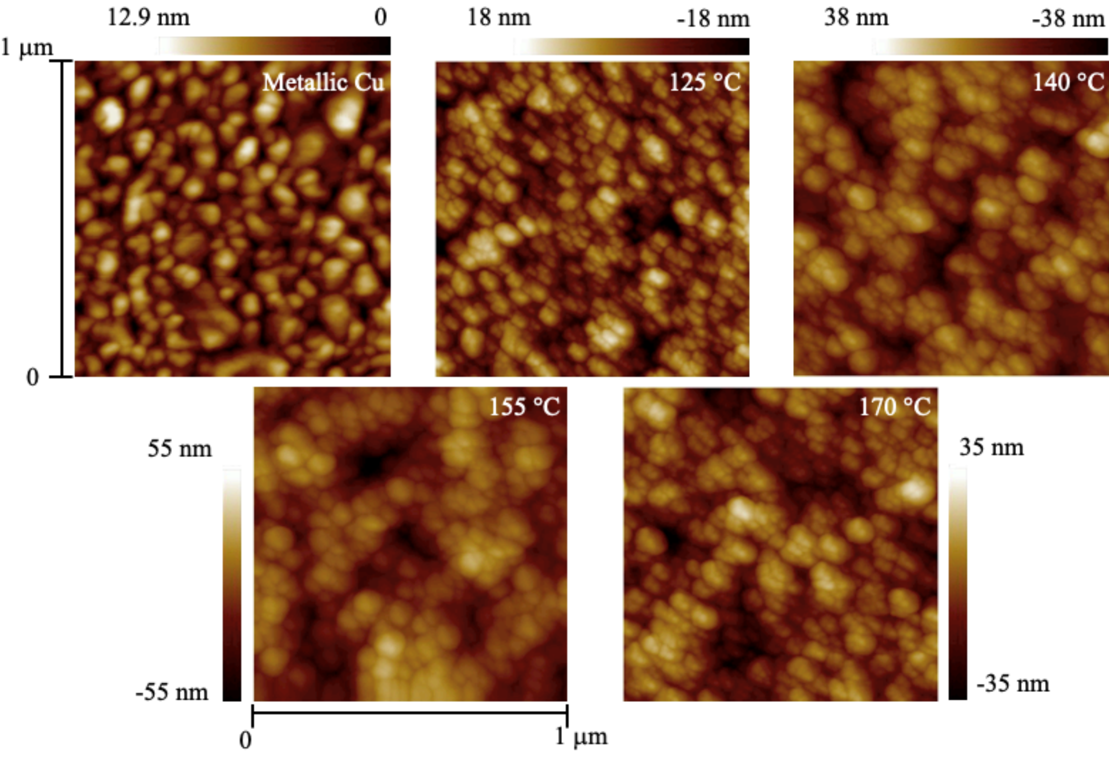

Figure 4.11: AFM images of the oxidation samples. Control sample (metallic Cu) and Cu_2O samples annealed for 70 minutes for various temperatures.

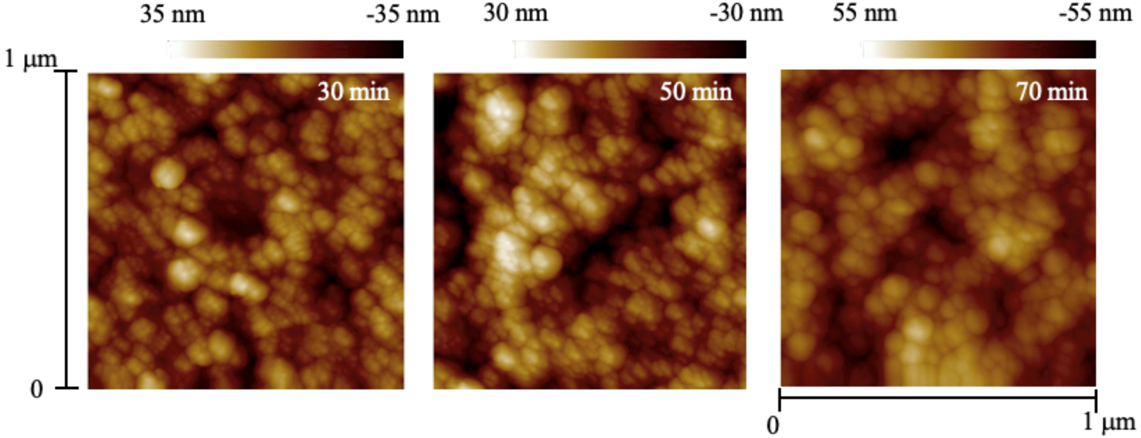

Figure 4.12: AFM images of the oxidation samples at 155 °C. Cu_2O samples annealed for (a) 30 minutes, (b) 50 minutes and (c) 70 minutes.

AFM images revealed that the surface of the film resembled a cauliflower-like morphology which was also revealed by others [175], [209], [210]. AFM images of the oxidation samples were analyzed using Fiji which is a distribution of ImageJ [211]. Particle size calculation was accomplished using the 'Analyze Particles' feature in an ImageJ script (see Appendix A). First, the image was passed through 'Convolve' that does a spatial convolution using a kernel. Then, the contrast of the image was enhanced with 0.3% saturation. The image was then converted to an 8-bit image which was passed through the 'Smooth' feature. Then the 8-bit image was run through the 'Auto Local Threshold' algorithm with the mean method. Furthermore, the image was cleaned out using a few median filters that reduces noise. Because the used filters and the thresholding algorithm creates artifacts, a minimum size of 500 nm^2 was selected for particle analysis. Also, the edges were excluded to further improve the analysis. This algorithm results in ImageJ calculating the areas (A) of the particles. Figure 4.13 shows the example of image pre- and post-processing.

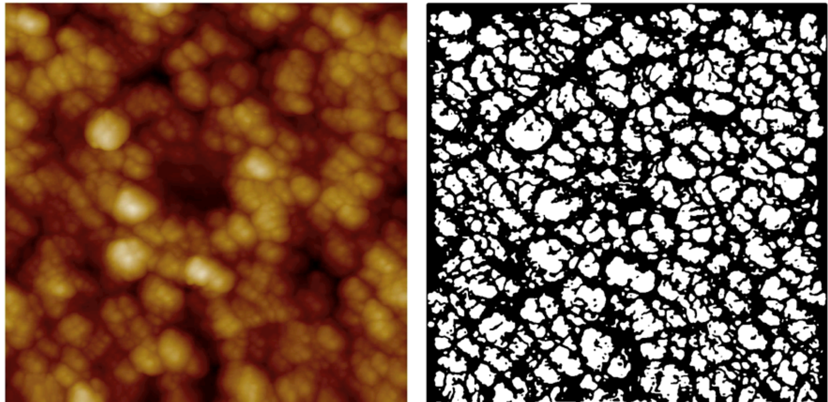

Figure 4.13: Image of the Cu_2O sample pre- and post-processing. Annealed at 155 °C for 30 minutes (left) pre-processing, (right) post-processing

Then, assuming circularity, the size of the particles (D_p) were calculated using $D_p^2 = 4A/\pi$. Table 4.4 shows the summary of the average particle sizes for various annealing times and temperatures. Particle sizes varied between 25 nm and 112 nm showing log-normal distribution which suggests coalescence growth rather than Ostwald ripening [212]. Particle size histograms (bin = 10) of samples annealed for 70 minutes at 125 °C, 140 °C, 155 °C and 170 °C and of samples annealed at 155 °C for 30, 50 and 70 minutes are shown in Figure 4.14 and Figure 4.15 respectively.

Table 4.4: Summary of the Average Particle Sizes Calculated with ImageJ.

Annealing Temperature (°C)	Annealing Time (minutes)	Particle size (nm)
125	70	40.29
140	30	42.93
	50	48.34
	70	51.98
155	30	47.79
	50	48.28
	70	54.09
170	30	58.20
	50	58.50
	70	59.22

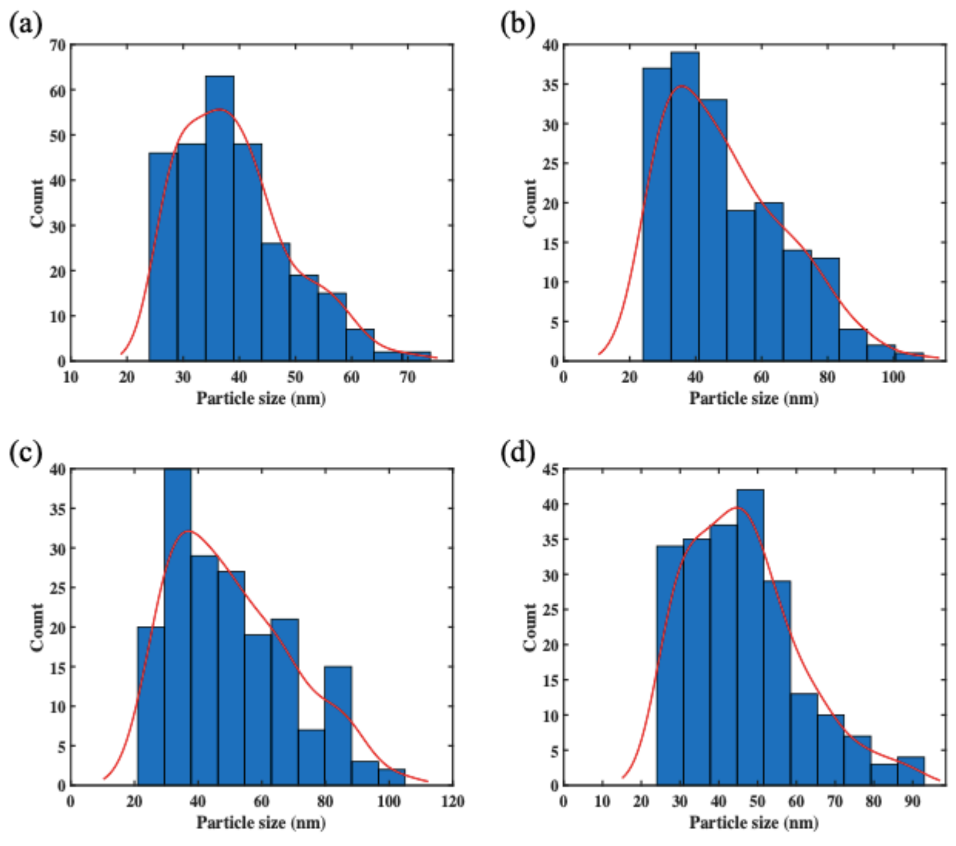

Figure 4.14: Particle size histograms of samples annealed for 70 minutes. At (a) 125 °C, (b) 140 °C, (c) 155 °C and (d) 170 °C (bin = 10).

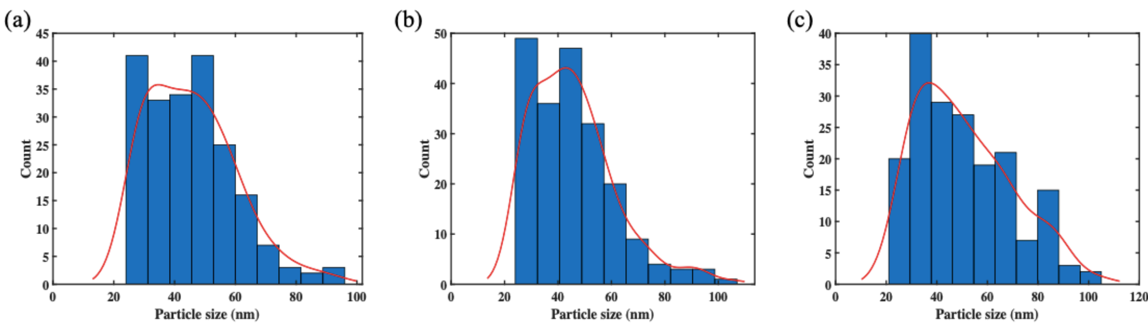

Figure 4.15: Particle size histograms of samples annealed at 155 °C. (a) 30 minutes, (b) 50 minutes, (c) 70 minutes (bin = 10).

4.2.4 Spectroscopic Ellipsometry

The thickness of the Cu_2O films were measured using spectroscopic ellipsometry (SE). Control samples, shown in Figure 4.2, were annealed on a hot plate in air at 140 °C, 155 °C and 170 °C for 30-90 minutes. Samples annealed at 125 °C did not result in a thick enough Cu_2O for SE to be detected; therefore, the measurements are not taken into account. The SE instrument was J.A. Woolam M2000 that operated at Ψ= 60, 70 and 80 degrees while the wavelength range was 193 nm – 1698 nm. The thickness measurement results are shown in Figure 4.16. In this temperature range, copper oxidizes according to the parabolic law $d_{ox}= k_p(T)\ t^{1/2}$, where $k_p(T)= k_0 \exp(-E_a/RT)$ [180], [213]. d^2_{ox} vs. annealing time is shown in Figure 4.17 and the fit is in good agreement with the parabolic law.

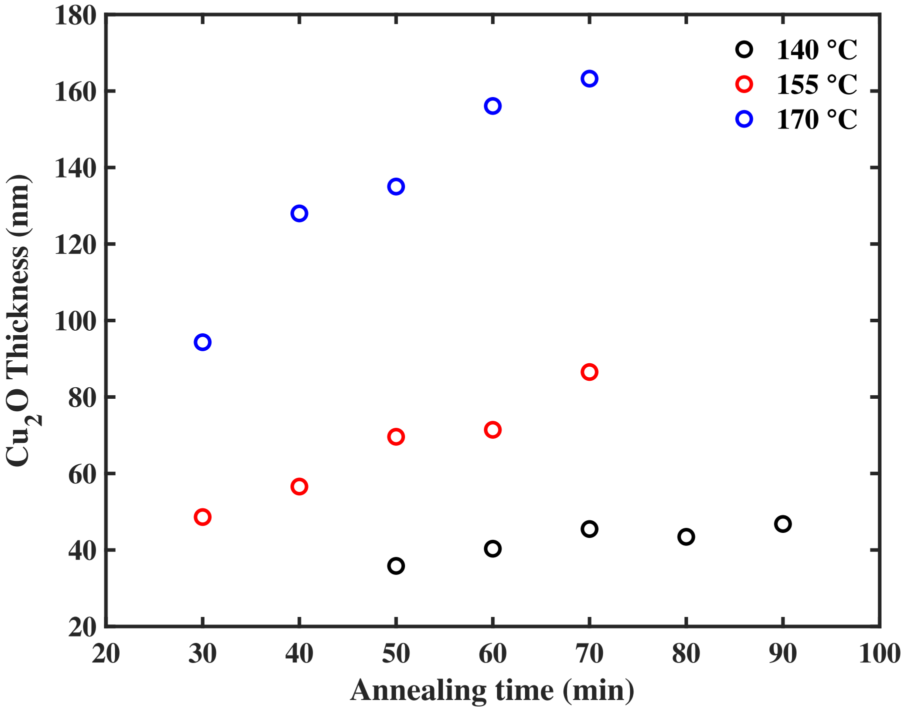

Figure 4.16: Cu_2O thickness (d_{ox}) vs. annealing time.

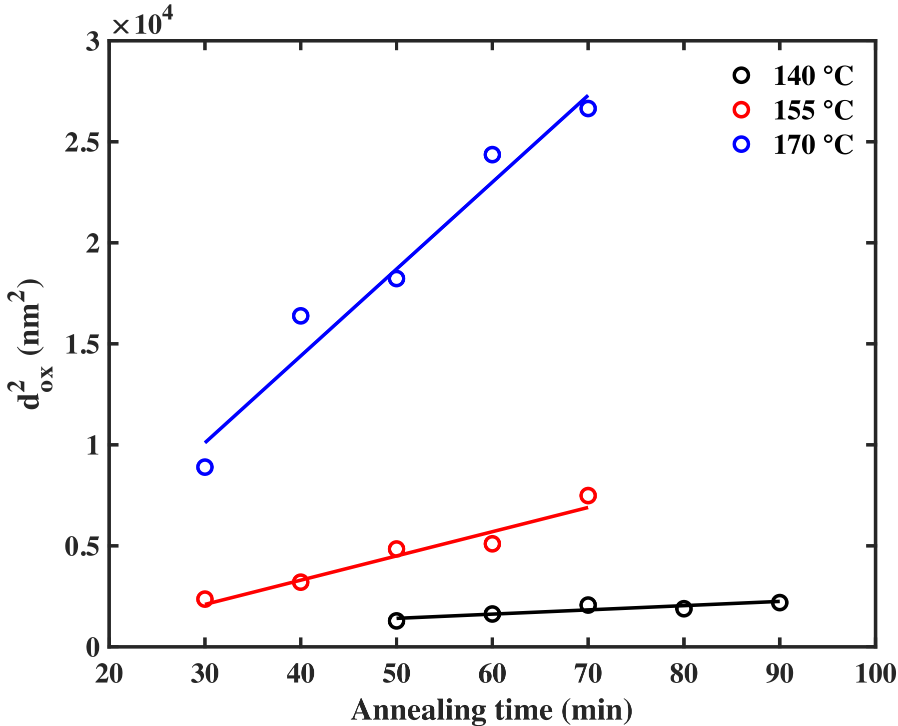

Figure 4.17: d^2_{ox} vs. annealing time.

In order to extract the activation energy for diffusion of copper (E_a) and the constant (k_0), Arrhenius plot of ln (k_p) vs 1/T is plotted (Figure 4.18) where the slope equals to $-E_a/R$ where R is the gas constant ($8.617.10^{-5}$ eV/K). The activation energy for diffusion of copper calculated from the linear fit to the measurement is 0.70 eV (where k_0= 20.7 $cm.s^{-1/2}$).

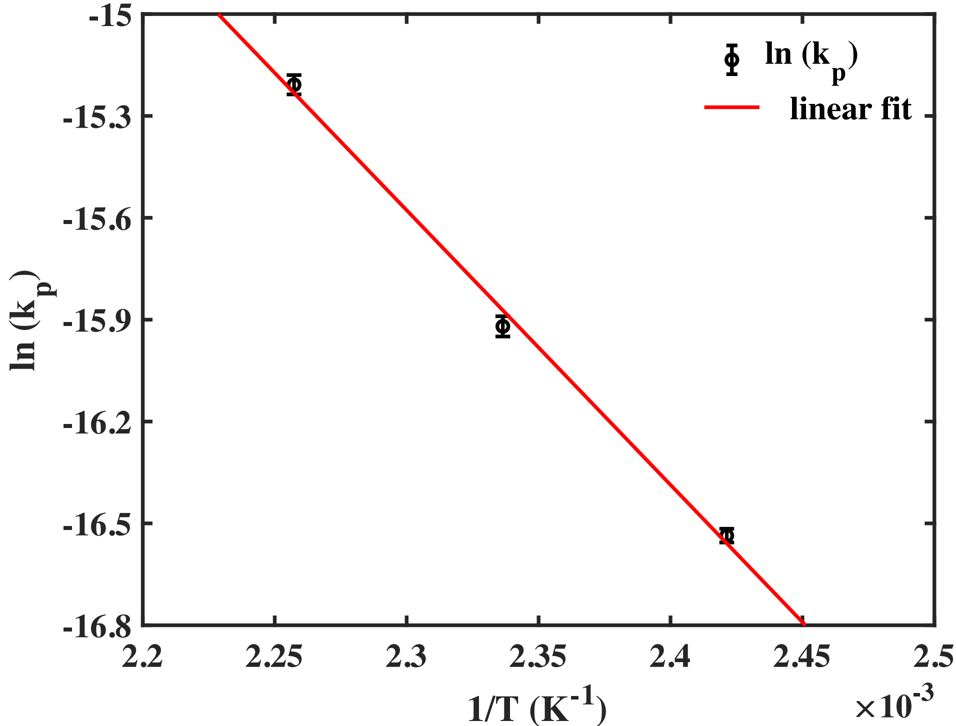

Figure 4.18: Arrhenius plot of ln (k_p) vs 1/T. The red line is a linear fit to the measurement.

When Cu oxidizes and forms a layer of oxide, Cu^+ ions have to be transported from the Cu layer to the oxide/air interface for further oxidation [214]. Obtained E_a (0.70 eV) indicates that the diffusion mechanism is not the vacancy mechanism which is most commonly seen in single crystal materials. In the vacancy mechanism, E_a should approximate the bond energy of the Cu ion, ~ 2 eV [180]. Due to the large difference between these values, it is reasonable to assume that the diffusion mechanism is mostly defect-related grain boundary diffusion. The obtained E_a is somewhat higher than reported values of Zhong et. al. [180] (0.57 eV) and Ramanandan et. al. [181] (0.55 eV), comparable to the reported value of O'Reilly et. al. [186] (0.74 eV) and smaller than the value reported by Fujita et. al. [176] (1.03 eV).

CHAPTER 5

DIFFUSION OF COPPER

5.1 Brief History of Integration of Copper and Diffusion Kinetics

Aluminum was being used in the IC fabrication as the metal lines/interconnects until 1990s, however, with increase in demand in performance and in order to reduce the RC delay time, Cu was introduced to replace aluminum due to its low resistivity (~1.7 μΩ-cm for bulk) and good electromigration resistance [134]. After the change, the industry faced some problems. It was quickly realized that some of these problems were fast drift of Cu in SiO_2 [215] and fast diffusion in Si [216], drifting through intermetal dielectrics (IMD) and forming Cu-Si compounds [217]. Moreover, it was found out that the migration was faster under electric field because Cu migrates in the positively charged (Cu^+) state [215]. In addition to these problems, increasing cross-talk between the interconnects, degradation and potential failure of the IMD directed the research in the semiconductor field towards limiting the diffusion of Cu into SiO_2 and Si. In order to limit/prevent the diffusion of Cu, various diffusion barriers were investigated such as Ta [218], TaN [219], [220], TiN [221], Ta_2O_5[222], W and WN_x [223], $MnSi_xO_y$ [224], [225], alloys that are self-forming barriers (Al [226]–[228], Zr [229]) and additional capping layers such as HfO_2 [230]. Since the 1990s, diffusion of copper in dielectrics has been researched extensively which makes Cu/oxide-electrolyte (Cu-SiO_x or Cu-WO_3) PMC devices easier to integrate as these materials are foundry-ready and well-studied. PMC devices in our lab utilize silica (SiO_x) and WO_3 as the switching/electrolyte layer. Diffusion of Cu in WO_3 has not been well studied but diffusion of Cu in SiO_2 and silica has been reported by many researchers

[215], [231]–[238]. In order to study the diffusion kinetics, the researchers often utilize the equilibrium capacitance-voltage (C-V) measurements. The equilibrium C-V measurements done at room temperature enables researchers to detect the mobile ions in the dielectric films [128], [239]. As bias-temperature stress (BTS) is applied to the metal-insulator-silicon (MIS) capacitor, the drifting ion, Cu^+ in this case, moves towards the silicon through the insulator, SiO_x. The flatband voltage shifts to negative values according to equations (5.1) and (5.2).

$$V_{FB} = -\int_0^{t_{ox}} \frac{\rho(x)xdx}{\varepsilon_0\varepsilon_{ox}} \tag{5.1}$$

where t_{ox} is the oxide thickness, $\rho(x)$ is the charge density of Q_{ox} (oxide charge) as a function of the distance x from the metal/dielectric interface, ε_0 is the permittivity of free space (8.854 x 10^{-12} F/m) and ε_{ox} is the relative dielectric constant of the oxide. Assuming all the mobile ions reside at the oxide/silicon interface, mobile ion concentration (N_m) can be found using equation (5.2) by measuring the flatband voltage shifts (ΔV_{FB}).

$$N_m = -\frac{C_{ox}\Delta V_{FB}}{qA} \tag{5.2}$$

where C_{ox} is the oxide capacitance, q is the electron charge and A is the area of the capacitance. Because the penetration of Cu^+ ions into the dielectric is thermally activated, by varying the temperature and using the Arrhenius dependence on the temperature (T), the activation energy (E_a) can be found using equation (5.3).

$$N_m(T) = N_0 \exp(-\frac{E_a}{k_B T}) \tag{5.3}$$

where N_0 is a constant and k_B is the Boltzmann's constant. This analysis technique relies on the assumption of single activation energy. Also, a great care to prevent the effect of the

mobile alkali ions such as Na^+ must be taken (sodium ions are the most dominant contaminant [128]). This is usually done by imposing a reverse bias on the capacitor for a short period of time. These mobile alkali ions are highly mobile compared to Cu^+, therefore by imposing a reverse bias for about 5 minutes, the effect can be eliminated [231]. The summary of the reported activation energy (E_a) of diffusion of Cu in SiO_x by BTS measurements is given in Table 5.1.

Table 5.1: Summary of the Reported E_a of Diffusion of Cu in SiO_x and Silica by BTS.

Dielectric	Deposition	Temperature Range (°C) & Bias Stress	Activation Energy (eV)	Study
SiO_2	Thermally grown	350 – 450 @ 1MV/cm	1.82	[215]
Silica	SOD	300 – 500 @ N/A	0.71	[231]
Silica	PECVD	300 – 500 @ N/A	0.84	[231]
SiO_2	Thermally grown	300 – 500 @ N/A	1.02	[231]
SiO_2	Thermally grown	100 – 200 @ 4MV/cm	1.20	[233]
SiO_2	Thermally grown	200 – 275 @ 1MV/cm	1.54	[234]
Methyl-doped SiO_2	CVD	175 – 275 @ 1.5MV/cm	0.76	[236]
SiO_2	PECVD	125 – 300 @ 1MV/cm	1.13	[237]
SiO_2	Thermally grown	250 – 300 @ 1MV/cm	0.93	[238]

SOD: spin-on deposition
PECVD: plasma enhanced chemical vapor deposition
N/A: No bias stress

As it can be seen from Table 5.1, the reported values of activation energy of copper diffusion in SiO_x vary. It is expected that the reported values for E_a with bias stress (field-assisted) compared to no-bias stress would be lower due to barrier height lowering. Some of the major factors that play a role in the difference between the values are the

deposition/growth techniques/conditions, BTS values and range, the structure and composition, and the density of the oxide layer.

Another method to characterize the diffusion kinetics of Cu into oxides is to utilize surface characterization tools equipped with sputtering guns such as XPS, AES or SIMS on samples annealed at different temperatures and modeling the diffusion by Fick's second law, equation (5.4).

$$\frac{\partial C(x,t)}{\partial t} = \mathrm{D}\frac{\partial^2 C(x,t)}{\partial x^2} \tag{5.4}$$

where C(x,t) is the concentration, t is the annealing time, D is the diffusion coefficient and x is the distance. Fick's second law has two solutions, where one solution, equation (5.5), is derived for "thick" films (constant source), and the other solution, equation (5.6), is derived for "thin" films (limited source).

$$C(x) = C_s\,[1 - \mathrm{erf}(-\frac{x}{\sqrt{4Dt}})] \tag{5.5}$$

where C_s is the surface concentration of atoms and erf is the mathematical function called the error function.

$$C(x) = C_0 \exp(-\frac{x^2}{4Dt}) \tag{5.6}$$

where C_0 is the initial concentration of atoms at x=0. Because diffusion is thermally activated, the diffusion coefficient is expressed by an Arrhenius dependence,

$$D = D_0 \exp(-\frac{E_a}{k_B T}) \tag{5.7}$$

where D_0 is the diffusion constant. In order to find out the diffusion kinetics, annealing temperature must be varied, and different diffusion coefficient values must be extracted according to the correct Fick's law solution. Then, plotting ln(D) vs $1/k_BT$ for different

annealing temperatures will result in a graph with the slope of $-E_a$ and the $1/k_BT=0$ intercept will be $\ln(D_0)$.

5.2 Diffusion of Cu in WO_3

Cu-doped WO_3 (Cu-WO_3) system is of particular interest in electronics due to its many potential applications. One application of Cu-WO_3 is that it is a switching medium that has been used in PMCs and has been investigated as a promising BEOL-compatible material for CBRAM applications [53], [75], [76], [240]. Cu-WO_3 system has also been studied for uses in photonic devices [241], cancer therapy applications [242], and semiconducting gas sensors [243]. Early interest in WO_3 in electronics was generated by its electro- and photo-chromic effects [244] where electrochromism of amorphous WO_3 can be explained by the double-charge injection model [245]. Injection of M^+ and electrons into a WO_3 host matrix forms M_xWO_3, where $0 < x < 1$. M^+ is usually H^+, Li^+ or Na^+ [246], however it can be any mobile ion such as Cu^{z+} [76], [78]. This effect is crucial for the PMCs as it implies that the conductivity of the material can be modulated.

5.2.1 XPS

Diffusion of Cu in WO_3 was investigated using XPS depth profiling. 23 nm of Cu was e-beam evaporated on top of 80 nm of WO_3 (also e-beam evaporated) in Lesker PVD 75 which was deposited on top of Si_3N_4/Si wafer where the Si_3N_4 was deposited using LPCVD. These samples were annealed in in air at 1 atm. The annealing temperatures and times were 125 °C, 140 °C and 155 °C for 60 minutes, 40 minutes and 20 minutes respectively. These samples are referred to as XPS Sample #1, XPS Sample #2 and XPS

Sample #3 respectively. The samples before and after annealing are shown in Figure 5.1. Even though there were other samples as mentioned in the "4.2.2 XPS" of Chapter 4, they were not analyzed in the diffusion study because there was remaining metallic Cu for at least one condition for each deposited Cu thickness. The XPS instrument was VG 220i-XL and the incident beam was monochromated Al Kα (E= 1.487 keV). The XPS x-ray source was run at 63 W. The depth profile of the samples was achieved by using Ar^+ sputtering gun with the sputter gun beam energy of 3 keV. The angle of incidence was near 60 degrees. The beam raster was a 2×2 mm^2 area.

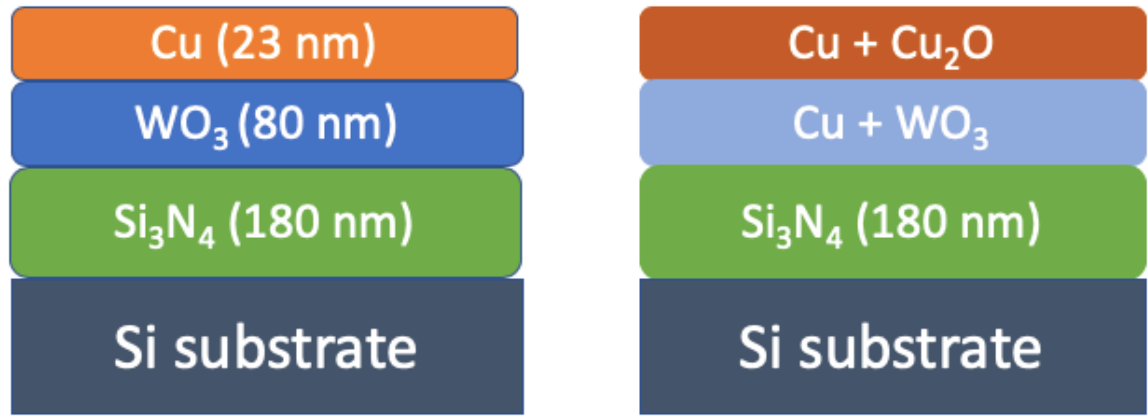

Figure 5.1: Samples before annealing (left) and after annealing (right) for XPS.

The XPS data was analyzed using CasaXPS and the resulting depth profiles of the Cu for each condition are shown in Figure 5.2 while the surface composition was left out due to existing hydrocarbons.

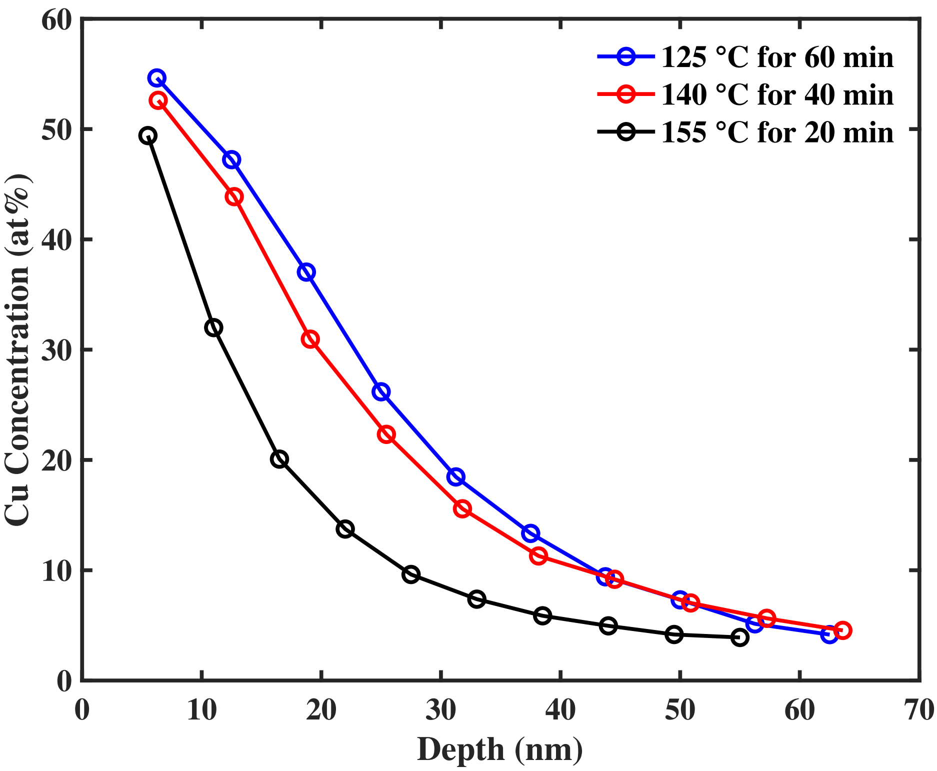

Figure 5.2: Depth profile of Cu (at%).

Since the oxidation kinetics of e-beam evaporated Cu was already characterized (presented in Chapter 4), the thickness of the Cu_2O layer was estimated using a model. After establishing the cuprous oxide thicknesses, only the data coming from the Cu which is diffused in the WO_3 layer ('diffusion data') were analyzed to characterize the diffusion. Diffusion data in comparison to the whole data set are shown in Figures 5.3-5.

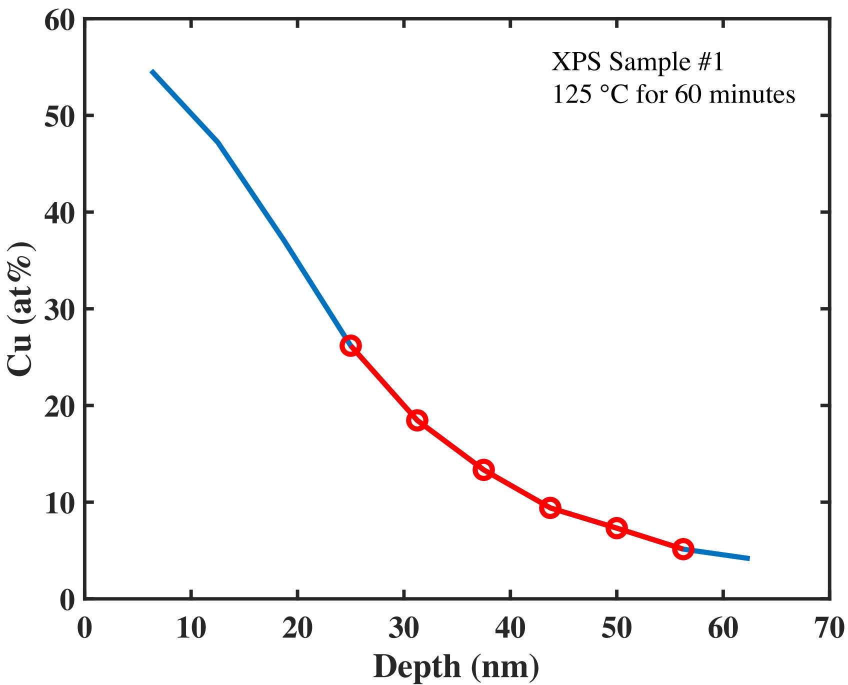

Figure 5.3: Depth profile of Cu (at%) of XPS Sample #1. The red dotted line indicates the 'diffusion data'.

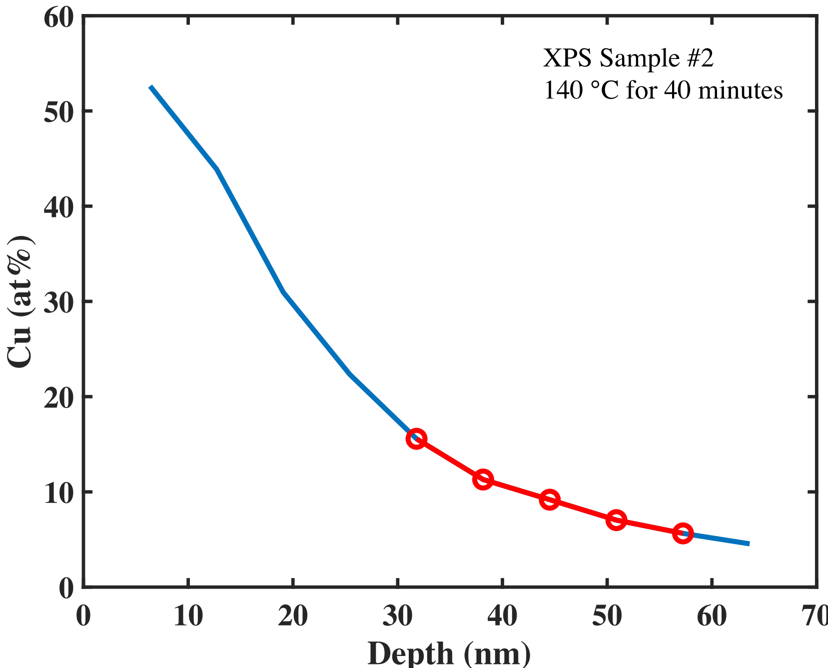

Figure 5.4: Depth profile of Cu (at%) of XPS Sample #2. The red dotted line indicates the 'diffusion data'.

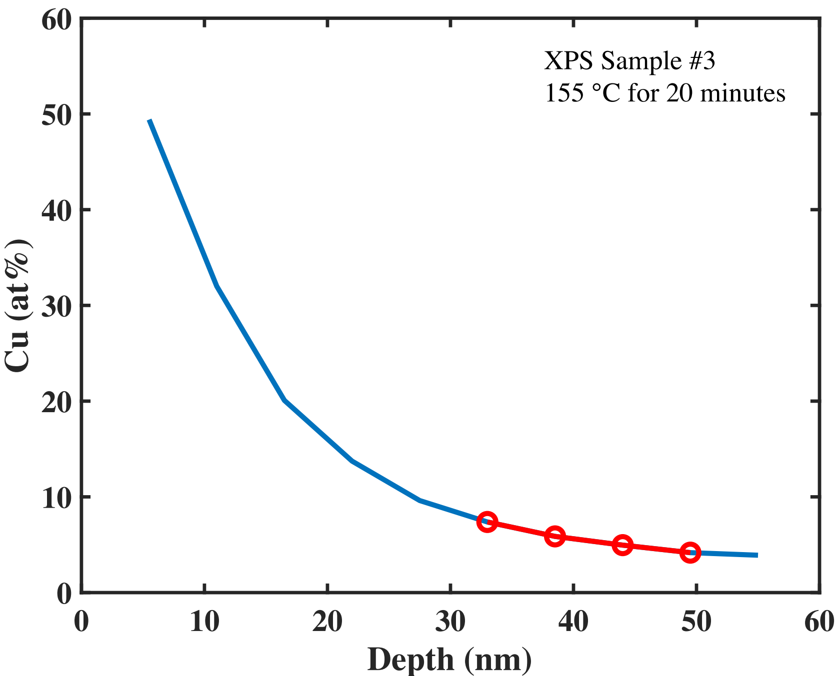

Figure 5.5: Depth profile of Cu (at%) of XPS Sample #3. The red dotted line indicates the 'diffusion data'.

Corresponding diffusion data were then analyzed to extract the diffusion coefficients for each condition. In order to do this, the data were plotted as ln (C) vs x^2 as the slope will be -1/4Dt according to equation (5.6) where D is the diffusion coefficient and t is the annealing time. This process, XPS Sample #1, is shown in Figure 5.6 and the diffusion coefficients for each condition are presented in Table 5.2.

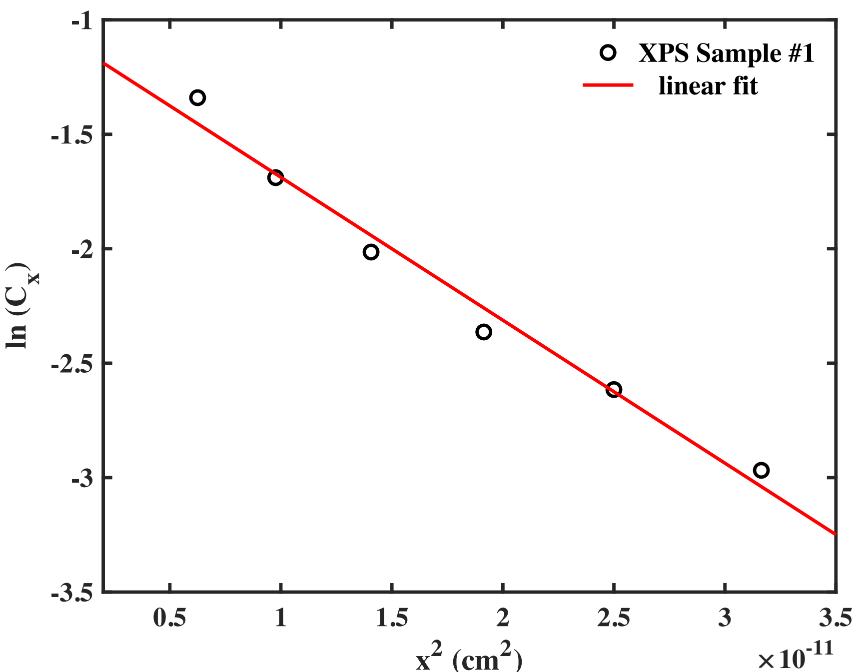

Figure 5.6: Plot of ln (C) vs x^2 for the diffusion data for XPS Sample 1. The red line is the linear fit to the data where the slope is -1/4Dt.

Table 5.2: Diffusion Coefficients for Each XPS Sample (Cu-WO_3)

Sample #	Annealing Temperature (°C)	Annealing Time (minutes)	Diffusion coefficient (cm^2/s)
Sample 1	125	60	1.1122×10^{-15}
Sample 2	140	40	2.3815×10^{-15}
Sample 3	155	20	5.0702×10^{-15}

Diffusion coefficient equation (5.7) is an Arrhenius equation; therefore, ln (D) vs 1/T will yield a slope of $-E_a/k_b$ where k_b is the Boltzmann constant (8.617×10^{-5} eV/K) and E_a is the activation energy of diffusion of Cu in WO_3 and the 1/T=0 intercept will correspond to $\ln(D_0)$ where D_0 is the diffusion constant. Plot of ln(D) vs 1/T is shown in Figure 5.7 along with a linear fit. Calculated E_a is 0.74 eV, where $D_0 = 2.73\times10^{-6}$ cm^2/s. There was no

reported E_a value of Cu in WO_3 to compare, however this value is lower than the ones reported by Sankaran et. al. for Cu diffusion in amorphous Al_2O_3 (0.90 eV) [247] and by Fisher et. al. for Cu diffusion in thermally grown SiO_2 (1.02 eV), but very similar to the value reported in the same study by Fisher et. al. for Cu diffusion in spin-on-deposited porous silica (0.71 eV) [231].

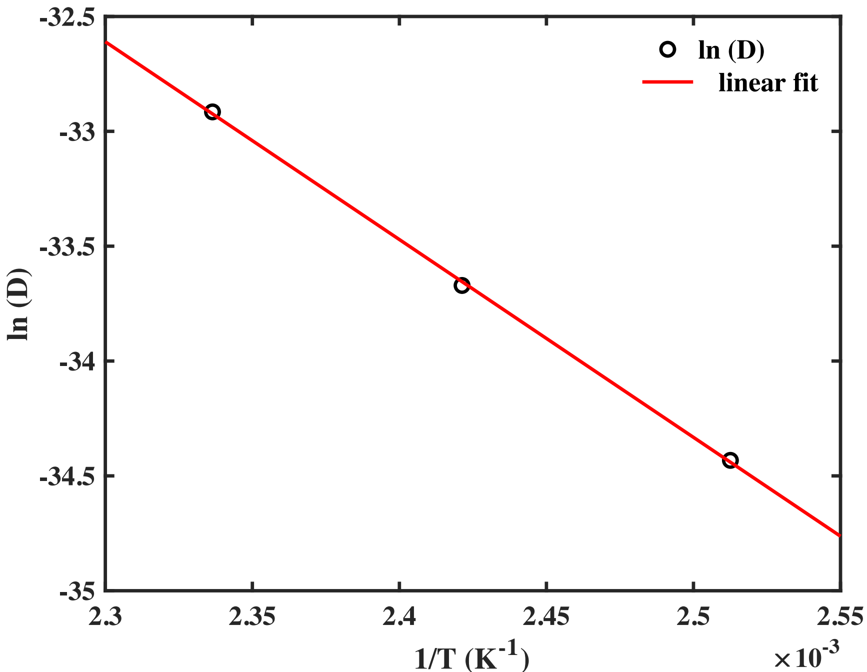

Figure 5.7: Plot of ln (D) vs 1/T. Red line is the linear fit to the data.

5.2.2 SIMS

In order to take a closer look at the interfaces and to investigate how much copper is present in our samples, secondary ion mass spectroscopy (SIMS) was utilized. The samples were Si_3N_4/Si and WO_3/Si_3N_4/Si (shown in Figure 5.8), and the samples with Cu, shown in Figure 5.9, pre- and post-annealing. The annealing was done for 30 minutes at 135 °C in air.

Figure 5.8: Si_3N_4/Si sample on the left and WO_3/Si_3N_4/Si sample on the right.

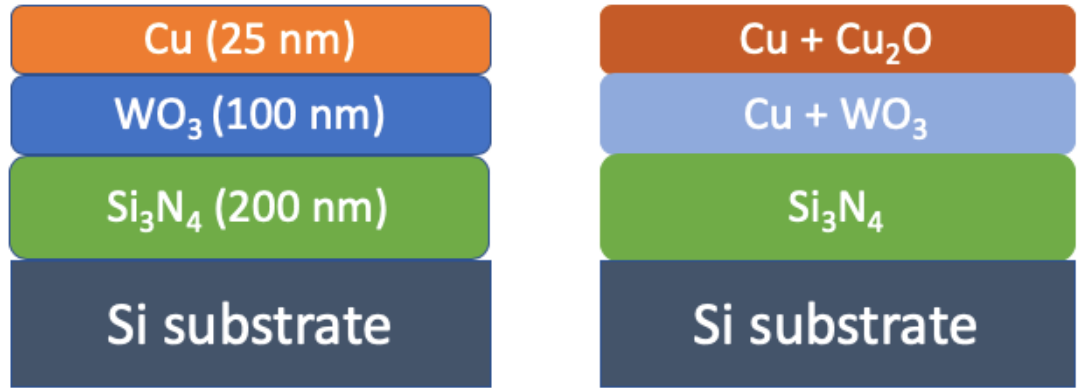

Figure 5.9: Blanket films of Cu/WO_3/Si_3N_4/Si. Control sample (left) and annealed (right).

The SIMS instrument was Cameca IMS 6f. The primary beam was comprised of O_2^+ ions with 7.6 keV energy while ^{28}Si, ^{63}Cu and ^{184}W were being detected. The total raster area of the beam was 250 µm × 250 µm and the secondary ions were sampled from an area of 35 µm × 35 µm. This was done to avoid signals coming from the edge of the crater. Figures 5.10-13 show the SIMS profiles of the samples mentioned above.

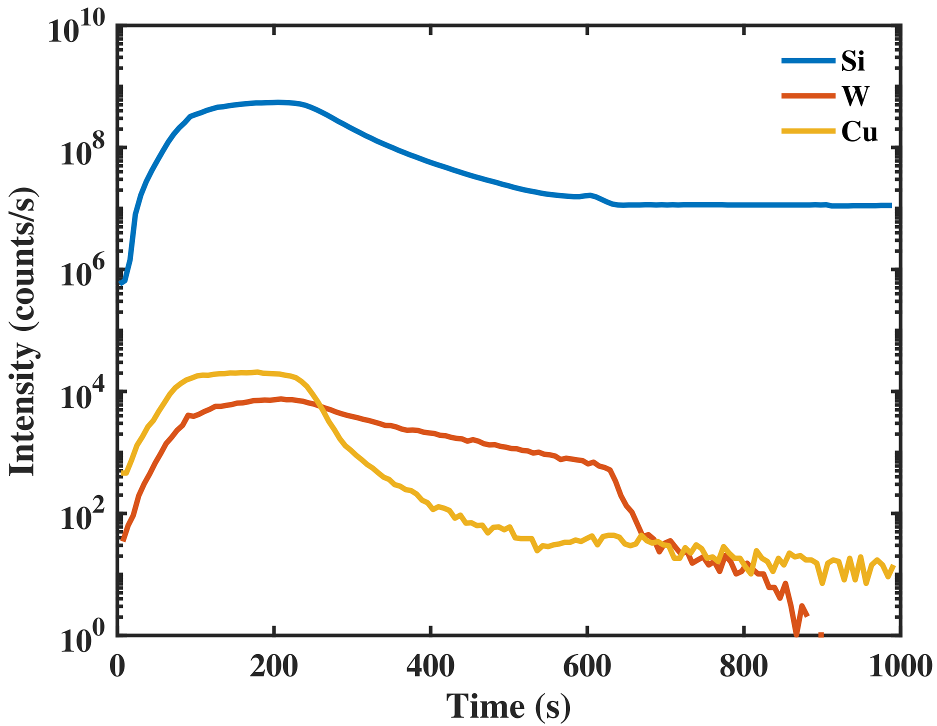

Figure 5.10: SIMS profile of Si_3N_4/Si sample.

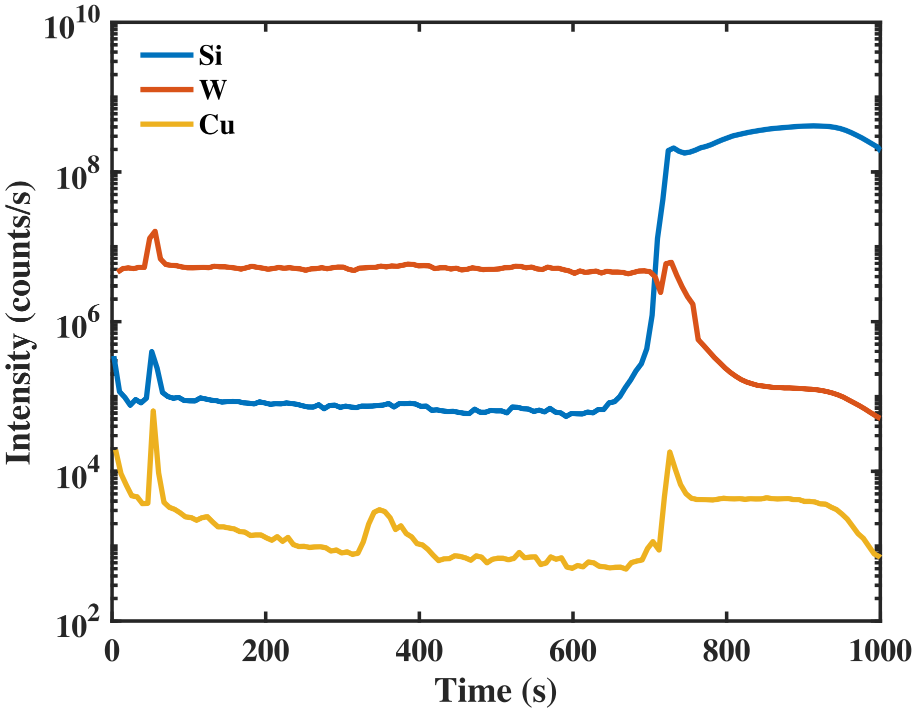

Figure 5.11: SIMS profile of WO_3/Si_3N_4/Si sample.

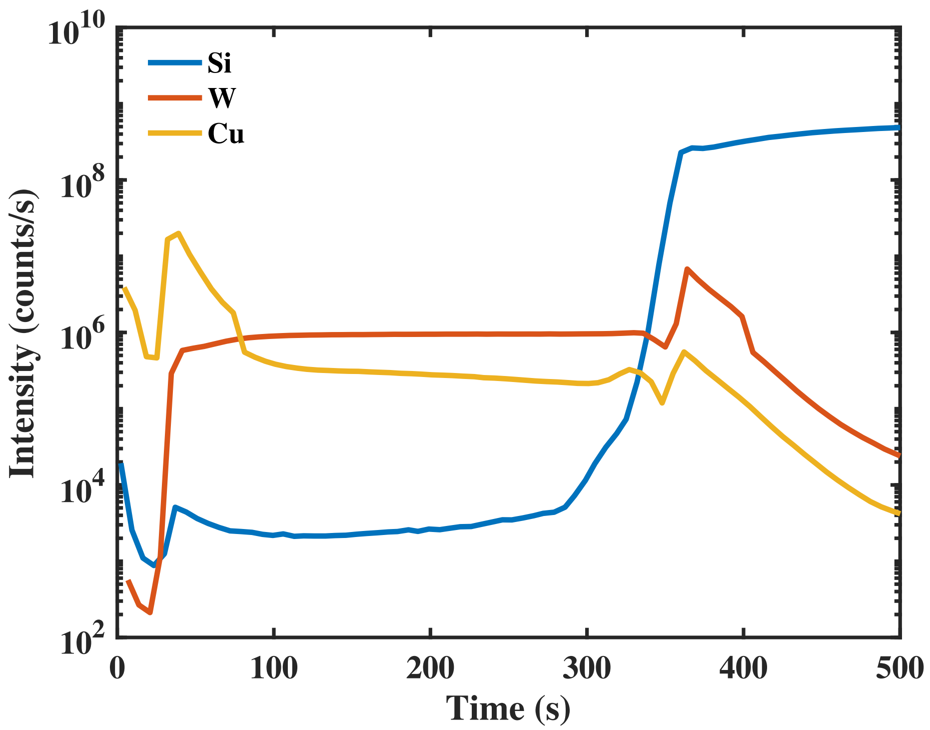

Figure 5.12: SIMS profile of unannealed $Cu/WO_3/Si_3N_4/Si$ sample.

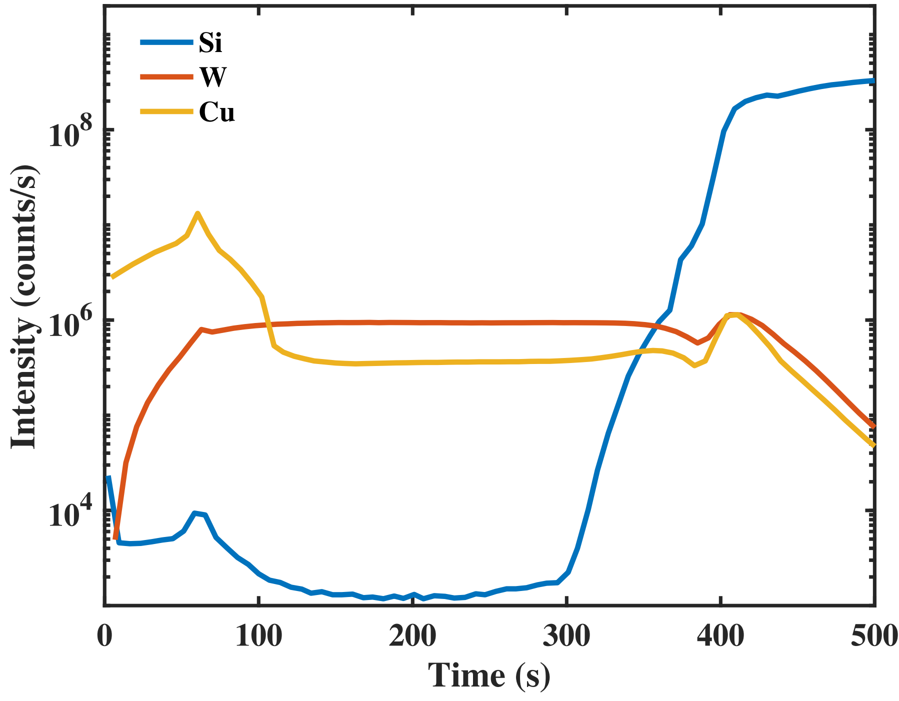

Figure 5.13: SIMS profile of annealed $Cu/WO_3/Si_3N_4/Si$ sample.

SIMS profiles were obtained on all these samples rather than just the last two because a level of baseline for "contamination" wanted to be established. It is clear by looking at Figures 5.10-13, 10^3-10^4 counts/s seems to be that baseline. Furthermore, Figure 5.12 reveals that inter-diffusion of Cu atoms starts even pre-annealing. This is either due to the interaction of matrix atoms and the beam, and/or inter-diffusion during copper film deposition. However, since the deposition technique was low impact e-beam evaporation [90], the former is thought to be the case here. Pre-annealing profile, Figure 5.12, also shows that W intensity signal at the Cu/WO_3 interface is pretty sharp as expected compared to post-annealing profile. It also shows that Cu count follows a complementary error function (erfc) profile due to "constant source" (thick-enough) of metallic Cu being present. It is clear that annealing the sample results (Figure 5.13) in a Gaussian-like distribution of Cu atoms near the interface (t=80 seconds) which suggests that there was no metallic Cu left post-annealing. This was also later confirmed by the Matlab model (Chapter 6). Figure 5.13 also indicates that there is another interface/layer being formed during annealing on the surface. Sudden change of the sign of the slope at around t= 80 seconds is attributed to this layer forming on top of the Cu-WO_3 layer. This is probably due to Cu being oxidized from the top and forming Cu_2O film. It is clearly seen in Figure 5.13 that, Cu count increases as we move away from the surface and at around t= 80 seconds, there is a peak. This behavior can be due to various reasons. One is the impact of the beam causing the matrix atoms to get pushed into the sample, hence causing a false count. Secondly, it can be due to the self-limiting nature of the relatively short low temperature oxidation. All of the copper may not reach to the surface to oxidize hence, the stoichiometry of the Cu_2O film may vary through its thickness.

5.2.3 TEM

In order to have a better understanding of the morphology, layer thicknesses, and diffusion of Cu in WO_3, TEM imaging and EELS were carried out using JEOL ARM200F. Blanket films, shown in Figure 5.14, with different deposited Cu thicknesses were fabricated. Then, these films were annealed at different annealing conditions in air. These different fabrication parameters and annealing conditions are given in Table 5.3.

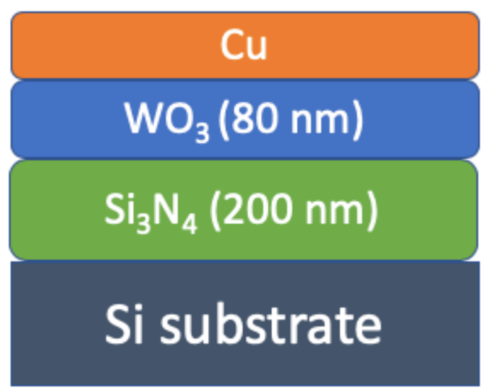

Figure 5.14: Structure of the as-deposited blanket films for TEM analysis.

Table 5.3: Fabrication/Annealing Conditions of the Blanket Films for TEM & XRD

TEM Sample #	Annealing Temperature (^oC)	Annealing Time (minutes)	Deposited Cu thickness (nm)
Sample 1	135	13	10
Sample 2	155	25	20
Sample 3	155	60	30

Cross-section of the TEM Sample 1 and the higher magnification image along with the EELS (copper map) analysis are shown in Figure 5.15 and 5.16 respectively.

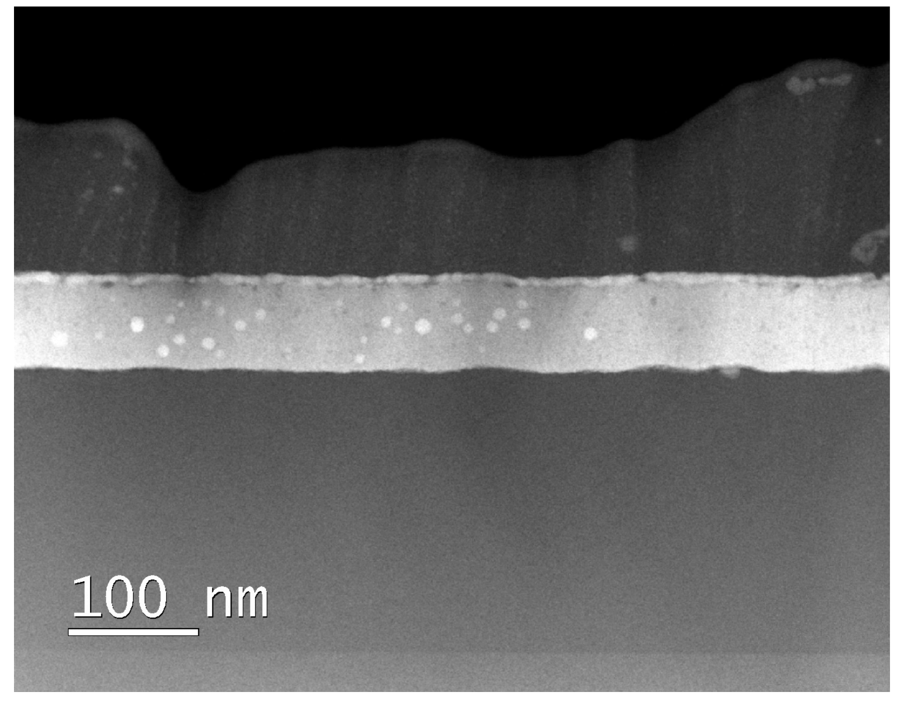

Figure 5.15: Cross-section TEM image of the Sample 1, Cu_2O/Cu-WO_3/Si_3N_4/Si.

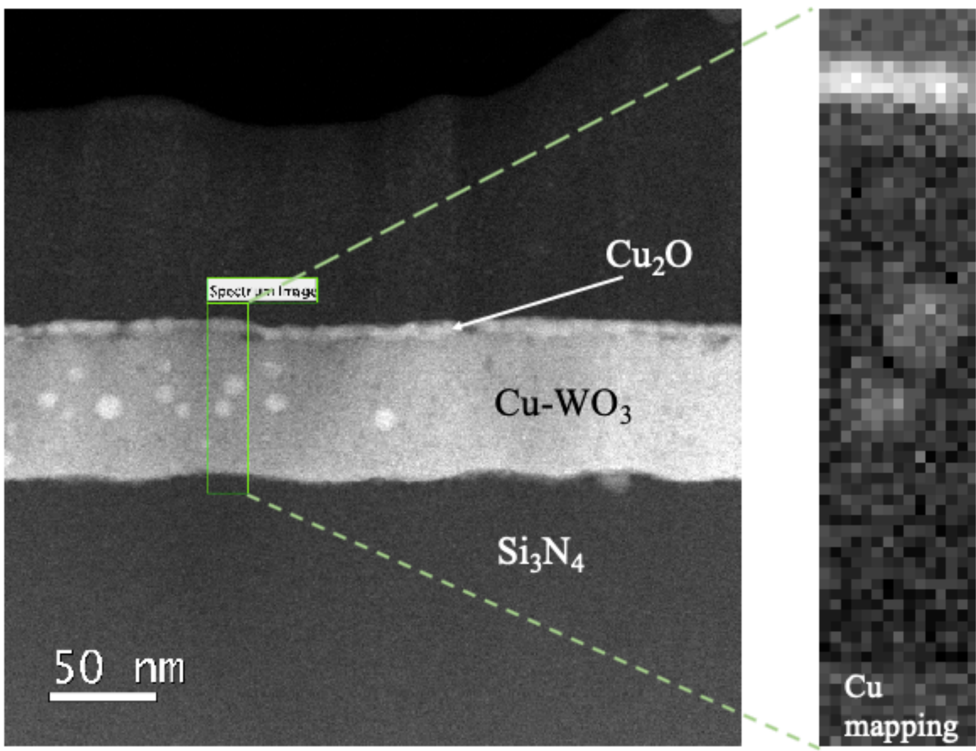

Figure 5.16: TEM image (left), and the EELS (Cu mapping) of the box (right). The dimensions of the EELS map are 19 nm wide x 88 nm tall.

EELS analysis in Figure 5.16 clearly shows that there is a Cu-rich layer on top of the WO_3 which is attributed to the Cu_2O, and the WO_3 layer is doped with Cu. Further zoomed-in TEM image of the cross-section is displayed in Figure 5.17. It appears that annealing results in Cu cluster formation in the electrolyte. This behavior of Cu has been shown in other oxides such as Al_2O_3 [248], [249], GeO_x [250] and SiO_2 [251] before. In order to further prove that these clusters are Cu, high-resolution TEM (HR-TEM) images shown in Figure 5.18 (b) and (c) were analyzed by fast Fourier transform (FFT) analysis. Due to the small crystals or surrounding amorphous WO_3, the FFT is not clear. Calculated *d*-spacings are 2.134 Å (Figure 5.19) and 2.187 Å (Figure 5.20) which are close to the crystal *d*-spacing of pure face centered cubic Cu (111) (d~ 2.08 Å [252]). Slight increase of *d*-spacing can be attributed to the oxygen-rich environment in the host and its interaction with the copper. However, the very similar *d*-spacing suggests that Cu-Cu bonds make up most of the nanocrystals. The size of the clusters varies between 5.97 nm and 12.62 nm, where the size of the clusters in Figure 5.18 (b) and (c) is ~8.71 nm and ~7.15 nm respectively. The difference in calculated *d*-spacing is most likely due to the difference in cluster sizes. As the cluster size increases, *d*-spacing approaches the value of pure fcc Cu (111) owing to more Cu-Cu bonds.

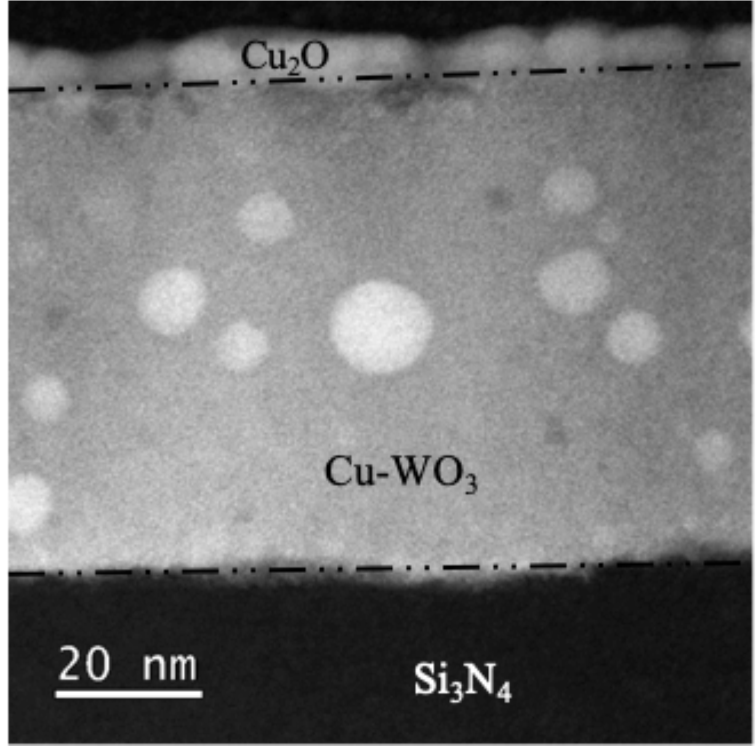

Figure 5.17: HR-TEM image of the cross-section of Sample 1.

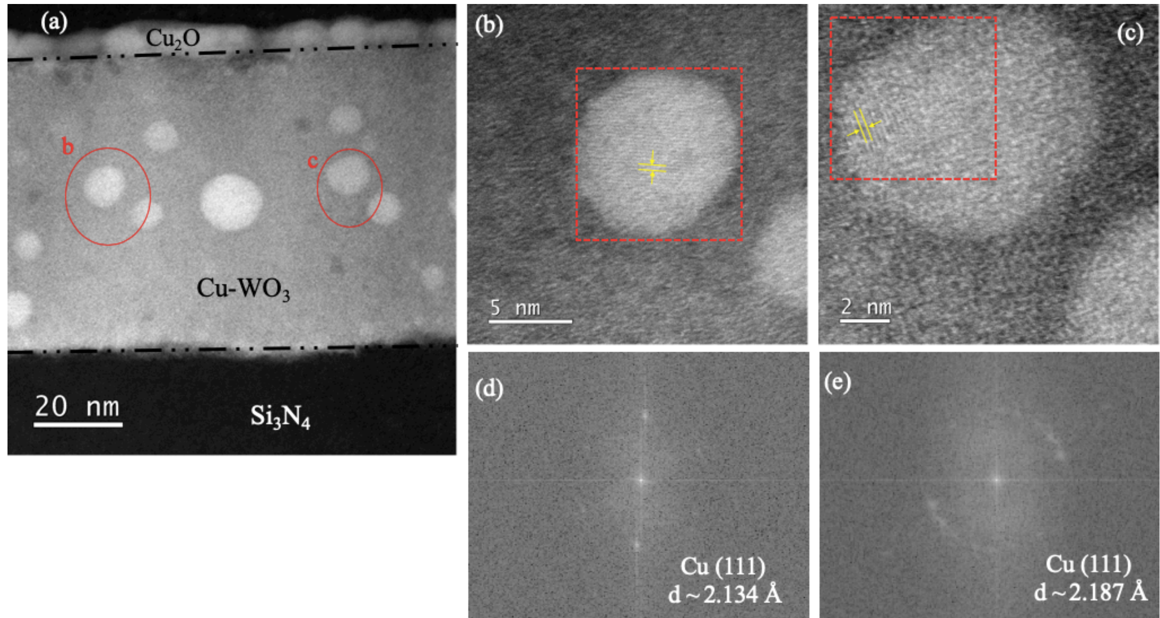

Figure 5.18: TEM analysis of the Sample 1. (a) HR-TEM image of the Sample 1, (b,c) HRTEM images of the spots indicated by red circles in (a), (d,e) FFT of (b) and (c) respectively showing Cu (111).

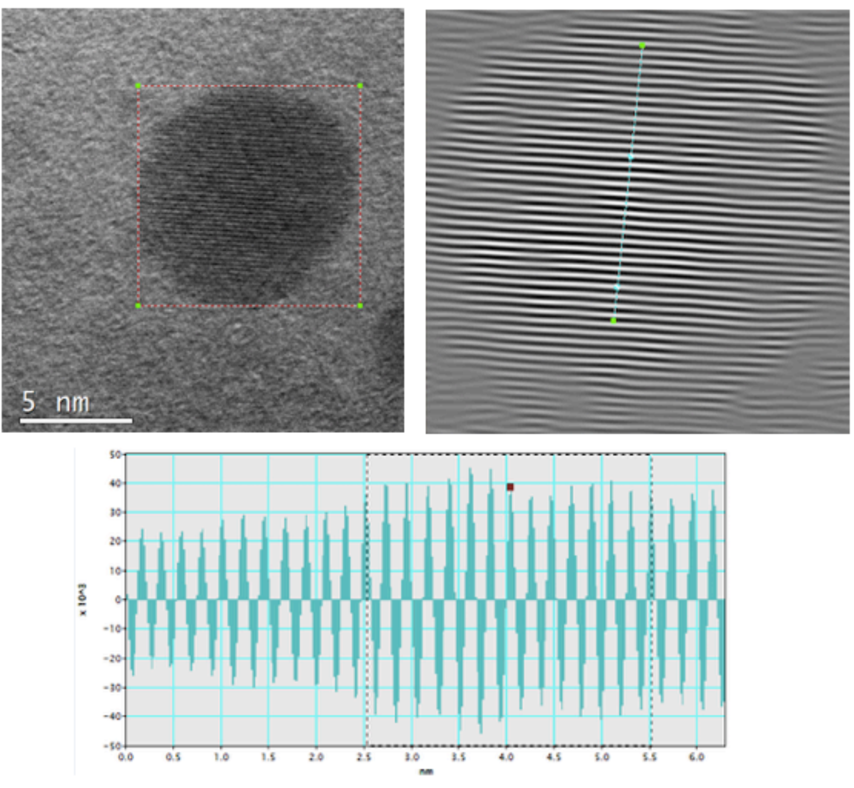

Figure 5.19: *d*-spacing calculation of the cluster in Figure 5.18b, *d*~ 2.134 Å.

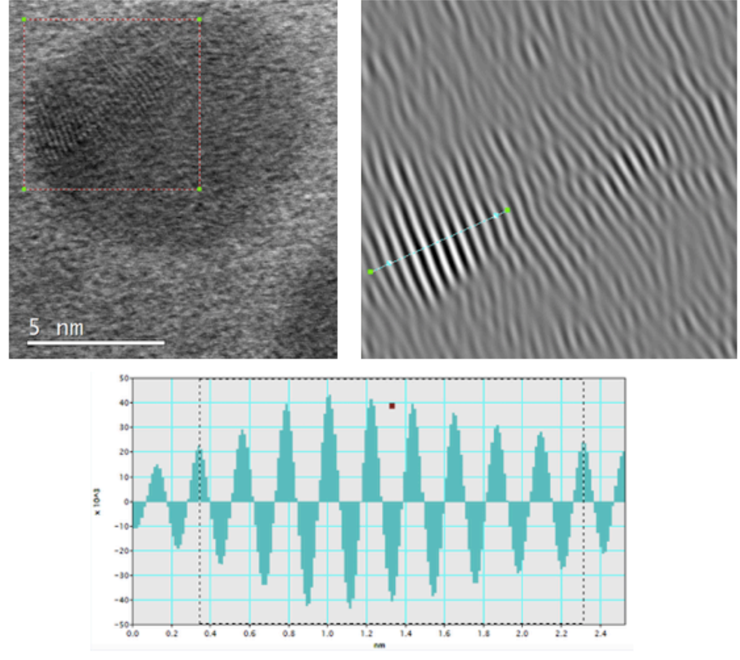

Figure 5.20: *d*-spacing calculation of the cluster in Figure 5.18c, *d*~ 2.187 Å.

5.2.4 XRD

Same samples made for TEM analysis were also analyzed by XRD using Cu-Kα beam on Bruker D8 Specialized Powder X-ray Diffractometer with detector scan configuration. The incident beam angle was set to ω=3° with the 0.6 mm slit while the detector was scanned from 10° to 80°. The scan rate was 7°/min where the x-rays were collected for 23 runs to improve the signal-to-noise ratio due to amorphous nature of WO_3. The XRD results are shown in Figure 5.21. WO_3 looks to be amorphous which is why it is labeled as WO_x as it could not be identified if it was WO_2 (PDF-00-032-1393) or WO_3 (PDF-00-032-1395). Strong crystalline Cu_2O peaks (PDF-04-007-9767) along with some crystalline Cu peaks (PDF-04-009-2090) are also present in the pattern. Increasing the annealing temperature and/or time not only results in increased Cu_2O (111) peak strength, but interestingly in increased Cu (111) peak too. Assuming that the penetration depth of the incident x-rays was comparable between the samples, Sample 3 has more metallic Cu than Sample 2, whereas metallic Cu in Sample 1 does not exist. This results in significant resistivity/conductivity changes in our samples (shown in Chapter 7) which affects the behavior of lateral PMC devices using the bilayer of Cu_2O/Cu-WO_3.

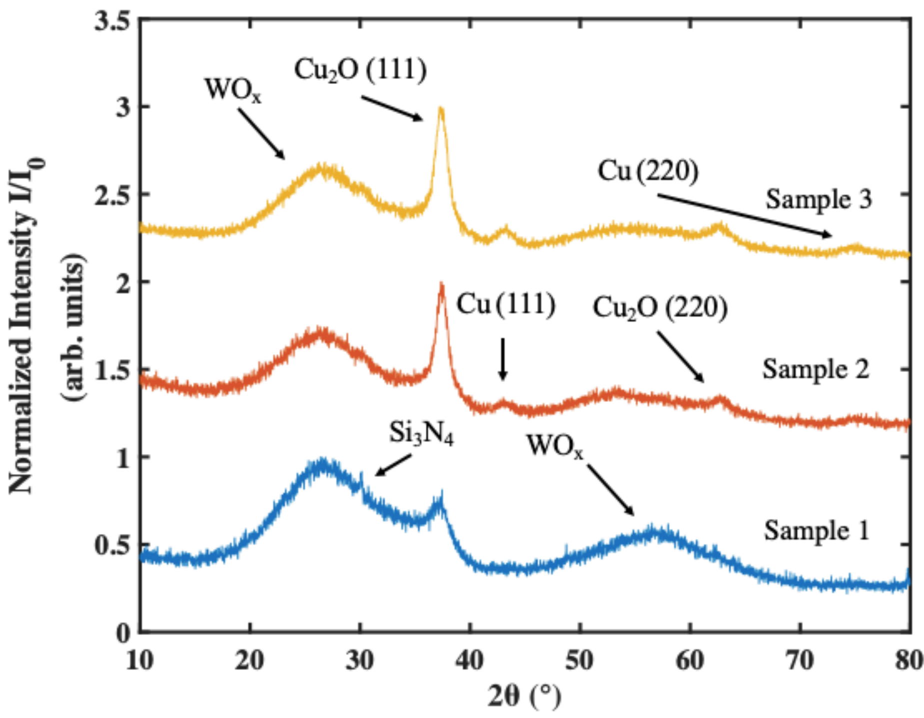

Figure 5.21: XRD patterns of TEM samples shown in Table 5.3.

CHAPTER 6

MODELING THE OXIDATION & DIFFUSION OF Cu/WO_3

6.1 Building the Model

After characterizing the oxidation kinetics of Cu and its diffusion into the solid electrolyte, a 1-D Matlab model was built. Along with the combined model of oxidation and diffusion, an oxidation model was also built due to the need. Table 6.1 shows the variables used in the model which are combination of experimentally extracted values and reported values in the literature (solid solubility of Cu in WO_3, density of Cu_2O). Complete code of oxidation and diffusion model can be found in Appendix B (Cu-WO_3 system).

Table 6.1: Variables Used in the Model for Cu-WO_3 System.

Variable Name	What It Is	Value
EaWO3 (eV)	Activation energy of diffusion of Cu in WO_3	0.742
Eacuox (eV)	Activation energy of diffusion of Cu in Cu_2O	0.697
D0 (cm^2/s)	Diffusion constant of Cu in WO_3	2.7333e-6
k0 ($cm.s^{-1/2}$)	Constant in the rate constant equation for oxidation	20.6972
R (eV/°K)	Boltzmann constant / Gas constant	8.617e-5
NAvog ($/cm^3$)	Avogadro's number	6.022e23
CuDens (g/cm^3)	Density of e-beam evaporated Cu	8.85
CuMolMass (g)	Molar mass of Cu	63.5 [187]
Cu2oDens (g/cm^3)	Density of Cu_2O	6 [253]
Cu2oMolMass (g)	Molar mass of Cu_2O	143 [187]
CuSSwo3 (at%)	Solid solubility of Cu in WO_3	0.56 [78]

The inputs of the model are deposited thickness of Cu (d_{Cu}), annealing temperature (T_{ann}) and annealing time (t) whereas oxygen partial pressure and WO_3 thickness are also optional inputs. The outputs of the model are the dose (Q in atoms/cm^2) of the diffused Cu and the semilog plot of concentration (atoms/cm^3) vs. depth (cm). As it is stated in the previous chapters, annealing Cu-WO_3 devices in air results in the oxidation of copper from the top and diffusion of copper at the Cu/WO_3 interface. As long as there is metallic copper left in the system, oxidation continues, and the diffusion can be modeled by the solution of the Fick's second law for the 'constant source' equation (5.5). Once there is no more metallic copper left, oxidation stops, and the diffusion can be modeled by the solution of the Fick's second law for the 'limited-source' equation (5.6). The model solves and plots the concentration vs. depth starting with time= 1 minute for each 1-minute increments until the input 'annealing time' is achieved.

6.2 Copper Oxidation Model

Oxidation model is relatively simple and straightforward. The inputs of the function (dCu2o.m) are temperature (in Celcius) and time (in minutes); and the outputs are the final Cu_2O thickness in nm and the minimum thickness of deposited Cu needed in nm. For example, dCu2o(155,50) returns 70.2834 and 42.596 which means that if the control sample had thick enough copper deposited (about 42.6 nm) and if it is annealed at 155 °C for 50 minutes, it will yield about 70.3 nm of Cu_2O. The code utilizes the parabolic law of oxidation along with equation (4.3) and the Cu_2O oxygen incorporation factor 1.65. The oxidation Matlab function dCu2o.m is given below.

```
function [dox,minCu] = dCu2o(temp,time)
R=8.617e-5;
Eacuox=0.697; %Activation energy of Cu in Cu20
k0=20.6972;
annT=273+temp; % conversion to Kelvin
t=time*60; % annealing time in seconds
k=k0*exp(-Eacuox/R/annT);
doxfinal=k*sqrt(t); %parabolic law
dox=doxfinal*1e7;
minCu=dox/1.65
end
```

6.3 Simulations of the Oxidation and Diffusion Model of Cu/WO_3

Inputs: d_{Cu} = 23 nm, T_{ann} = 140 °C, t = 40 minutes

Outputs: Q= 9.4467e16

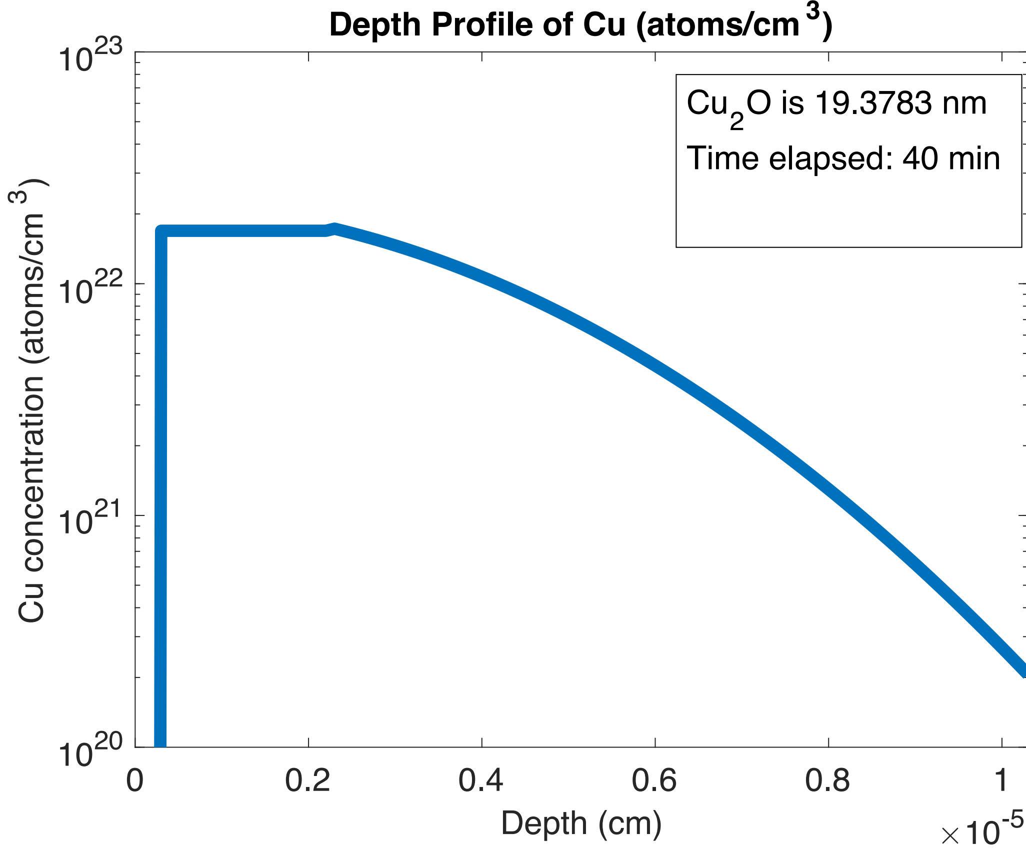

Figure 6.1: Cu concentration vs. depth for case 1. d_{Cu} = 23 nm, T_{ann} = 140 °C, t = 40 minutes.

Inputs: d_{Cu} = 20 nm, T_{ann} = 125 °C, t = 60 minutes

Outputs: Q= 9.5885e16

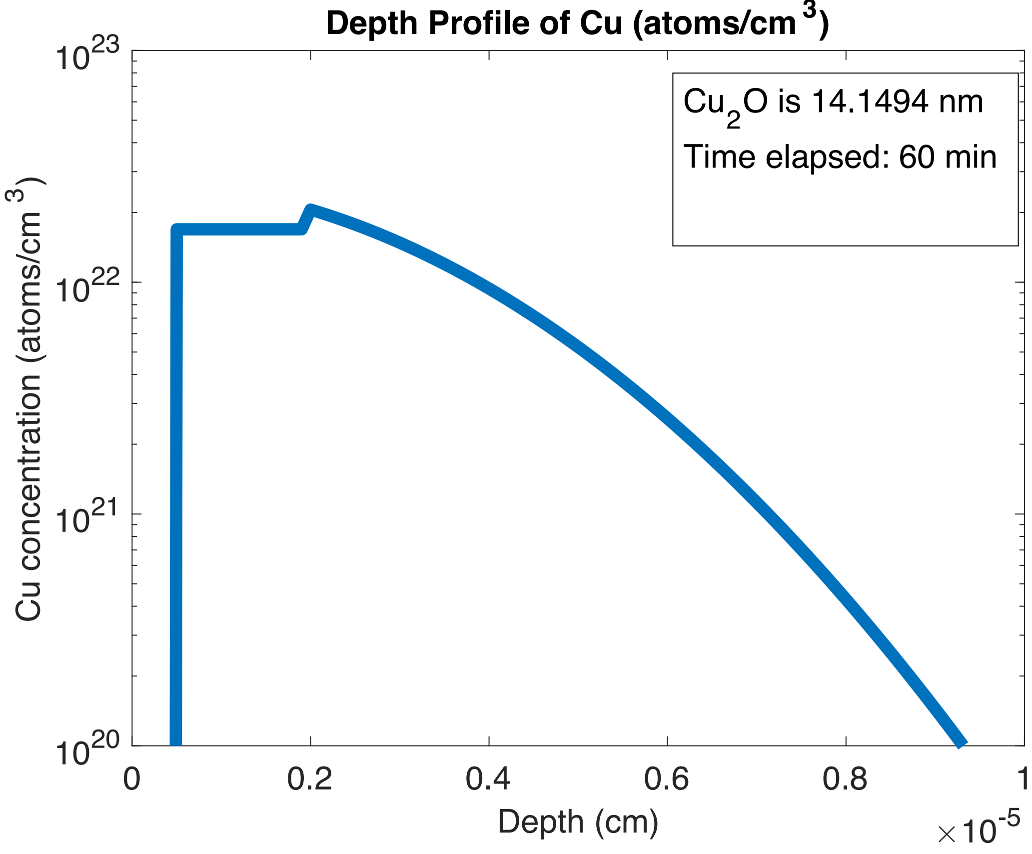

Figure 6.2: Cu concentration vs. depth for case 2. d_{Cu} = 20 nm, T_{ann} = 125 °C, t = 60 minutes.

Inputs: d_{Cu} = 30 nm, T_{ann} = 155 °C, t = 60 minutes

Outputs: Q= 1.0011e17

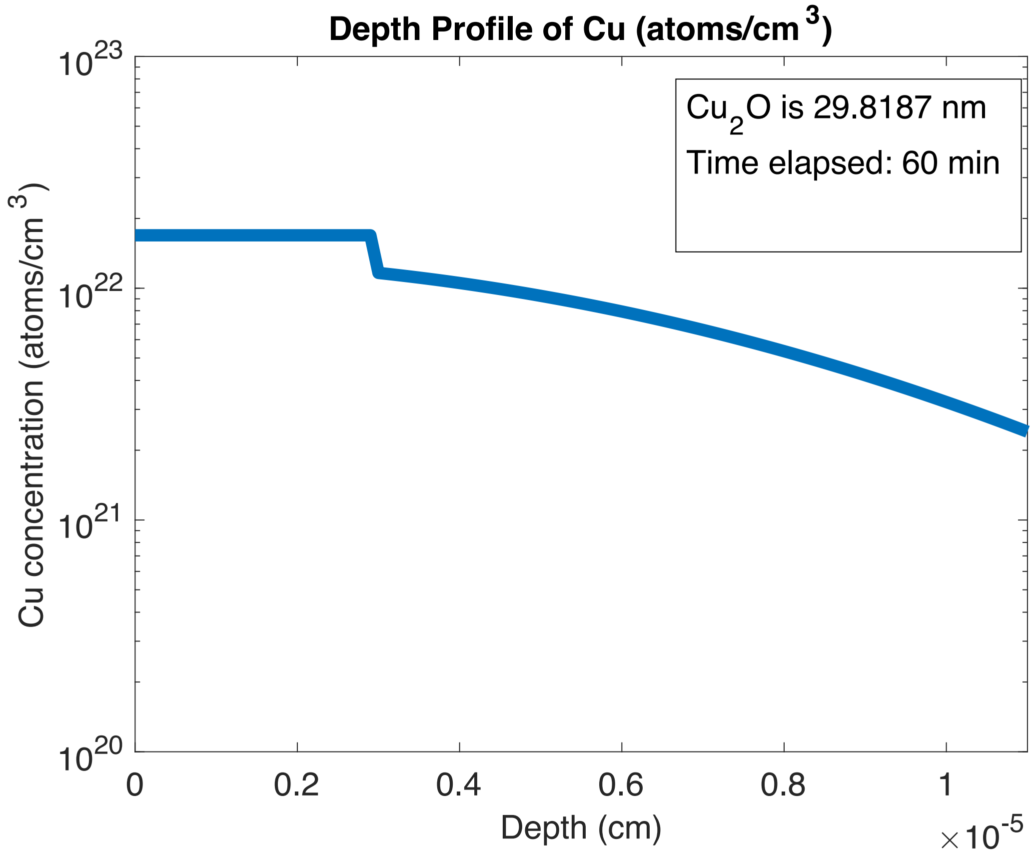

Figure 6.3: Cu concentration vs. depth for case 3. d_{Cu} = 30 nm, T_{ann} = 155 °C, t = 60 minutes.

Inputs: d_{Cu} = 25 nm, T_{ann} = 135 °C, t = 30 minutes

Outputs: Q= 1.0389e17

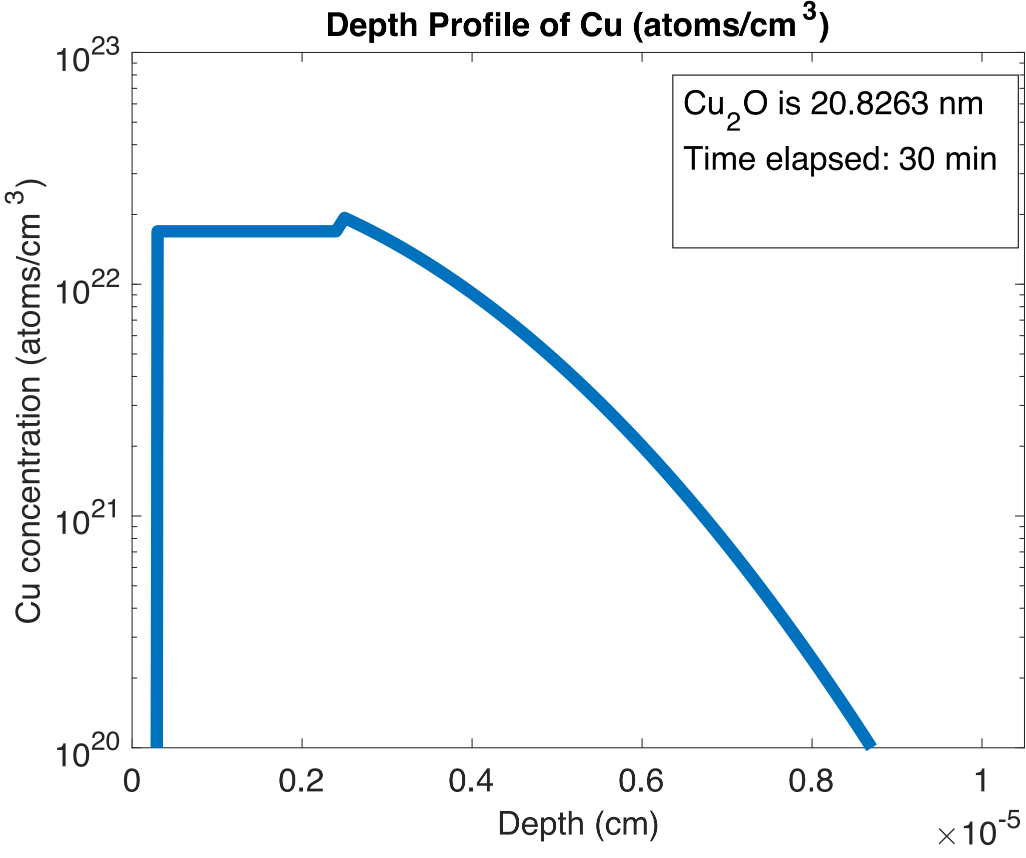

Figure 6.4: Cu concentration vs. depth for case 4. d_{Cu} = 25 nm, T_{ann} = 135 °C, t = 30 minutes.

Inputs: d_{Cu} = 25 nm, T_{ann} = 135 °C, t = 15 minutes

Outputs: Q= N/A due to still existing metallic Cu

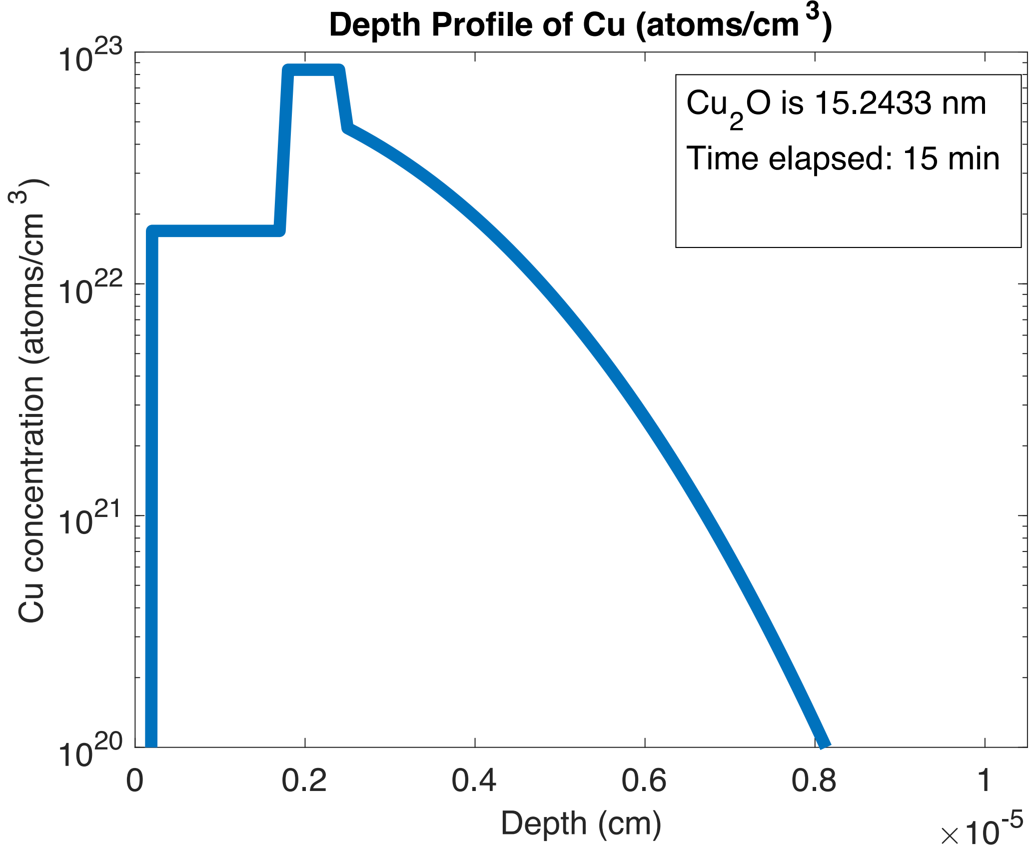

Figure 6.5: Cu concentration vs. depth for case 5. d_{Cu} = 25 nm, T_{ann} = 135 °C, t = 15 minutes.

CHAPTER 7

LATERAL PMC DEVICES USING Cu_2O/Cu-WO_3 BILAYER

7.1 Fabrication of Lateral PMC Devices

Three sets of lateral devices were fabricated to determine the capability of the bilayer for electrodeposition. Starting with a 4-inch Si wafer, 200 nm of Si_3N_4 was deposited by low pressure chemical vapor deposition (LPCVD) on the wafer. All layers were patterned using a photolithography – e-beam evaporation – lift-off sequence. First, the electrolyte pattern was exposed in a bilayer of OCG825 and AZ3312 photoresists spun on the Si_3N_4/Si using OAI 808 aligner. Next, a Cu/WO_3 stack with three different thicknesses of Cu was e-beam evaporated on the patterned resist using a Lesker PVD75 deposition system. This was done to provide different amounts of the metal for the oxidation/diffusion process. The WO_3 thickness was 80 nm in all cases. 10 nm of Cu was deposited for “device 1”, 20 nm of Cu was deposited for “device 2” and 30 nm of Cu was deposited for “device 3”. The Cu/WO_3 stack was then patterned by acetone liftoff to produce an electrolyte channel width of 50 μm. Subsequently, device 1 was annealed in air at 135 °C for 13 minutes, device 2 was annealed in air at 155 °C for 25 minutes and device 3 was annealed in air at 155 °C for 60 minutes. These times and temperatures were determined by using the Matlab model (Chapter 6 & Appendix B) based on the material analysis work to ensure complete Cu oxidation/diffusion so that no continuous metallic Cu film remained in the stack and thereby prevent electrodeposition. Moreover, the annealing conditions were chosen to have similar Cu concentrations at the WO_3 interface for all cases post-annealing. To complete the device structures, the Ni cathode and Cu anode and their

probe pads for external connections were deposited on top of the electrolyte layer using e-beam evaporation in the Lesker PVD75 and patterned by the sequence described above to produce an electrolyte channel length of 14 μm in both devices.

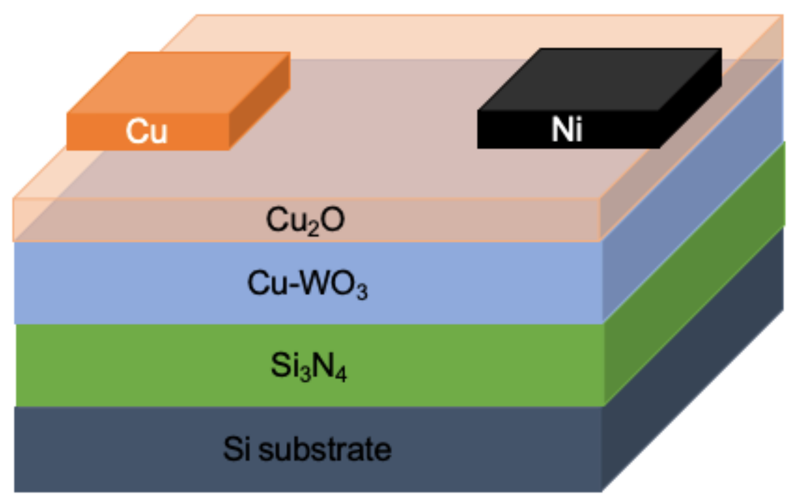

Figure 7.1: Idealized cross-section of the devices after annealing.

7.2 Characteristics of the Bilayer

Few parameters such as Cu concentration at the $Cu_2O/Cu\text{-}WO_3$ interface ($C_{Cu,i}$), total amount of Cu in the $Cu\text{-}WO_3$, the point where the Cu concentration reaches 5×10^{21} /cm^3 in $Cu\text{-}WO_3$, Cu_2O thickness, the time for all the metallic Cu to oxidize/diffuse (t_d) were extracted from the Matlab model. $C_{Cu,i}$ was determined to be 1.7×10^{22} /cm^3, 1.2×10^{22} /cm^3, and 1.2×10^{22} /cm^3 for device 1, device 2 and device 3 respectively. As expected, $C_{Cu,i}$ was very similar for all devices as the annealing conditions were chosen to achieve this case. The total amount of Cu in the 80 nm thick WO_3 was 5.5×10^{21} atoms in device 1, 8.3×10^{21} atoms in device 2 and 1.3×10^{22} atoms in device 3, and the point below the surface of the WO_3 at which the Cu concentration reached 5×10^{21} /cm^3 is approximately

18 nm in device 1, 34 nm in device 2 and 53 nm in device 3. These results suggest that the amount of Cu in the first few tens of nm of the WO_3 is quite similar for all samples, indicating that any significant differences in electrodeposition rate between the two devices would not be due to the Cu-WO_3 electrolyte. Concerning the overlying Cu_2O layer, the model showed that the copper oxide layer was 7.8 nm thick in device 1, 19.8 nm thick in device 2 and 29.9 nm thick in device 3. It was also determined that t_d was about 5 minutes for device 1 and device 2, and 10 minutes for device 3. This means that the bilayer was further annealed for 8 minutes, 20 minutes and 50 minutes for device 1, device 2 and device 3 respectively after getting rid of the deposited metallic Cu layer.

7.3 Results and Discussion

Electrical characterization was accomplished by applying constant voltage bias using an Agilent 4155C parameter analyzer connected via tungsten probes on a MicroZoom probe station to the probe pads and the current was measured over time. The high resistance state (HRS), starting resistance, for device 1 was 15 GΩ and for device 3 was 25 MΩ. Using these resistance values and device dimensions, and assuming that the copper oxide layer has a lower resistance than the Cu-doped WO_3 [76], [178], the copper oxide resistivity in device 1 is around 43 kΩ.cm which implies that we have "pure" Cu_2O and the layer resistivity in device 3 is around 270 Ω.cm which implies a Cu_2O + Cu mix [178]. Presence of Cu_2O + Cu in the bilayer of device 2 and device 3 was also verified by XRD post-annealing (Chapter 5, Figure 5.21). This behavior of partial oxidation of Cu into Cu + Cu_2O at low temperatures was also previously reported where presence of Cu disappears around 200 °C [178]. The lower resistance layer in device 2 and device 3 allows

a much greater electron supply for Cu ion reduction and this should result in faster electrodeposition at the anode.

Because the bilayer of device 2 and device 3 showed similar resistivity, current-time characteristics of device 1 compared to device 3 was investigated. Constant voltage of 5 V was applied to the anode of device 3 while the cathode was grounded. The electrodeposit bridged the channel in 29 seconds, as determined by the point where the current suddenly reached the compliance limit as shown in Figure 7.2. The same bias (5 V) for device 1 resulted in no noticeable change in resistance during testing over tens of hours, so the bias was increased to 60 V. The electrodeposit, with the increased bias, bridged the channel in around 3.5 hours, also shown in Figure 7.2. The average electrodeposition rates for these bias conditions were 0.0011 µm/s and 0.48 µm/s for device 1 and device 3 respectively. The low resistance state (LRS) in both devices was determined by the current compliance, which is typical for PMC devices [50].

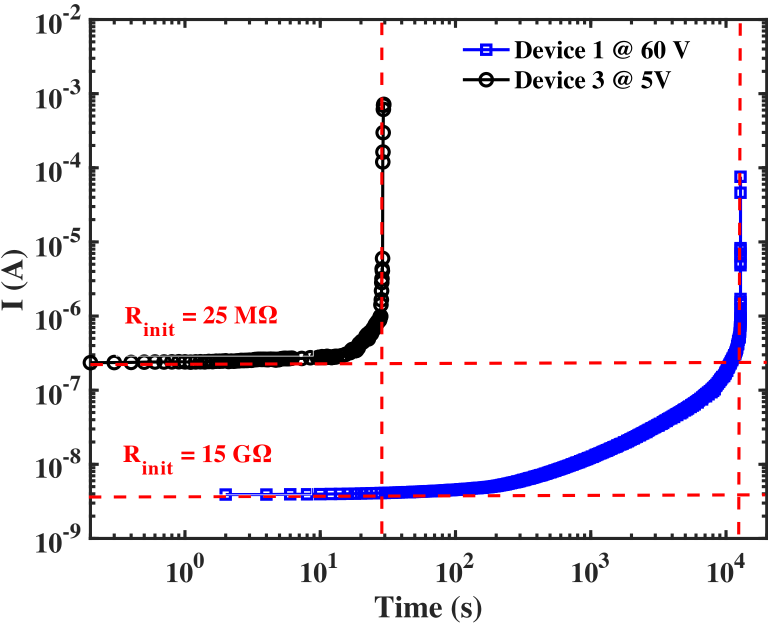

Figure 7.2: Current-time plots of device 1 and device 3.

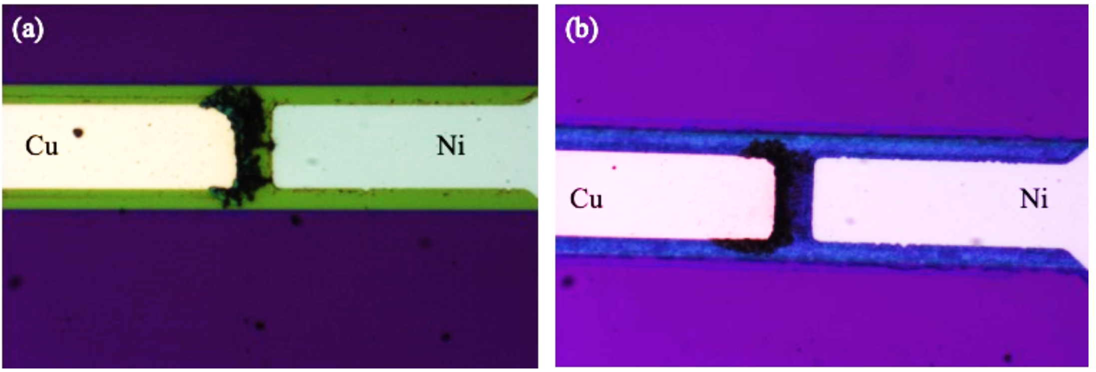

Figure 7.3: Optical micrographs of (a) device 1 and (b) device 3 post-biasing.

Optical micrographs of device 1 and device 3 following the electrodeposition bridging the channel are given in Figure 7.3. The darker color of the electrodeposit is due to its roughness.

The activation energy of conduction ($E_{\sigma,a}$) obtained from high temperature measurements in HRS was found to be 0.64 eV, 0.20 eV and 0.30 eV for device 1, device 2 and device 3 respectively [254]. The calculated $E_{\sigma,a}$ values for device 2 and device 3 are comparable to previously reported values in Cu_xO where x = 1, 2 [255]–[259] and the calculated $E_{\sigma,a}$ value for device 1 is comparable to previously reported value in amorphous WO_3 [260]. Disparity in values of $E_{\sigma,a}$ between device 1 and device 3 can be explained by the lower resistivity of the Cu_2O layer due to partial oxidation (Cu + Cu_2O mix) in device 3. The Cu_2O thickness of ~8 nm for device 1 indicates that the Cu_2O was formed by the surface diffusion of oxidation [202], [203] leading to a uniform Cu_2O layer. This dramatic reduction in the activation energy of conduction eventually causes the electrodeposit to form much quicker at lower applied voltages. The huge difference also suggests that Cu ions in device 3 are most likely reduced near the anode where electrons are supplied by the Cu_2O layer, whereas Cu ions in device 1 need to migrate all the way to the cathode and are

reduced by the electrons near the cathode. As revealed by the XRD patterns of the bilayers of device 2 and device 3 (Figure 5.21), Cu was present in both cases as mentioned earlier. Therefore, the difference in $E_{\sigma,a}$ for device 2 and device 3 was most likely due to the difference in grain sizes of the Cu_2O. The annealing temperature was the same for device 2 and device 3, however calculated t_d values were 20 minutes and 50 minutes respectively. The grain growth kinetics follow,

$$D^n - D_0^n = kt \tag{7.1}$$

where t is the annealing time, D is the grain size at time t, D_0 is the initial grain size, n is the grain growth exponent (where n is expected to be ~3 [261], [262]) and k is the temperature-dependent kinetic coefficient. Because the bilayer in device 3 was annealed 30 minutes longer than device 2 at the same temperature post-oxidation/diffusion of the deposited Cu layer, the average grain size of Cu_2O in device 3 is expected to be larger. This means that the number of grain boundaries (GBs) per area in device 2 is expected to be greater. Having higher number of GBs per area in device 2 facilitates the mass transport in the copper-oxide layer [263], [264] thus leading to lower $E_{\sigma,a}$.

Next, grown electrodeposit on another device was investigated. This device (referred to as TEM device) had a very similar structure to device 3 where the only difference was the bridge channel was 40 μm. The device was fabricated and biased for the TEM analysis because longer channel facilitated TEM sample preparation. A constant voltage of 20 V was applied to the anode while the cathode was grounded until electrodeposits were formed. TEM imaging along with EELS was done to examine where the electrodeposit grew in the TEM device. TEM sample was prepared by focused ion beam (FIB) using Nova 200 NanoLab, which is a SEM tool equipped with FIB, and

HRTEM analysis was performed using JEOL ARM 200F. Before the FIB cut, the device was coated with carbon so that the surface was conductive all around to enable imaging in SEM. Then, a thick layer of Pt was deposited to allow the FIB cut to performed with minimal damage to the device. The optical micrograph of the bridged device before TEM sample preparation and the SEM image pre-FIB-cut are given in Figure 7.4.

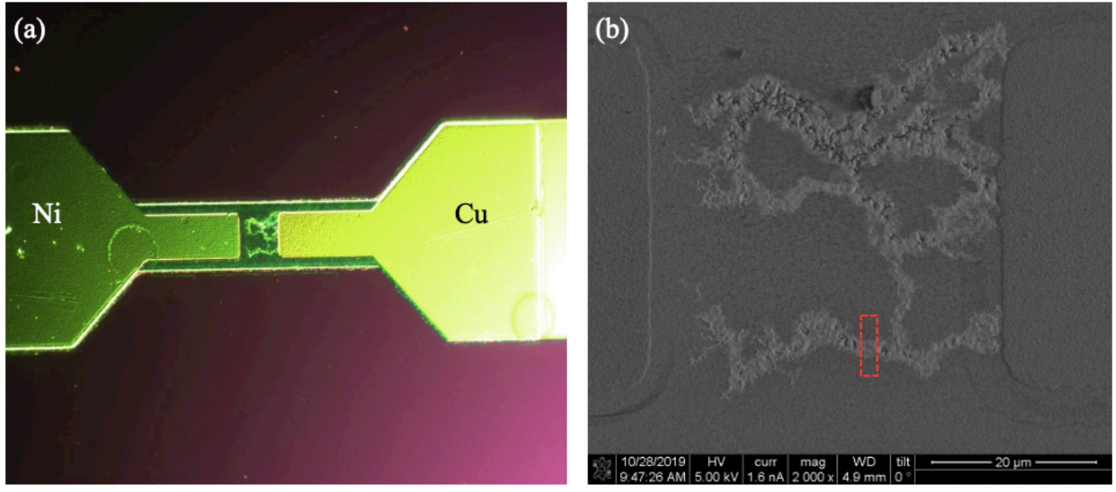

Figure 7.4: (a) Optical micrograph of the device post-bridging, (b) SEM image of the same device. Red highlighted rectangle in b shows where the FIB cut was made.

The electrodeposit growth was found to be at the interface of Cu_2O/Cu-WO_3 as displayed in Figure 7.5. Electrodeposition of the Cu growth is supplied by the Cu-WO_3 layer and this is suggested by the wider base of the electrodeposit.

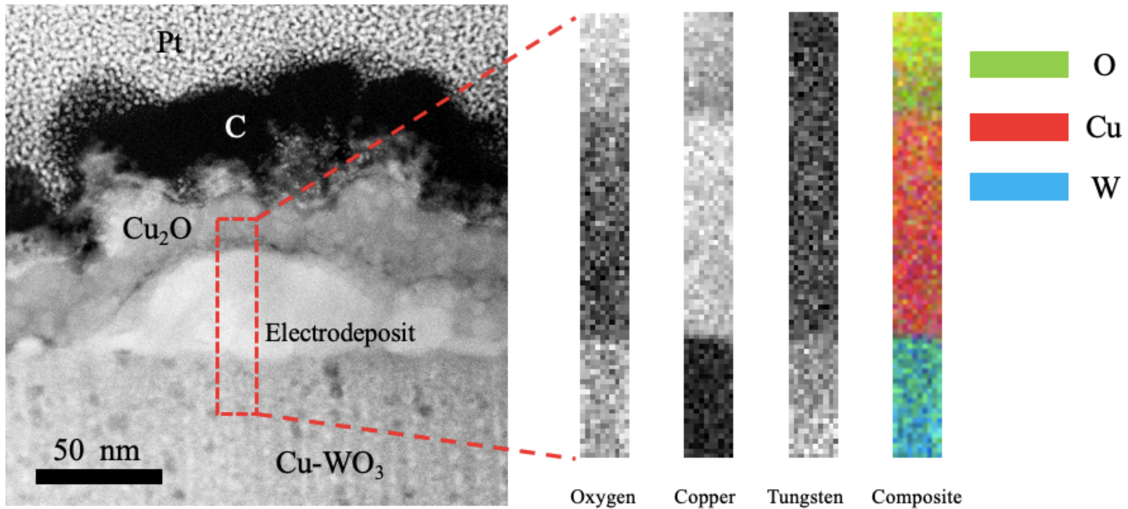

Figure 7.5: TEM analysis of the electrodeposit. (left) TEM cross-section image of the red rectangle shown in Figure 7.4b, (right) EELS oxygen map, copper map and tungsten map showing that the electrodeposit is metallic Cu.

Current – time plots of device 1 and device 3 given in Figure 7.2 provide insightful information on how each device is bridged. Fairly constant current over time for device 3 suggests that the current is due to the low-resistive Cu_2O layer that supplies electrons to the ionized Cu. These electrons rapidly reduce the Cu ions near the anode which was also observed during testing. The fast electrodeposition is not believed to change the overall resistance of the cell until the channel is almost bridged. Right before the electrodeposit shorts the electrodes, resistance of the cell begins to be dominated by the filament and the final stages of the electrodeposit growth, and bridging makes the current to increase suddenly until it reaches the compliance. However, in device 1, ionized Cu has to migrate all the way to the cathode first where the electrons are abundant resulting in Cu ion reduction at the cathode site. During the electrodeposition growth, the slow growth enables the filament to gather Cu from the surrounding host (Cu-WO_3) which leads to gradual increase in resistance of the cell. This effect can clearly be seen for device 1 after ~ 100

seconds in Figure 7.2. This allows for a bilayer resistance model (Figure 7.6) to be used for device 1 where some parameters about the material system can be extracted using the Mott-Gurney model [3], [4] along with the resistance model.

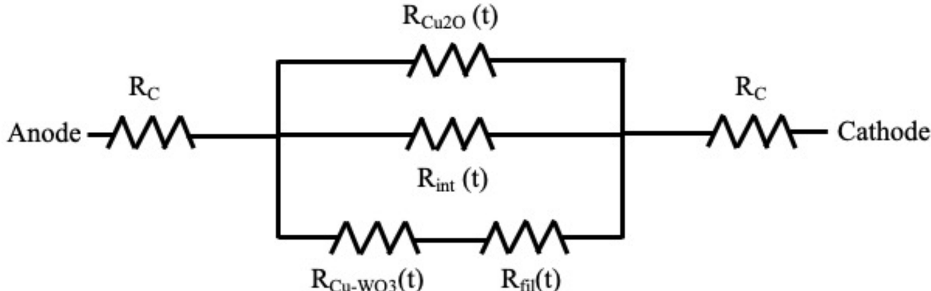

Figure 7.6: Bilayer resistance model. R_{Cu2O} (t) is the resistance of the Cu_2O layer, R_{Cu-WO3}(t) is the resistance of the solid electrolyte R_{fil}(t) is the resistance of the filament, R_{int} (t) is the resistance of the interface where the electrodeposit grows, R_c is the resistance between the anode/cathode and the interface.

The resistance between the anode (also cathode) and the interface, R_c, may have an impact on the switching due to supplied ions needing to travel through the thin Cu_2O layer and get to the interface where the electrodeposition occurs. Assuming a square area for the electrode (50 μm x 50 μm) and ~ 40 kΩ.cm for the resistivity of the Cu_2O layer, R_c is calculated to be ~ 1.3 kΩ. Because this value is relatively very low, the model can be simplified further as shown in Figure 7.7.

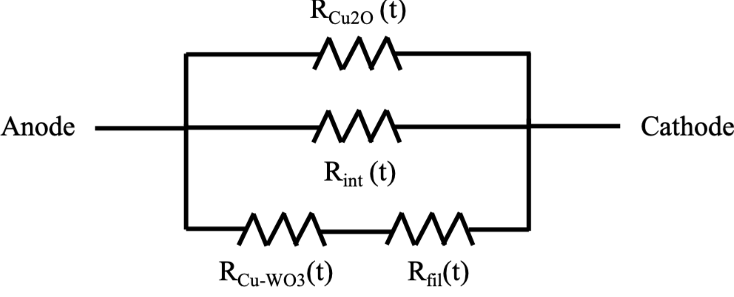

Figure 7.7: Simplified bilayer resistance model.

Electrodeposit growth rate in a PMC can be expressed as,

$$\frac{dh}{dt} = \frac{2N_i u_{th}}{N_f} \exp\left(-\frac{E_0}{kT}\right) \sinh\left(\frac{azqV_c}{2kT(L-h(t))}\right) \tag{7.1}$$

where h is the filament length, t is the time, N_i is the cation concentration (5.5×10^{21} /cm^3), u_{th} is the thermal velocity (2.8×10^4 cm/s for Cu^{2+} [50]), N_f is the Cu filament metal density (8.4×10^{22} /cm^3), E_0 is the barrier height (assumed to be 0.6 eV due to large applied bias), kT is the thermal energy, a is the mean ionic hopping distance, z is the charge of the ions (2 for Cu^{2+}), q is the electron charge, V_c is the cell bias (60 V) and L is the channel length (14 µm). The only unknown in this equation is the mean ionic hopping distance. By using time-to-bridge (t_s = 3.5 hours), and simulating the filament length over time (Figure 7.8) with the following equation derived from equation 7.1,

$$t_s = \left[\frac{2N_i u_{th}}{N_f} \exp\left(-\frac{E_0}{kT}\right)\right]^{-1} \left[\int_0^L \sinh\left(\frac{azqV_c}{2kT\big(L-h(t)\big)}\right) dh\right]^{-1} \tag{7.2}$$

the mean ionic hopping distance is obtained to be 1.1 nm.

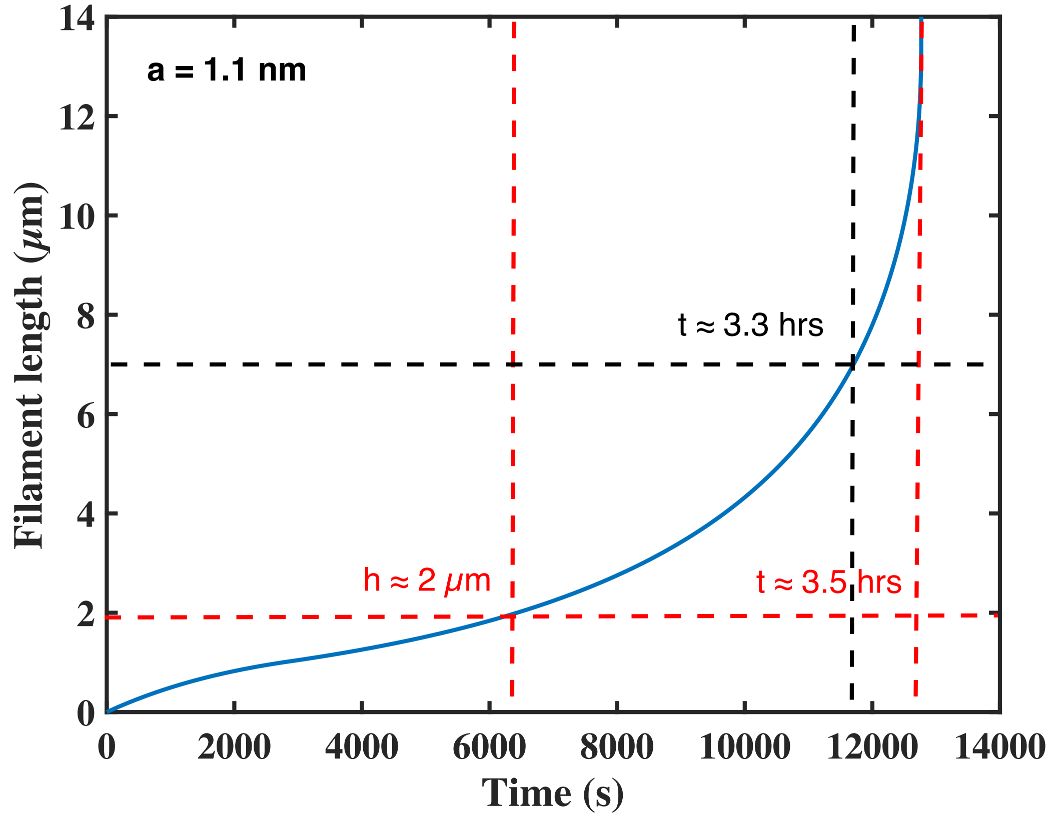

Figure 7.8: Simulation result showing filament length vs time.

Obtained a = 1.1 nm for Cu in WO_3 is very similar to the values used in simulations or other extracted values of hopping distance of Cu in sputtered SiO_2 ~ 1.3 nm [265], Cu in thermal SiO_2 ~ 2.2 nm [266], Cu in SiCOH ~ 1.5 nm [147]. After obtaining the mean hopping distance, the vibrational frequency (v) can be calculated by u_{th} = av, where v is 2.5 × 10^{11} Hz which is similar to the value used in the literature [50]. The slow electrodeposition/low ion mobility can also be seen by the half-way point where the time it takes the filament to reach 7 μm is ~ 3.3 hours. After this point, due to the enhanced electric field, it only takes the filament ~ 12 minutes to bridge the channel. Also, filament length at half-time point (half of the time it takes to bridge) is about 2 μm. Both half-way and half-time point is in fact, similar to the behavior seen during testing. It takes a very

long time for the electrodeposit to grow at first, and then when the filament reaches about the half-way point, the growth rate increases rapidly. In order to achieve such growth rate, the cation concentration had to be varying over time. During the initial stages of the electrodeposition, the filament consumes large amount of the cations in the solid electrolyte, creating a region depleted of cations. In the meantime, Cu anode is supplying Cu ions to the solid electrolyte, however due to long channel length and low diffusivity/mobility of Cu, it takes a long time for the supplied ions to reach near the filament. This behavior is simulated (in Figure 7.9) as such that Cu cation concentration, at first, dips to a certain value and then increases back up. The conductivity increasing during switching hints on that the cation concentration actually increases to a value higher than its original value.

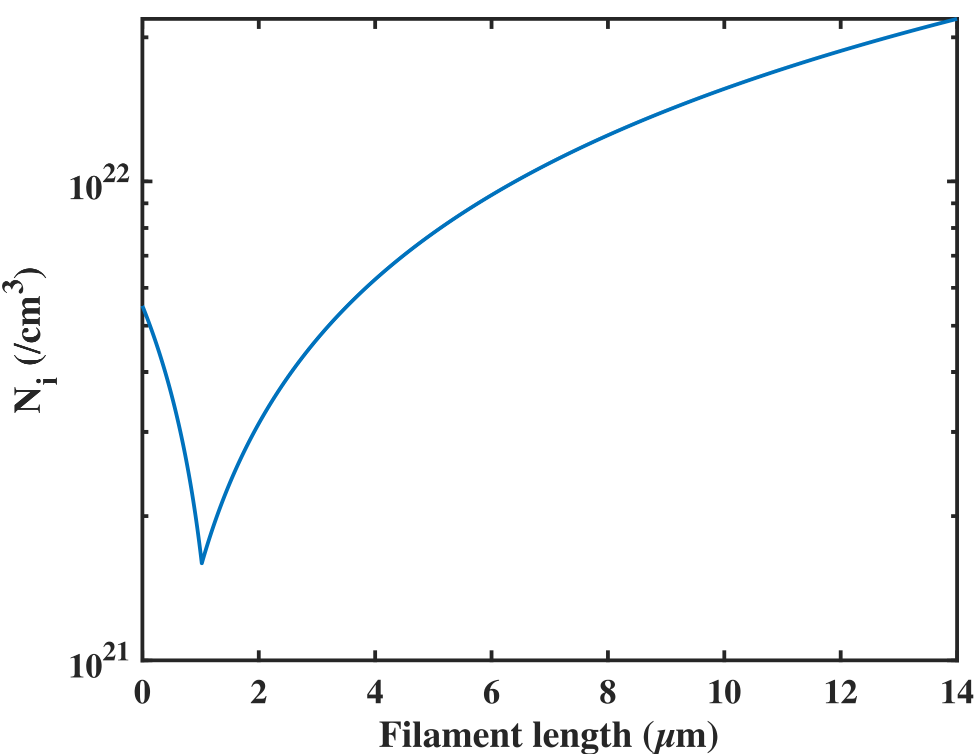

Figure 7.9: Simulated cation concentration vs filament length.

Next, using the resistance model where the ionic current (Mott-Gurney) should be the same as the current passing through the $R_{Cu\text{-}WO3}(t)$ and $R_{fil}(t)$, resistivity of the solid electrolyte $\rho_{Cu\text{-}WO3}$ can be obtained. The resistance of the cell will be,

$$R(h) = \frac{\rho_{Cu} h}{A_{fil}} + \frac{\rho_{Cu-WO3}(L-h)}{A_{Cu-WO3}} \tag{7.3}$$

where ρ_{Cu} is the resistivity of the copper filament (1.7 μΩ.cm [134]), A_{fil} is the cross-sectional area of the filament, $A_{Cu\text{-}WO3}$ is the cross-sectional area of the solid electrolyte. A_{fil} is assumed to have a circular shape with ~ 50 nm in diameter (see Figure 7.5) and $A_{Cu\text{-}WO3} = 4 \times 10^{-8}$ cm^2. Plotting both the current density over filament length from the Mott-Gurney model and the current density going through the resistance in equation 7.3 indicates $\rho_{Cu\text{-}WO3} \approx 30$ MΩ.cm (see Figure 7.10) which is similar to the previously reported values of Cu-WO_3 resistivity [76].

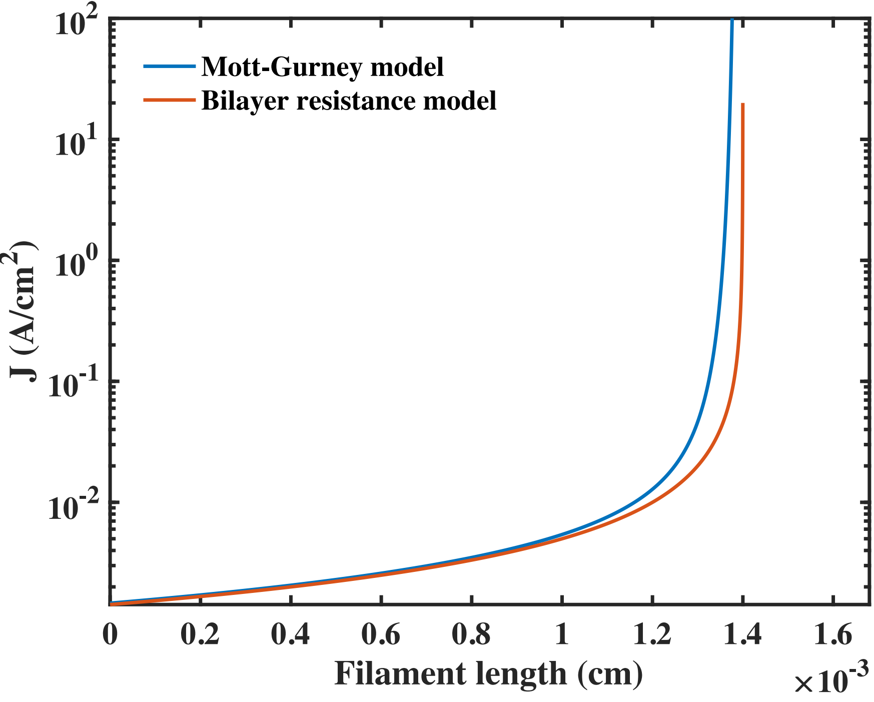

Figure 7.10: Current density vs filament length.

The semiconductor current (I_{Cu2O}) is simply calculated by the following equation,

$$I_{Cu2O} = \sigma\, E\, A_{Cu2O} = \frac{V_c\, W_e\, t_{Cu2O}}{\rho_{Cu2O}(L-h)} \tag{7.4}$$

where σ is the conductivity of the Cu_2O layer, E is the electric field, A_{Cu2O} is the cross-sectional area, W_e is the width of the electrode, t_{Cu2O} is the thickness of the Cu_2O, ρ_{Cu2O} is the resistivity of the Cu_2O layer.

Finally, the resistance of the interface, R_{int} (t), is simulated. Due to the small ionic current, even with the adjusted cation concentration, and the behavior of the I-t curve showing increase in conductivity, it is believed that the R_{int} was changing with time. Therefore, a time-dependent interface current (I_{int}) is fitted to the total current where the fitting showed a ~ $\rho_{Cu\text{-}WO3}/t^{0.8}$ dependence and it is shown in Figure 7.11.

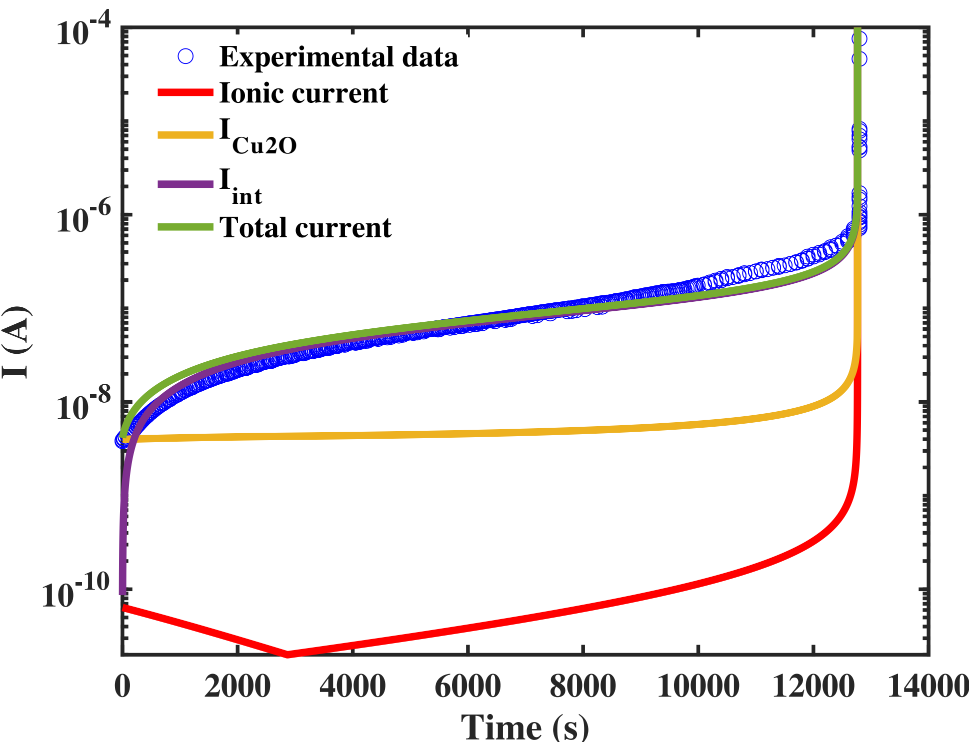

Figure 7.11: Simulated current through the entire resistance model

CHAPTER 8

CONCLUSION

In this dissertation, analysis and modeling of foundry-compatible PMC materials is presented. The main contribution of this dissertation was the fact that by changing fabrication parameters and processing conditions, materials with different properties could be obtained. These different material properties were shown to have a dramatic impact on the PMC device characteristics. Study on the performance of Cu-SiO_x vertical devices showed that forming voltage (V_F) and initial resistance (R_i) of a cell was greatly influenced by the annealing conditions and the cathode material. Using W instead of Ni resulted in devices with much lower V_F and R_i values. This was believed to be due to rougher interface created at the cathode/solid-electrolyte interface by the higher melting temperature of W which also possibly led to more columnar structures in the SiO_x which facilitated easier transport of Cu ions. Also, it was found that the effects of the densification of the SiO_x layer was more pronounced up to 500 °C which at first led to increase in V_F, but doping of Cu into the SiO_x was more dominating at 550 °C which drastically reduced the V_F by forming Cu islands at the Cu/SiO_x interface for the W-based devices. Moreover, analysis of thin-film Cu oxidation in air at low temperatures (125 °C – 170 °C) revealed that Cu oxidized into Cu_2O with the activation energy (E_a) of 0.70 eV. The calculated E_a suggested that the diffusion mechanism is mostly defect-related grain boundary diffusion. The feature sizes on the surface of Cu_2O was analyzed by image processing and it showed an increase in size with both annealing time and temperature. Furthermore, diffusion investigation of Cu into WO_3 showed that Cu formed clusters in the WO_3 host matrix, and the activation

energy of diffusion was found to be 0.74 eV in the temperature range of 125 °C – 155 °C. Analysis of Cu oxidation and diffusion of Cu into WO_3 enabled for a Matlab model to be built that assisted the formation of Cu_2O/Cu-WO_3 bilayers that were used in lateral PMC devices. The bilayer was formed by thermal processing of deposited Cu/WO_3 stack at low temperatures in air which caused the oxidation of Cu from the top and a simultaneous diffusion at the Cu/WO_3 interface. Bilayers with different electrical characteristics were established by controlling the deposited Cu thickness and annealing conditions. Low temperature annealing of the deposited stack with Cu thicknesses larger than 20 nm led to a Cu_2O layer that exhibited Cu + Cu_2O mix that reduced the resistivity. This low resistive characteristic of the formed Cu_2O layer resulted in a higher electron supply to the Cu ions that were reduced closer to the anode which enhanced the electrodeposition rate ($E_{\sigma,a}$ ~ 0.20 – 0.30 eV). On the other hand, annealing the stack with the 10 nm of deposited Cu resulted in a very thin Cu_2O layer with higher resistivity that showed reduction of Cu ions closer to the cathode with slower electrodeposition rate ($E_{\sigma,a}$ ~ 0.64 eV). This wide range of electrodeposition rate proved that devices with different time-to-bridge values could be obtained for lateral PMC devices by optimizing the annealing conditions and deposited Cu thicknesses.

This dissertation presents a comprehensive study on analysis and modeling of foundry compatible programmable metallization cell materials and devices and provides a solid foundation for interesting future work. First of all, a detailed study on the electrical performance and modeling of the Cu_2O/Cu-WO_3 bilayer lateral PMC devices must be performed. Furthermore, because SiO_x is also a widely used BEOL-compatible PMC material, similar Cu diffusion study into SiO_x along with potential Cu_2O/Cu-SiO_x bilayer

lateral PMC devices should be investigated. Moreover, fine tuning of the interesting behavior of Cu_2O (low and high resistivity) for lateral PMC device applications should be explored.

REFERENCES

[1] H. J. Schmidt and D. Volke, “Shift of meaning and students’ alternative concepts,” *Int. J. Sci. Educ.*, vol. 25, no. 11, pp. 1409–1424, 2003.

[2] A. J. Bard, *Electrochemical methods : fundamentals and applications*, 2nd ed.. New York ; Chichester [England]: John Wiley, 2001.

[3] N. F. Mott, *Electronic processes in ionic crystals,* 2d ed.. Oxford: Clarendon Press, 1957.

[4] J. J. O’Dwyer, *The theory of electrical conduction and breakdown in solid dielectrics,*. Oxford: Clarendon Press, 1973.

[5] E. E. Mendez and G. Bastard, “WannierStark Ladders and Bloch Oscillations in Superlattices,” *Phys. Today*, vol. 46, no. 6, pp. 34–42, 1993.

[6] G. M. Moore, “Moore’s Law ,Electronics,” vol. 38, no. 8, p. 114, 1965.

[7] W. Weinreich *et al.*, “Scaling and optimization of high-density integrated Si-capacitors,” in *2013 IEEE International Semiconductor Conference Dresden - Grenoble: Technology, Design, Packaging, Simulation and Test, ISCDG 2013*, 2013, pp. 1–4.

[8] R. E. Fontana, S. R. Hetzler, and G. Decad, “Technology roadmap comparisons for TAPE, HDD, and NAND flash: Implications for data storage applications,” *IEEE Trans. Magn.*, vol. 48, no. 5 PART 1, pp. 1692–1696, 2012.

[9] Y. Ji, J. Hu, and M. Lanza, “A future way of storing information: Resistive random access memory,” *IEEE Nanotechnol. Mag.*, vol. 9, no. 1, pp. 12–17, 2015.

[10] Z. Li, R. Zhou, and T. Li, “Exploring high-performance and energy proportional interface for phase change memory systems,” *Proc. - Int. Symp. High-Performance Comput. Archit.*, no. 2, pp. 210–221, 2013.

[11] G. W. Burr *et al.*, “The inner workings of phase change memory: Lessons from prototype PCM devices,” *2010 IEEE Globecom Work. GC’10*, no. c, pp. 1890–1894, 2010.

[12] H. S. P. Wong *et al.*, “Phase Change Memory,” in *Proceedings of the IEEE*, 2010, vol. 98, no. 12, pp. 2201–2227.

[13] J. Li and C. Lam, “Phase Change Memory,” *Sci. China Inf. Sci.*, vol. 54, pp. 1061–1072, 2011.

[14] S. Paul, S. Mukhopadhyay, and S. Bhunia, “A circuit and architecture codesign approach for a hybrid CMOS-STTRAM nonvolatile FPGA,” *IEEE Trans. Nanotechnol.*, vol. 10, no. 3, pp. 385–394, 2011.

[15] S. Chatterjee, M. Rasquinha, S. Yalamanchili, and S. Mukhopadhyay, “A scalable design methodology for energy minimization of STTRAM: A circuit and architecture perspective,” *IEEE Trans. Very Large Scale Integr. Syst.*, vol. 19, no. 5, pp. 809–817, 2011.

[16] A. Iyengar, S. Ghosh, and S. Srinivasan, “Retention Testing Methodology for STTRAM,” *IEEE Des. Test*, vol. 33, no. 5, pp. 7–15, 2016.

[17] F. Lentz, B. Roesgen, V. Rana, D. J. Wouters, and R. Waser, “Current compliance-dependent nonlinearity in TiO2 ReRAM,” *IEEE Electron Device Lett.*, vol. 34, no. 8, pp. 996–998, 2013.

[18] R. Waser, “Electrochemical and thermochemical memories,” in *2008 IEEE International Electron Devices Meeting*, 2008, pp. 1–4.

[19] E. Vianello *et al.*, “Metal Oxide Resistive Memory (OxRAM) and Phase Change Memory (PCM) as Artificial Synapses in Spiking Neural Networks,” in *2018 25th IEEE International Conference on Electronics Circuits and Systems, ICECS 2018*, 2019, pp. 561–564.

[20] S. Chatterjee, S. Salahuddin, S. Kumar, and S. Mukhopadhyay, “Modeling of the self-heating in STTRAM and analysis of its impact on reliable memory operations,” *Proc. - 2009 10th Non-Volatile Mem. Technol. Symp. NVMTS 2009*, no. c, pp. 86–89, 2009.

[21] R. Govindaraj and S. Ghosh, “Design and Analysis of STTRAM-Based Ternary Content Addressable Memory Cell,” *ACM J. Emerg. Technol. Comput. Syst.*, vol. 13, no. 4, pp. 1–22, 2017.

[22] R. Waser and M. Aono, “Nanoionics-based resistive switching memories,” *Nat. Mater.*, vol. 6, pp. 833–840, 2007.

[23] A. Beck, J. G. Bednorz, C. Gerber, C. Rossel, and D. Widmer, “Reproducible switching effect in thin oxide films for memory applications,” *Appl. Phys. Lett.*, vol. 77, no. 1, pp. 139–141, 2000.

[24] J. Bin Yun *et al.*, “Random and localized resistive switching observation in Pt/NiO/Pt,” *Phys. Status Solidi - Rapid Res. Lett.*, vol. 1, no. 6, pp. 280–282, 2007.

[25] S. Seo *et al.*, “Reproducible resistance switching in polycrystalline NiO films,” *Appl. Phys. Lett.*, vol. 85, no. 23, pp. 5655–5657, 2004.

[26] D.-H. Kwon *et al.*, “Atomic structure of conducting nanofilaments in TiO2 resistive switching memory.,” *Nat. Nanotechnol.*, vol. 5, no. 2, pp. 148–53, 2010.

[27] B. J. Choi *et al.*, “Resistive switching mechanism of TiO2 thin films grown by atomic-layer deposition,” *J. Appl. Phys.*, vol. 98, no. 3, p. 033715, 2005.

[28] C. Rohde, B. J. Choi, D. S. Jeong, S. Choi, J. S. Zhao, and C. S. Hwang, “Identification of a determining parameter for resistive switching of TiO2 thin films,” *Appl. Phys. Lett.*, vol. 86, no. 26, p. 262907, 2005.

[29] K. L. Lin, T. H. Hou, J. Shieh, J. H. Lin, C. T. Chou, and Y. J. Lee, “Electrode dependence of filament formation in HfO2 resistive-switching memory,” *J. Appl. Phys.*, vol. 109, no. 8, 2011.

[30] Y. Y. Chen *et al.*, “Insights into Ni-filament formation in unipolar-switching Ni/HfO2/TiN resistive random access memory device,” *Appl. Phys. Lett.*, vol. 100, no. 11, pp. 1–5, 2012.

[31] F. Kurnia, Hadiyawarman, C. U. Jung, R. Jung, and C. Liu, “Composition dependence of unipolar resistance switching in TaOx thin films,” *Phys. Status Solidi - Rapid Res. Lett.*, vol. 5, no. 7, pp. 253–255, 2011.

[32] D. L. Xu, Y. Xiong, M. H. Tang, B. W. Zeng, Y. G. Xiao, and Z. P. Wang, “Reversible alternation between bipolar and unipolar resistive switching in La-SrTiO3 thin films,” *Chinese Phys. B*, vol. 22, no. 11, 2013.

[33] L. Goux *et al.*, “On the bipolar resistive-switching characteristics of Al2O3- and HfO2-based memory cells operated in the soft-breakdown regime,” *J. Appl. Phys.*, vol. 116, no. 13, pp. 3–11, 2014.

[34] J. J. Yang, M. D. Pickett, X. Li, D. A. A. Ohlberg, D. R. Stewart, and R. S. Williams, “Memristive switching mechanism for metal/oxide/metal nanodevices,” *Nat. Nanotechnol.*, vol. 3, no. 7, pp. 429–433, 2008.

[35] J. Joshua Yang *et al.*, “The mechanism of electroforming of metal oxide memristive switches,” *Nanotechnology*, vol. 20, no. 21, 2009.

[36] Y. M. Lu, M. Noman, W. Chen, P. A. Salvador, J. A. Bain, and M. Skowronski, “Elimination of high transient currents and electrode damage during electroformation of TiO2-based resistive switching devices,” *J. Phys. D. Appl. Phys.*, vol. 45, no. 39, 2012.

[37] M. H. Lee *et al.*, “Study on the electrical conduction mechanism of bipolar resistive switching TiO2 thin films using impedance spectroscopy,” *Appl. Phys. Lett.*, vol. 96, no. 15, 2010.

[38] S. Yu, X. Guan, and H. S. P. Wong, "Conduction mechanism of TiN/HfOx/Pt resistive switching memory: A trap-assisted-tunneling model," *Appl. Phys. Lett.*, vol. 99, no. 6, pp. 16–19, 2011.

[39] R. Fang, W. Chen, L. Gao, W. Yu, and S. Yu, "Low-Temperature Characteristics of HfOx-Based Resistive Random Access Memory," *IEEE Electron Device Lett.*, vol. 36, no. 6, pp. 567–569, 2015.

[40] L. Goux *et al.*, "Evidences of oxygen-mediated resistive-switching mechanism in TiN\HfO2\Pt cells," *Appl. Phys. Lett.*, vol. 97, no. 24, pp. 2–5, 2010.

[41] H. Y. Lee *et al.*, "Low power and high speed bipolar switching with a thin reactive ti buffer layer in robust HfO2 based RRAM," *Tech. Dig. - Int. Electron Devices Meet. IEDM*, pp. 3–6, 2008.

[42] D. S. Lee, Y. H. Sung, I. G. Lee, J. G. Kim, H. Sohn, and D. H. Ko, "Enhanced bipolar resistive switching of HfO2 with a Ti interlayer," *Appl. Phys. A Mater. Sci. Process.*, vol. 102, no. 4, pp. 997–1001, 2011.

[43] T. J. Dai, L. X. Qian, Y. X. Ren, and X. Z. Liu, "MoO3-x-based Bipolar Switching ReRAM Fabricated by Atomic Layer Deposition," in *International Conference on Electron Devices and Solid-State Circuits (EDSSC)*, 2017.

[44] M. J. Lee *et al.*, "A fast, high-endurance and scalable non-volatile memory device made from asymmetric Ta2O5-x/TaO2-x bilayer structures," *Nat. Mater.*, vol. 10, no. 8, pp. 625–630, 2011.

[45] Z. Wei *et al.*, "Highly reliable TaOx ReRAM and direct evidence of redox reaction mechanism," *Tech. Dig. - Int. Electron Devices Meet. IEDM*, pp. 1–4, 2008.

[46] J. J. Yang *et al.*, "High switching endurance in TaOx memristive devices," *Appl. Phys. Lett.*, vol. 97, no. 23, pp. 6–9, 2010.

[47] F. Messerschmitt, M. Kubicek, S. Schweiger, and J. L. M. Rupp, "Memristor kinetics and diffusion characteristics for mixed anionic-electronic SrTiO3-δ bits: The memristor-based cottrell analysis connecting material to device performance," *Adv. Funct. Mater.*, vol. 24, no. 47, pp. 7448–7460, 2014.

[48] K. Szot, W. Speier, G. Bihlmayer, and R. Waser, "Switching the electrical resistance of individual dislocations in single-crystalline SrTiO3," *Nat. Mater.*, vol. 5, no. 4, pp. 312–320, 2006.

[49] R. J. Kamaladasa *et al.*, "Dislocation impact on resistive switching in single-crystal SrTiO3," *J. Appl. Phys.*, vol. 113, no. 23, 2013.

[50] M. N. Kozicki and H. J. Barnaby, "Conductive bridging random access memory - Materials, devices and applications," *Semicond. Sci. Technol.*, vol. 31, no. 11, 2016.

[51] C. Schindler, M. Meier, R. Waser, and M. N. Kozicki, "Resistive switching in Ag-Ge-Se with extremely low write currents," vol. 00, no. c, pp. 82–85, 2015.

[52] M. Kund *et al.*, "Conductive bridging RAM (CBRAM): an emerging non-volatile memory technology scalable to sub 20nm," vol. 00, no. 1, pp. 754–757, 2006.

[53] M. N. Kozicki, C. Gopalan, M. Balakrishnan, M. Park, and M. Mitkova, "Nonvolatile memory based on solid electrolytes," vol. 00, no. C, pp. 10–17, 2005.

[54] M. Mitkova and M. N. Kozicki, "Silver incorporation in Ge-Se glasses used in programmable metallization cell devices," *J. Non. Cryst. Solids*, vol. 299–302, no. PART 2, pp. 1023–1027, 2002.

[55] N. E. Gilbert and M. N. Kozicki, "An embeddable multilevel-cell solid electrolyte memory array," *IEEE J. Solid-State Circuits*, vol. 42, no. 6, pp. 1383–1391, 2007.

[56] M. N. Kozicki, M. Park, and M. Mitkova, "Nanoscale memory elements based on solid-state electrolytes," *IEEE Trans. Nanotechnol.*, vol. 4, no. 3, pp. 331–338, 2005.

[57] M. N. Kozicki and M. Mitkova, "Mass transport in chalcogenide electrolyte films - materials and applications," *J. Non. Cryst. Solids*, vol. 352, no. 6-7 SPEC. ISS., pp. 567–577, 2006.

[58] M. N. Kozicki, M. Mitkova, M. Park, M. Balakrishnan, and C. Gopalan, "Information storage using nanoscale electrodeposition of metal in solid electrolytes," *Superlattices Microstruct.*, vol. 34, no. 3–6, pp. 459–465, 2003.

[59] W. Chen *et al.*, "Total-Ionizing-Dose Effects on Resistance Stability of Programmable Metallization Cell Based Memory and Selectors," *IEEE Trans. Nucl. Sci.*, vol. 64, no. 1, pp. 269–276, 2017.

[60] D. Kamalanathan, U. Russo, D. Ielmini, and M. N. Kozicki, "Voltage-driven on-off transition and tradeoff with program and erase current in Programmable Metallization Cell (PMC) memory," *IEEE Electron Device Lett.*, vol. 30, no. 5, pp. 553–555, 2009.

[61] U. Russo, D. Kamalanathan, D. Ielmini, A. L. Lacaita, and M. N. Kozicki, "Study of multilevel programming in Programmable Metallization Cell (PMC) memory," *IEEE Trans. Electron Devices*, vol. 56, no. 5, pp. 1040–1047, 2009.

[62] C. Gopalan *et al.*, “Demonstration of Conductive Bridging Random Access Memory (CBRAM) in logic CMOS process,” *Solid. State. Electron.*, vol. 58, no. 1, pp. 54–61, 2011.

[63] R. Symanczyk, R. Bruchhaus, R. Dittrich, and M. Kund, “Investigation of the reliability behavior of conductive-bridging memory cells,” *IEEE Electron Device Lett.*, vol. 30, no. 8, pp. 876–878, 2009.

[64] R. Bruchhaus, M. Honal, R. Symanczyk, and M. Kund, “Selection of Optimized Materials for CBRAM Based on HT-XRD and Electrical Test Results,” *J. Electrochem. Soc.*, vol. 156, no. 9, p. H729, 2009.

[65] M. Balakrishnan, M. N. Kozicki, C. Gopalan, and M. Mitkova, “Germanium sulfide-based solid electrolytes for non-volatile memory,” *Device Res. Conf. - Conf. Dig. DRC*, vol. 2005, pp. 47–48, 2005.

[66] J. Orava *et al.*, “Preferred location for conducting filament formation in thin-film nano-ionic electrolyte: study of microstructure by atom-probe tomography,” *J. Mater. Sci. Mater. Electron.*, vol. 28, no. 9, pp. 6846–6851, 2017.

[67] S. Puthen Thermadam, S. K. Bhagat, T. L. Alford, Y. Sakaguchi, M. N. Kozicki, and M. Mitkova, “Influence of Cu diffusion conditions on the switching of Cu-SiO2-based resistive memory devices,” *Thin Solid Films*, vol. 518, no. 12, pp. 3293–3298, 2010.

[68] S. Tappertzhofen, S. Menzel, I. Valov, and R. Waser, “Redox processes in silicon dioxide thin films using copper microelectrodes,” *Appl. Phys. Lett.*, vol. 99, no. 20, pp. 2011–2014, 2011.

[69] W. Chen, H. J. Barnaby, and M. N. Kozicki, “Impedance Spectroscopy of Programmable Metallization Cells With a Thin SiO2 Switching Layer,” *IEEE Electron Device Lett.*, vol. 37, no. 5, pp. 576–579, 2016.

[70] I. Valov and T. Tsuruoka, “Effects of moisture and redox reactions in VCM and ECM resistive switching memories,” *J. Phys. D. Appl. Phys.*, vol. 51, no. 41, 2018.

[71] S. Tappertzhofen, H. Mündelein, I. Valov, and R. Waser, “Nanoionic transport and electrochemical reactions in resistively switching silicon dioxide,” *Nanoscale*, vol. 4, no. 10, pp. 3040–3043, 2012.

[72] C. Schindler, S. C. P. Thermadam, R. Waser, and M. N. Kozicki, “Bipolar and Unipolar Resistive Switching in Cu-Doped SiO2,” *IEEE Trans. Electron Devices*, vol. 54, no. 10, pp. 2762–2768, 2007.

[73] W. Chen *et al.*, “A CMOS-compatible electronic synapse device based on Cu/SiO2/W programmable metallization cells,” *Nanotechnology*, vol. 27, no. 25, 2016.

[74] C. Kügeler, R. Rosezin, E. Linn, R. Bruchhaus, and R. Waser, “Materials, technologies, and circuit concepts for nanocrossbar-based bipolar RRAM,” *Appl. Phys. A Mater. Sci. Process.*, vol. 102, no. 4, pp. 791–809, 2011.

[75] Y. T. Li *et al.*, “Investigation of resistive switching behaviours in WO3-based RRAM devices,” *Chinese Phys. B*, vol. 20, no. 1, 2011.

[76] M. N. Kozicki, C. Gopalan, M. Balakrishnan, and M. Mitkova, “A low-power nonvolatile switching element based on copper-tungsten oxide solid electrolyte,” *IEEE Trans. Nanotechnol.*, vol. 5, no. 5, pp. 535–544, 2006.

[77] Y. Li *et al.*, “Nonvolatile multilevel memory effect in Cu/WO3/Pt device structures,” *Phys. Status Solidi - Rapid Res. Lett.*, vol. 4, no. 5–6, pp. 124–126, 2010.

[78] C. Gopalan, M. N. Kozicki, S. Bhagat, S. C. Puthen Thermadam, T. L. Alford, and M. Mitkova, “Structure of copper-doped tungsten oxide films for solid-state memory,” *J. Non. Cryst. Solids*, vol. 353, no. 18–21, pp. 1844–1848, 2007.

[79] L. Goux *et al.*, “Field-driven ultrafast sub-ns programming in W\Al2O3\Ti\CuTe-based 1T1R CBRAM system,” *Dig. Tech. Pap. - Symp. VLSI Technol.*, pp. 69–70, 2012.

[80] A. Belmonte *et al.*, “90nm W\Al2O3\TiW\Cu 1T1R CBRAM cell showing low-power, fast and disturb-free operation,” *2013 5th IEEE Int. Mem. Work. IMW 2013*, pp. 26–29, 2013.

[81] A. Belmonte *et al.*, “A thermally stable and high-performance 90-nm Al2O3 \ Cu-based 1T1R CBRAM cell,” *IEEE Trans. Electron Devices*, vol. 60, no. 11, pp. 3690–3695, 2013.

[82] L. Goux *et al.*, “Influence of the Cu-Te composition and microstructure on the resistive switching of Cu-Te/Al2O3/Si cells,” *Appl. Phys. Lett.*, vol. 99, no. 5, pp. 3–6, 2011.

[83] K. Aratani *et al.*, “A Novel Resistance Memory with High Scalability and Nanosecond Switching,” in *IEEE Electron Devices Meeting*, 2007, pp. 783–786.

[84] T. Tsuruoka, K. Terabe, T. Hasegawa, and M. Aono, “Temperature effects on the switching kinetics of a Cu-Ta2O5-based atomic switch,” *Nanotechnology*, vol. 22, no. 37, 2011.

[85] T. Sakamoto, K. Lister, N. Banno, T. Hasegawa, K. Terabe, and M. Aono, "Electronic transport in Ta2O5 resistive switch," *Appl. Phys. Lett.*, vol. 91, no. 9, 2007.

[86] T. Sakamoto *et al.*, "A Ta2O5 solid-electrolyte switch with improved reliability," in *Digest of Technical Papers - Symposium on VLSI Technology*, 2007, vol. 3032, no. 2003, pp. 38–39.

[87] Y. Tsuji, T. Sakamoto, N. Banno, H. Hada, and M. Aono, "Off-state and turn-on characteristics of solid electrolyte switch," *Appl. Phys. Lett.*, vol. 96, no. 2, pp. 1–4, 2010.

[88] K. H. Kim *et al.*, "A functional hybrid memristor crossbar-array/CMOS system for data storage and neuromorphic applications," *Nano Lett.*, vol. 12, no. 1, pp. 389–395, 2012.

[89] Y. Yang, P. Gao, S. Gaba, T. Chang, X. Pan, and W. Lu, "Observation of conducting filament growth in nanoscale resistive memories," *Nat. Commun.*, vol. 3, pp. 732–738, 2012.

[90] I. Valov, R. Waser, J. R. Jameson, and M. N. Kozicki, "Electrochemical metallization memories - Fundamentals, applications, prospects," *Nanotechnology*, vol. 22, no. 28, 2011.

[91] U. Celano *et al.*, "Three-dimensional observation of the conductive filament in nanoscaled resistive memory devices," *Nano Lett.*, vol. 14, no. 5, pp. 2401–2406, 2014.

[92] Q. Liu *et al.*, "Real-time observation on dynamic growth/dissolution of conductive filaments in oxide-electrolyte-based ReRAM," *Adv. Mater.*, vol. 24, pp. 1844–1849, 2012.

[93] W. Chen *et al.*, "A Study of Gamma-Ray Exposure of Cu-SiO2 Programmable Metallization Cells," *IEEE Trans. Nucl. Sci.*, vol. 62, no. 6, pp. 2404–2411, 2015.

[94] R. Waser, R. Dittmann, C. Staikov, and K. Szot, "Redox-based resistive switching memories nanoionic mechanisms, prospects, and challenges," *Adv. Mater.*, vol. 21, no. 25–26, pp. 2632–2663, 2009.

[95] J. A. Nessel, R. Q. Lee, C. H. Mueller, M. N. Kozicki, M. Ren, and J. Morse, "A novel nanoionics-based switch for microwave applications," *IEEE MTT-S Int. Microw. Symp. Dig.*, pp. 1050–1054, 2008.

[96] A. Emboras *et al.*, "Nanoscale plasmonic memristor with optical readout functionality," *Nano Lett.*, vol. 13, no. 12, pp. 6151–6155, 2013.

[97] U. Koch, C. Hoessbacher, A. Emboras, and J. Leuthold, “Optical memristive switches,” *J. Electroceramics*, vol. 39, no. 1–4, pp. 239–250, 2017.

[98] M. N. Kozicki, P. Maroufkhani, and M. Mitkova, “Valving in microchannels via electrodeposition on solid electrolytes,” in *2005 NSTI Nanotechnology Conference and Trade Show - NSTI Nanotech 2005 Technical Proceedings*, 2005, pp. 716–719.

[99] S. Enderling *et al.*, “Integration of a novel electrochemical tuning scheme with mems surface micromachined resonators,” pp. 159–162, 2005.

[100] S. S. Je, J. Kim, J. C. Harrison, M. N. Kozicki, and J. Chae, “In situ tuning of omnidirectional microelectromechanical-systems microphones to improve performance fit in hearing aids,” *Appl. Phys. Lett.*, vol. 93, no. 12, pp. 1–4, 2008.

[101] Y. Gonzalez-Velo, M. N. Kozicki, D. Chang, A. Odishvili, and E. Mikkola, “Timing Devices Based on the Growth of Metal Electrodeposits,” in *2020 GOMAC Conference*, 2020.

[102] M. N. Kozicki, “Timing Device Using Electrodeposit Growth,” US Patent 10,558,172, 2020.

[103] M. N. Kozicki, “Dendritic structures and tags as physical unclonable function for anti-counterfeiting,” European Patent Application 2998949, 2016.

[104] C.-Y. Liu, K.-C. Chiang, and C.-H. Lai, “Resistive memory properties of an electrochemical SiO2-based device without an active electrode,” *J. Vac. Sci. Technol. A Vacuum, Surfaces, Film.*, vol. 34, no. 2, p. 02D102, 2016.

[105] M. Tada, T. Sakamoto, N. Banno, M. Aono, H. Hada, and N. Kasai, “Nonvolatile crossbar switch using TiOx/TaSiOy Solid electrolyte,” *IEEE Trans. Electron Devices*, vol. 57, no. 8, pp. 1987–1995, 2010.

[106] D. Varandani, B. Singh, B. R. Mehta, M. Singh, V. N. Singh, and D. Gupta, “Resistive switching mechanism in delafossite-transition metal oxide (CuInO2-CuO) bilayer structure,” *J. Appl. Phys.*, vol. 107, no. 10, 2010.

[107] S. Z. Rahaman *et al.*, “Impact of TaOx nanolayer at the GeSex/W interface on resistive switching memory performance and investigation of Cu nanofilament,” *J. Appl. Phys.*, vol. 111, no. 6, 2012.

[108] S. Z. Rahaman and S. Maikap, “Improved resistive switching memory characteristics using novel bi-layered Ge0.2Se0.8/Ta2O5 solid-electrolytes,” in *2010 IEEE International Memory Workshop, IMW 2010*, 2010, pp. 1–4.

[109] J. Yi *et al.*, “Research on switching property of an oxide/copper sulfide hybrid memory,” in *Proceedings - 2008 9th Annual Non-Volatile Memory Technology Symposium, NVMTS 2008*, 2008, pp. 5–8.

[110] R. Soni, M. Meier, A. Rüdiger, B. Holländer, C. Kügeler, and R. Waser, “Integration of ‘GexSe1-x’ in crossbar arrays for non-volatile memory applications,” *Microelectron. Eng.*, vol. 86, no. 4–6, pp. 1054–1056, 2009.

[111] J. Guy *et al.*, “Investigation of the physical mechanisms governing data-retention in down to 10nm nano-trench Al2O3/CuTeGe conductive bridge RAM (CBRAM),” *Tech. Dig. - Int. Electron Devices Meet. IEDM*, pp. 742–745, 2013.

[112] J. Yoon *et al.*, “Excellent switching uniformity of Cu-doped MoOxGdOx bilayer for nonvolatile memory applications,” *IEEE Electron Device Lett.*, vol. 30, no. 5, pp. 457–459, 2009.

[113] G. E. Bacon, *X-Ray and Neutron Diffraction : The Commonwealth and International Library: Selected Readings in Physics*. Kent: Elsevier Science & Technology, 1966.

[114] W. L. Bragg, “The Diffraction of Short Electromagnetic Waves by a Crystal,” *Proc. Camb. Philol. Soc.*, vol. 17, pp. 43–57, 1913.

[115] B. B. He, *Two-dimensional X-ray diffraction*. Hoboken, NJ: Wiley, 2009.

[116] D. G. Lamas, M. D. O. Neto, G. Kellermann, and A. F. Craievich, *Scattering by Nanomaterials*. Elsevier Inc., 2017.

[117] M. Sardela, *Practical materials characterization*. 2014.

[118] R. Escobar Galindo, R. Gago, D. Duday, and C. Palacio, “Towards nanometric resolution in multilayer depth profiling: A comparative study of RBS, SIMS, XPS and GDOES,” *Anal. Bioanal. Chem.*, vol. 396, no. 8, pp. 2725–2740, 2010.

[119] J. F. Watts, *An introduction to surface analysis by XPS and AES*. Chichester, England ; New York: J. Wiley, 2003.

[120] L. S. Chang, Y. C. Lin, C. Y. Su, H. C. Wu, and J. P. Pan, “Effect of C60 ion sputtering on the compositional depth profiling in XPS for Li(Ni,Co,Mn)O2 electrodes,” *Appl. Surf. Sci.*, vol. 258, no. 3, pp. 1279–1281, 2011.

[121] D. C. Joy, “The theory and practice of high-resolution scanning electron microscopy,” *Ultramicroscopy*, vol. 37, no. 1–4, pp. 216–233, 1991.

[122] A. Adriaens and M. G. Dowsett, “Chapter 3 Electron microscopy and its role in cultural heritage studies,” *Compr. Anal. Chem.*, vol. 42, pp. 73–128, 2004.

[123] Weirich, Lábár, and Zou, *Electron Crystallography Novel Approaches for Structure Determination of Nanosized Materials*, 1st ed. 2006.. Dordrecht ; [Great Britain]: Springer, 2006.

[124] H. Riegler, “A user’s guide to ellipsometry. By Harland G. Tompkins, Academic Press, New York 1993, 260 pp. hardback, ISBN 0-12-603050-0,” *Adv. Mater.*, 1993.

[125] R. M. A. Azzam, *Ellipsometry and polarized light*. Amsterdam ; New York : New York: North-Holland Pub. Co. ; Sole distributors for the U.S.A. and Canada, Elsevier North-Holland, 1977.

[126] R. K. Sampson and H. Z. Massoud, “Resolution of Silicon Wafer Temperature Measurement by in Situ Ellipsometry in a Rapid Thermal Processor,” *J. Electrochem. Soc.*, vol. 140, no. 9, pp. 2673–2678, 1993.

[127] D. E. Aspnes, “New developments in spectroellipsometry: the challenge of surfaces,” *Thin Solid Films*, vol. 233, no. 1–2, pp. 1–8, 1993.

[128] D. K. Schroder, *Semiconductor Material and Device Characterization: Third Edition*. 2005.

[129] G. Binnig, C. F. Quate, and C. Gerber, “Atomic Force Microscope,” *Phys. Rev. Lett.*, vol. 56, no. 9, pp. 930–933, 1986.

[130] D. Johnson, N. Hilal, and W. R. Bowen, *Basic principles of atomic force microscopy*. Elsevier Ltd, 2009.

[131] Y. F. Chang *et al.*, “Intrinsic SiOx-based unipolar resistive switching memory. I. Oxide stoichiometry effects on reversible switching and program window optimization,” *J. Appl. Phys.*, vol. 116, no. 4, 2014.

[132] Y. T. Chen *et al.*, “Tristate operation in resistive switching of SiO2 thin films,” *IEEE Electron Device Lett.*, vol. 33, no. 12, pp. 1702–1704, 2012.

[133] D. Y. Cho, S. Tappertzhofen, R. Waser, and I. Valov, “Bond nature of active metal ions in SiO2-based electrochemical metallization memory cells,” *Nanoscale*, vol. 5, no. 5, pp. 1781–1784, 2013.

[134] S. P. Murarka, “Multilevel interconnections for ULSI and GSI era,” *Mater. Sci. Eng. R Reports*, vol. 19, no. 3–4, pp. 87–151, 1997.

[135] Y. Yang *et al.*, “Electrochemical dynamics of nanoscale metallic inclusions in dielectrics,” *Nat. Commun.*, vol. 5, no. May, pp. 1–9, 2014.

[136] Z. Wang *et al.*, “Electrochemical metallization switching with a platinum group metal in different oxides,” *Nanoscale*, vol. 8, no. 29, pp. 14023–14030, 2016.

[137] S. Tappertzhofen, R. Waser, and I. Valov, “Impact of the Counter-Electrode Material on Redox Processes in Resistive Switching Memories,” *ChemElectroChem*, vol. 1, no. 8, pp. 1287–1292, 2014.

[138] I. Valov, “Redox-based resistive switching memories (ReRAMs): Electrochemical systems at the atomic scale,” *ChemElectroChem*, vol. 1, no. 1, pp. 26–36, 2014.

[139] I. Valov and G. Staikov, “Nucleation and growth phenomena in nanosized electrochemical systems for resistive switching memories,” *J. Solid State Electrochem.*, vol. 17, no. 2, pp. 365–371, 2013.

[140] Y. Fan, S. King, J. Bielefeld, and M. Orlowski, “Characterization of porous BEOL dielectrics for resistive switching,” *ECS Trans.*, vol. 72, no. 2, pp. 35–50, 2016.

[141] X. Zhang, X. Gu, and S. Xiao, “Modification of SiO2 thickness distribution through evaporation,” *Thin Solid Films*, vol. 642, no. July, pp. 31–35, 2017.

[142] M. S. Munde *et al.*, “Intrinsic Resistance Switching in Amorphous Silicon Suboxides: The Role of Columnar Microstructure,” *Sci. Rep.*, vol. 7, no. 1, pp. 1–8, 2017.

[143] J. A. Thornton, “The microstructure of sputter-deposited coatings,” *J. Vac. Sci. Technol. A Vacuum, Surfaces, Film.*, vol. 4, no. 6, pp. 3059–3065, 1986.

[144] O. O. Abegunde, E. T. Akinlabi, O. P. Oladijo, S. Akinlabi, and A. U. Ude, “Overview of thin film deposition techniques,” *AIMS Mater. Sci.*, vol. 6, no. 2, pp. 174–199, 2019.

[145] A. Mehonic *et al.*, “Silicon Oxide (SiOx): A Promising Material for Resistance Switching?,” *Adv. Mater.*, vol. 30, no. 43, pp. 1–21, 2018.

[146] Y. Fan, R. Ali, S. King, J. Bielefeld, and M. Orlowski, “Decoupling of ion diffusivity and electromobility in porous dielectrics,” *ECS Trans.*, vol. 72, no. 2, pp. 233–240, 2016.

[147] R. Ali, Y. Fan, S. King, and M. Orlowski, “Modeling and simulation of Cu diffusion and drift in porous CMOS backend dielectrics,” *APL Mater.*, vol. 6, p. 066101, 2018.

[148] T. Tsuruoka, K. Terabe, T. Hasegawa, I. Valov, R. Waser, and M. Aono, "Effects of moisture on the switching characteristics of oxide-based, gapless-type atomic switches," *Adv. Funct. Mater.*, vol. 22, no. 1, pp. 70–77, 2012.

[149] S. Tappertzhofen, I. Valov, T. Tsuruoka, T. Hasegawa, R. Waser, and M. Aono, "Generic relevance of counter charges for cation-based nanoscale resistive switching memories," *ACS Nano*, vol. 7, no. 7, pp. 6396–6402, 2013.

[150] W. Chen, S. Tappertzhofen, H. J. Barnaby, and M. N. Kozicki, "SiO2 based conductive bridging random access memory," *J. Electroceramics*, vol. 39, no. 1–4, pp. 109–131, 2017.

[151] M. Lübben, S. Menzel, S. G. Park, M. Yang, R. Waser, and I. Valov, "SET kinetics of electrochemical metallization cells: Influence of counter-electrodes in SiO2/Ag based systems," *Nanotechnology*, vol. 28, no. 13, 2017.

[152] B. W. Fowler *et al.*, "Electroforming and resistive switching in silicon dioxide resistive memory devices," *RSC Adv.*, vol. 5, no. 27, pp. 21215–21236, 2015.

[153] Z. A. Weinberg, D. R. Young, J. A. Calise, S. A. Cohen, J. C. Deluca, and V. R. Deline, "Reduction of electron and hole trapping in SiO2 by rapid thermal annealing," *Appl. Phys. Lett.*, vol. 45, no. 11, pp. 1204–1206, 1984.

[154] C. Schindler, "Resistive switching in electrochemical metallization memory cells," 2009.

[155] C. He *et al.*, "Tunable Electroluminescence in Planar Graphene/SiO2 Memristors," *Adv. Mater.*, vol. 25, no. 39, pp. 5593–5598, 2013.

[156] J. Yao, L. Zhong, D. Natelson, and J. M. Tour, "In situ imaging of the conducting filament in a silicon oxide resistive switch," *Sci. Rep.*, vol. 2, pp. 1–5, 2012.

[157] J. Yao, Z. Sun, L. Zhong, D. Natelson, and J. M. Tour, "Resistive switches and memories from silicon oxide," *Nano Lett.*, vol. 10, no. 10, pp. 4105–4110, 2010.

[158] Y. Wang *et al.*, "Effect of hydrogen/deuterium incorporation on electroforming voltage of SiOx resistive random access memory," *Appl. Phys. Lett.*, vol. 101, no. 18, 2012.

[159] C. Schindler, G. Staikov, and R. Waser, "Electrode kinetics of Cu-SiO2-based resistive switching cells: Overcoming the voltage-time dilemma of electrochemical metallization memories," *Appl. Phys. Lett.*, vol. 94, no. 7, pp. 92–95, 2009.

[160] M. R. Baklanov, C. Adelmann, L. Zhao, and S. De Gendt, "Advanced Interconnects: Materials, Processing, and Reliability," *ECS J. Solid State Sci. Technol.*, vol. 4, no. 1, pp. Y1–Y4, 2015.

[161] K. Han and M. Tao, "Electrochemically deposited p-n homojunction cuprous oxide solar cells," *Sol. Energy Mater. Sol. Cells*, vol. 93, no. 1, pp. 153–157, 2009.

[162] S. J. Pearton, W. H. Heo, M. Ivill, D. P. Norton, and T. Steiner, "Dilute magnetic semiconducting oxides," *Semicond. Sci. Technol.*, vol. 19, no. 10, pp. R59–R74, 2004.

[163] J. Ramírez-Ortiz *et al.*, "A catalytic application of Cu2O and CuO films deposited over fiberglass," *Appl. Surf. Sci.*, vol. 174, no. 3–4, pp. 177–184, 2001.

[164] F. P. Koffyberg and F. A. Benko, "A photoelectrochemical determination of the position of the conduction and valence band edges of p-type CuO," *J. Appl. Phys.*, vol. 53, no. 2, pp. 1173–1177, 1982.

[165] X. G. Zheng, C. N. Xu, E. Tanaka, Y. Tomokiyo, M. Suzuki, and E. S. Otabe, "Charge–spin–orbital coupling in CuO," *Phys. C Supercond.*, vol. 357–360, pp. 181–185, 2001.

[166] J. Ghijsen *et al.*, "Electronic structure of Cu2O and CuO," *Phys. Rev. B*, vol. 38, no. 16, pp. 11322–11330, 1988.

[167] A. H. Jayatissa, K. Guo, and A. C. Jayasuriya, "Fabrication of cuprous and cupric oxide thin films by heat treatment," *Appl. Surf. Sci.*, vol. 255, no. 23, pp. 9474–9479, 2009.

[168] S. Suzuki, Y. Ishikawa, M. Isshiki, and Y. Waseda, "Native Oxide Layers Formed on the Surface of Ultra High-Purity Iron and Copper Investigated by Angle Resolved XPS," *Mater. Trans. JIM*, vol. 38, no. 11, pp. 1004–1009, 1997.

[169] D. R. et al. Lide, "CRC Handbook of Chemistry and Physics, Internet Version." p. 2661, 2005.

[170] D. L. Cocke *et al.*, "The low-temperature thermal oxidation of copper, Cu3O2, and its influence on past and future studies," *Vacuum*, vol. 79, no. 1–2, pp. 71–83, 2005.

[171] L. Debbichi, M. C. Marco De Lucas, and P. Krüger, "Electronic structure, lattice dynamics and thermodynamic stability of paramelaconite Cu4O3," *Mater. Chem. Phys.*, vol. 148, no. 1–2, pp. 293–298, 2014.

[172] J. Li, J. W. Mayer, and E. G. Colgan, “Oxidation and protection in copper and copper alloy thin films,” *J. Appl. Phys.*, vol. 70, no. 5, pp. 2820–2827, 1991.

[173] G. Valensi, “Nouvelles applications de la théorie de l’oxydation des métaux possédant deux oxydes,” *Rev. Métallurgie*, 1948.

[174] Y. S. Gong, C. Lee, and C. K. Yang, “Atomic force microscopy and Raman spectroscopy studies on the oxidation of Cu thin films,” *J. Appl. Phys.*, vol. 77, no. 10, pp. 5422–5425, 1995.

[175] V. Figueiredo *et al.*, “Effect of post-annealing on the properties of copper oxide thin films obtained from the oxidation of evaporated metallic copper,” *Appl. Surf. Sci.*, vol. 254, no. 13, pp. 3949–3954, 2008.

[176] K. Fujita, D. Ando, M. Uchikoshi, K. Mimura, and M. Isshiki, “New model for low-temperature oxidation of copper single crystal,” *Appl. Surf. Sci.*, vol. 276, pp. 347–358, 2013.

[177] B. Maack and N. Nilius, “Oxidation of polycrystalline copper films – Pressure and temperature dependence,” *Thin Solid Films*, vol. 651, no. December 2017, pp. 24–30, 2018.

[178] L. De Los Santos Valladares *et al.*, “Crystallization and electrical resistivity of Cu2O and CuO obtained by thermal oxidation of Cu thin films on SiO2/Si substrates,” *Thin Solid Films*, vol. 520, no. 20, pp. 6368–6374, 2012.

[179] W. Gao, H. Gong, J. He, A. Thomas, L. Chan, and S. Li, “Oxidation behaviour of Cu thin films on Si wafer at 175-400°C,” *Mater. Lett.*, vol. 51, no. 1, pp. 78–84, 2001.

[180] C. Zhong, Y. M. Jiang, Y. F. Luo, B. Deng, L. Zhang, and J. Li, “Kinetics characterization of the oxidation of Cu thin films at low temperature by using sheet resistance measurement,” *Appl. Phys. A Mater. Sci. Process.*, vol. 90, no. 2, pp. 263–266, 2008.

[181] G. K. P. Ramanandan, G. Ramakrishnan, and P. C. M. Planken, “Oxidation kinetics of nanoscale copper films studied by terahertz transmission spectroscopy,” *J. Appl. Phys.*, vol. 111, no. 12, 2012.

[182] N. Cabrera and N. F. Mott, “Theory of the oxidation of metals,” *Reports Prog. Phys.*, vol. 12, no. 1, pp. 163–184, 1949.

[183] A. Manara, V. Sirtori, and L. Mammarella, “Optical ellipsometry and electron spectroscopy studies of copper oxidation related to copper on printed circuit boards,” *Surf. Interface Anal.*, 1992.

[184] S. K. Roy and S. C. Sircar, "A critical appraisal of the logarithmic rate law in thin-film formation during oxidation of copper and its alloys," *Oxid. Met.*, 1981.

[185] F. W. Young, J. V Cathcart, and A. T. Gwathmey, "The rates of oxidation of several faces of a single crystal of copper as determined with elliptically polarized light," *Acta Metall.*, vol. 4, no. 2, pp. 145–152, 2003.

[186] M. O'Reilly *et al.*, "Investigation of the oxidation behaviour of thin film and bulk copper," *Appl. Surf. Sci.*, vol. 91, no. 1–4, pp. 152–156, 1995.

[187] A. Yabuki and S. Tanaka, "Oxidation behavior of copper nanoparticles at low temperature," *Mater. Res. Bull.*, vol. 46, no. 12, pp. 2323–2327, 2011.

[188] H. Derin and K. Kantarli, "Optical characterization of thin thermal oxide films on copper by ellipsometry," *Appl. Phys. A Mater. Sci. Process.*, vol. 75, no. 3, pp. 391–395, 2002.

[189] T. N. Rhodin, "Low Temperature Oxidation of Copper. I. Physical Mechanism," *J. Am. Chem. Soc.*, vol. 72, no. 11, pp. 5102–5106, 1950.

[190] J. Liang, N. Kishi, T. Soga, T. Jimbo, and M. Ahmed, "Thin cuprous oxide films prepared by thermal oxidation of copper foils with water vapor," *Thin Solid Films*, vol. 520, no. 7, pp. 2679–2682, 2012.

[191] J. Iijima, J. W. Lim, S. H. Hong, S. Suzuki, K. Mimura, and M. Isshiki, "Native oxidation of ultra high purity Cu bulk and thin films," *Appl. Surf. Sci.*, vol. 253, no. 5, pp. 2825–2829, 2006.

[192] Y. Zhu, K. Mimura, and M. Isshiki, "A study of the initial oxidation of copper in 0.1 MPa oxygen and the effect of purity by metallographic methods," *Corros. Sci.*, vol. 46, no. 10, pp. 2445–2454, 2004.

[193] C. Gattinoni and A. Michaelides, "Atomistic details of oxide surfaces and surface oxidation: the example of copper and its oxides," *Surf. Sci. Rep.*, vol. 70, no. 3, pp. 424–447, 2015.

[194] P. K. Ooi, S. S. Ng, M. J. Abdullah, H. Abu Hassan, and Z. Hassan, "Effects of oxygen percentage on the growth of copper oxide thin films by reactive radio frequency sputtering," *Mater. Chem. Phys.*, vol. 140, no. 1, pp. 243–248, 2013.

[195] T. N. Rhodin, "Low Temperature Oxidation of Copper. II. Reaction Rate Anisotropy," *J. Am. Chem. Soc.*, vol. 73, no. 7, pp. 3143–3146, 1951.

[196] R. Haugsrud and P. Kofstad, “On the Oxygen Pressure Dependence of High Temperature Oxidation of Copper,” *Mater. Sci. Forum*, vol. 251–254, pp. 65–72, Oct. 1997.

[197] Y. Zhu, K. Mimura, J. W. Lim, M. Isshiki, and Q. Jiang, “Brief review of oxidation kinetics of copper at 350 °C to 1050 °C,” *Metall. Mater. Trans. A Phys. Metall. Mater. Sci.*, vol. 37, no. 4, pp. 1231–1237, 2006.

[198] S. Chevalier, “Mechanisms and kinetics of oxidation,” *Shreir’s Corros.*, pp. 132–152, 2010.

[199] H. K. Liou, J. S. Huang, and K. N. Tu, “Oxidation of Cu and Cu3Ge thin films,” *J. Appl. Phys.*, vol. 77, no. 10, pp. 5443–5445, 1995.

[200] G. Valensi, “Theoretical and experimental investigations about conjugated formation of several layers in dry corrosion,” in *Pittsburgh International Conference on Surface Reactions*, 1948, pp. 156–165.

[201] Y. Zhu, K. Mimura, and M. Isshiki, “Oxidation Mechanism of Copper at 623-1073 K,” *Mater. Trans.*, vol. 43, no. 9, pp. 2173–2176, 2005.

[202] J. C. Yang, M. Yeadon, B. Kolasa, and J. M. Gibson, “Oxygen surface diffusion in three-dimensional Cu2O growth on Cu (001) thin films,” *Appl. Phys. Lett.*, vol. 70, no. 26, pp. 3522–3524, 1997.

[203] J. C. Yang, B. Kolasa, J. M. Gibson, and M. Yeadon, “Self-limiting oxidation of copper,” *Appl. Phys. Lett.*, vol. 73, no. 19, pp. 2841–2843, 1998.

[204] C. L. Huang, W. L. Weng, Y. S. Huang, and C. N. Liao, “Enhanced photolysis stability of Cu2O grown on Cu nanowires with nanoscale twin boundaries,” *Nanoscale*, vol. 11, no. 29, pp. 13709–13713, 2019.

[205] E. Kirkendall, L. Thomassen, and C. Uethegrove, “Rates of Diffusion of Copper and Zinc in Alpha Brass,” *Trans. Am. Inst. Min. Metall. Eng.*, 1939.

[206] C. E. Birchenall, “Kinetics of Formation of Porous or Partially Detached Scales,” *J. Electrochem. Soc.*, vol. 104, no. 6, p. 397, 1957.

[207] J. Liu, R. E. Saw, and Y. H. Kiang, “Calculation of effective penetration depth in X-ray diffraction for pharmaceutical solids,” *J. Pharm. Sci.*, vol. 99, no. 9, pp. 3807–3814, 2010.

[208] H. Bubert, E. Grallath, A. Quentmeier, M. Wielunski, and L. Borucki, “Comparative investigation on copper oxides by depth profiling using XPS, RBS and GDOES,” *Fresenius. J. Anal. Chem.*, vol. 353, no. 3–4, pp. 456–463, 1995.

[209] S. Bijani, R. Schrebler, E. A. Dalchiele, M. Gabás, L. Martínez, and J. R. Ramos-Barrado, “Study of the nucleation and growth mechanisms in the electrodeposition of micro- and nanostructured Cu2O thin films,” *J. Phys. Chem. C*, vol. 115, no. 43, pp. 21373–21382, 2011.

[210] D. Ozaslan, O. Erken, M. Gunes, and C. Gumus, “The effect of annealing temperature on the physical properties of Cu2O thin film deposited by SILAR method,” *Phys. B Condens. Matter*, vol. 580, no. June 2019, p. 411922, 2020.

[211] T. Ferreira and W. Rasband, *ImageJ User Guide User Guide ImageJ*, vol. 1.46r. 2012.

[212] C. G. Granqvist and R. A. Buhrman, “Size Distributions for Supported Metal Catalysts: Coalescence Growth versus Ostwald Ripening,” *J. Catal.*, vol. 42, pp. 477–479, 1976.

[213] N. F. Mott, “Oxidation of metals and the formation of protective films,” *Nature*, 1940.

[214] J. Bardeen, W. H. Brattain, and W. Shockley, “Investigation of oxidation of copper by use of radioactive Cu tracer,” *J. Chem. Phys.*, vol. 14, no. 12, pp. 714–721, 1946.

[215] J. D. McBrayer, “Diffusion of Metals in Silicon Dioxide,” *J. Electrochem. Soc.*, vol. 133, no. 6, p. 1242, 2006.

[216] E. R. Weber, “Transition metals in silicon,” *Appl. Phys. A Solids Surfaces*, 1983.

[217] C. S. Liu and L. J. Chen, “Catalytic oxidation of (001)Si in the presence of Cu 3 Si at room temperature,” *J. Appl. Phys.*, vol. 74, no. 5, pp. 3611–3613, 1993.

[218] Z. Y. Nuru, C. J. Arendse, S. Khamlich, L. Kotsedi, and M. Maaza, “A Tantalum diffusion barrier layer to improve the thermal stability of AlxOy/Pt/AlxOy multilayer solar absorber,” *Sol. Energy*, vol. 107, pp. 89–96, 2014.

[219] Q. Xie *et al.*, “Superior thermal stability of Ta/TaN bi-layer structure for copper metallization,” *Appl. Surf. Sci.*, vol. 253, no. 3, pp. 1666–1672, 2006.

[220] H. Kim, C. Detavenier, O. Van Der Straten, S. M. Rossnagel, A. J. Kellock, and D. G. Park, “Robust TaNx diffusion barrier for Cu-interconnect technology with subnanometer thickness by metal-organic plasma-enhanced atomic layer deposition,” *J. Appl. Phys.*, vol. 98, no. 1, 2005.

[221] J. Baumann, T. Werner, A. Ehrlich, M. Rennau, C. Kaufmann, and T. Gessner, "TiN diffusion barriers for copper metallization," *Microelectron. Eng.*, vol. 37/38, pp. 221–228, 1997.

[222] A. Lintanf-Salaün, A. Mantoux, E. Djurado, and E. Blanquet, "Atomic layer deposition of tantalum oxide thin films for their use as diffusion barriers in microelectronic devices," *Microelectron. Eng.*, vol. 87, no. 3, pp. 373–378, 2010.

[223] K. M. Chang, T. H. Yeh, I. C. Deng, and C. W. Shin, "Amorphouslike chemical vapor deposited tungsten diffusion barrier for copper metallization and effects of nitrogen addition," *J. Appl. Phys.*, vol. 82, no. 3, pp. 1469–1475, 1997.

[224] M. P. Nguyen, Y. Sutou, and J. Koike, "Diffusion barrier property of MnSixOy layer formed by chemical vapor deposition for Cu advanced interconnect application," *Thin Solid Films*, vol. 580, pp. 56–60, 2015.

[225] C. Byrne, B. Brennan, A. P. McCoy, J. Bogan, A. Brady, and G. Hughes, "In Situ XPS Chemical Analysis of MnSiO3 Copper Diffusion Barrier Layer Formation and Simultaneous Fabrication of Metal Oxide Semiconductor Electrical Test MOS Structures," *ACS Appl. Mater. Interfaces*, vol. 8, no. 4, pp. 2470–2477, 2016.

[226] C. Byrne *et al.*, "Chemical and electrical characterisation of the segregation of Al from a CuAl alloy (90%:10% wt) with thermal anneal," *Thin Solid Films*, vol. 599, pp. 59–63, 2016.

[227] C. Byrne *et al.*, "Physical, chemical and electrical characterisation of the diffusion of copper in silicon dioxide and prevention via a CuAl alloy barrier layer system," *Mater. Sci. Semicond. Process.*, vol. 63, no. November 2016, pp. 227–236, 2017.

[228] D. C. Perng, J. Bin Yeh, K. C. Hsu, and S. W. Tsai, "Self-forming AlOx layer as Cu diffusion barrier on porous low-k film," *Thin Solid Films*, vol. 518, no. 6, pp. 1648–1652, 2010.

[229] C. J. Liu and J. S. Chen, "High-temperature self-grown ZrO2 layer against Cu diffusion at Cu(2.5 at. % Zr)⁄SiO2 interface," *J. Vac. Sci. Technol. B Microelectron. Nanom. Struct.*, vol. 23, no. 1, p. 90, 2005.

[230] Y. L. Cheng, K. C. Kao, C. J. Huang, G. S. Chen, and J. S. Fang, "Atomic layer deposition HfO2 capping layer effect on porous low dielectric constant materials," *Appl. Surf. Sci.*, vol. 354, pp. 115–119, 2015.

[231] I. Fisher and M. Eizenberg, "Copper ion diffusion in porous and nonporous SiO2 - based dielectrics using bias thermal stress and thermal stress tests," *Thin Solid Films*, vol. 516, no. 12, pp. 4111–4121, 2008.

[232] O. Rodriguez, R. Saxena, W. Cho, J. L. Plawsky, and W. N. Gill, “Diffusion of copper in nanoporous dielectric films,” *Ind. Eng. Chem. Res.*, vol. 44, no. 5, pp. 1220–1225, 2005.

[233] G. Raghavan *et al.*, “Diffusion of copper through dielectric films under bias temperature stress,” *Thin Solid Films*, vol. 262, no. 1–2, pp. 168–176, 1995.

[234] K. S. Kim, Y. C. Joo, K. B. Kim, and J. Y. Kwon, “Extraction of Cu diffusivities in dielectric materials by numerical calculation and capacitance-voltage measurement,” *J. Appl. Phys.*, vol. 100, no. 6, pp. 1–6, 2006.

[235] B. G. Willis and D. V. Lang, “Oxidation mechanism of ionic transport of copper in SiO2 dielectrics,” *Thin Solid Films*, vol. 467, no. 1–2, pp. 284–293, 2004.

[236] H. Cui, I. B. Bhat, S. P. Murarka, H. Lu, W.-J. Hsia, and W. Catabay, “Copper drift in methyl-doped silicon oxide film,” *J. Vac. Sci. Technol. B Microelectron. Nanom. Struct.*, vol. 20, no. 5, p. 1987, 2002.

[237] A. L. S. Loke, C. Ryu, C. P. Yue, J. S. H. Cho, and S. S. Wong, “Kinetics of copper drift in PECVD dielectrics,” *IEEE Electron Device Lett.*, vol. 17, no. 12, pp. 549–551, 1996.

[238] D. H. Shacham-Diamand, Y.Dedhia and W. G. Oldham, “Copper Transport in Thermal SiO2,” *J. Electrochem. Soc. 1993 Vol. 140, issue 8,* vol. 140, no. 8, pp. 5–10, 1993.

[239] E. H. Nicollian and J. R. Brews, “Metal Oxide Semiconductor (MOS) Physics and Technology,” *Wiley, New York, 1982.*, 1982.

[240] A. Kuzmin, A. Anspoks, A. Kalinko, J. Timoshenko, and R. Kalendarev, “X-ray absorption spectroscopy of Cu-doped WO3 films for use in electrochemical metallization cell memory,” *J. Non. Cryst. Solids*, vol. 401, pp. 87–91, 2014.

[241] L. Chen *et al.*, “Amorphous copper tungsten oxide with tunable band gaps,” *J. Appl. Phys.*, vol. 108, no. 4, 2010.

[242] F. Mehmood, J. Iqbal, A. Gul, W. Ahmed, and M. Ismail, “Facile synthesis of 2-D Cu doped WO3 nanoplates with structural, optical and differential anti cancer characteristics,” *Phys. E Low-Dimensional Syst. Nanostructures*, vol. 88, no. December 2016, pp. 188–193, 2017.

[243] X. Bai, H. Ji, P. Gao, Y. Zhang, and X. Sun, “Morphology, phase structure and acetone sensitive properties of copper-doped tungsten oxide sensors,” *Sensors Actuators, B Chem.*, vol. 193, pp. 100–106, 2014.

[244] R. Sivakumar, R. Gopalakrishnan, M. Jayachandran, and C. Sanjeeviraja, “Preparation and characterization of electron beam evaporated WO3 thin films,” *Opt. Mater. (Amst).*, vol. 29, no. 6, pp. 679–687, 2007.

[245] B. W. Faughnan, R. S. Crandall, and P. M. Heyman, “Electrochromism in WO3 amorphous films,” *R.C.A. Rev.*, vol. 36, pp. 177–197, 1975.

[246] S. Hashimoto and H. Matsuoka, “Mechanism of electrochromism for amorphous WO3 thin films,” *J. Appl. Phys.*, vol. 69, no. 2, pp. 933–937, 1991.

[247] K. Sankaran *et al.*, “Modeling of Copper Diffusion in Amorphous Aluminum Oxide in CBRAM Memory Stack,” *ECS Trans.*, vol. 45, no. 3, pp. 317–330, 2012.

[248] J. A. Dawson and J. Robertson, “Nature of Cu interstitials in Al2O3 and the implications for filament formation in conductive bridge random access memory devices,” *J. Phys. Chem. C*, vol. 120, no. 27, pp. 14474–14483, 2016.

[249] K. N. Subedi, K. Prasai, M. N. Kozicki, and D. A. Drabold, “Structural origins of electronic conduction in amorphous copper-doped alumina,” *Phys. Rev. Mater.*, vol. 3, no. 6, pp. 1–9, 2019.

[250] D. Jana *et al.*, “Conductive-bridging random access memory: challenges and opportunity for 3D architecture,” *Nanoscale Res. Lett.*, vol. 10, no. 1, 2015.

[251] N. Onofrio, D. Guzman, and A. Strachan, “Atomic origin of ultrafast resistance switching in nanoscale electrometallization cells,” *Nat. Mater.*, vol. 14, no. 4, pp. 440–446, 2015.

[252] C. S. Hsu, H. Y. Hsieh, and J. S. Fang, “Enhancement of oxidation resistance and electrical properties of indium-doped copper thin films,” *J. Electron. Mater.*, vol. 37, no. 6, pp. 852–859, 2008.

[253] B. K. Meyer *et al.*, “Binary copper oxide semiconductors: From materials towards devices,” *Phys. Status Solidi Basic Res.*, vol. 249, no. 8, pp. 1487–1509, 2012.

[254] N. Chamele, “private communication.” 2020.

[255] A. P. Young and C. M. Schwartz, “Electrical conductivity and thermoelectric power of Cu2O,” *J. Phys. Chem. Solids*, vol. 30, no. 2, pp. 249–252, Feb. 1969.

[256] D. S. Murali, S. Kumar, R. J. Choudhary, A. D. Wadikar, M. K. Jain, and A. Subrahmanyam, “Synthesis of Cu2O from CuO thin films: Optical and electrical properties,” *AIP Adv.*, vol. 5, no. 4, pp. 1–6, 2015.

[257] D. Kudryashov, A. Gudovskikh, K. Zelentsov, A. Mozharov, A. Babichev, and A. Filimonov, "The temperature dependence of the electrical conductivity in Cu2O thin films grown by magnetron sputtering," *J. Phys. Conf. Ser.*, vol. 741, no. 1, pp. 1–5, 2016.

[258] S. Yazdanparast, J. A. Koza, and J. A. Switzer, "Copper Nanofilament Formation during Unipolar Resistance Switching of Electrodeposited Cuprous Oxide," *Chem. Mater.*, vol. 27, no. 17, pp. 5974–5981, 2015.

[259] M. O'Keeffe and W. J. Moore, "Electrical Conductivity of Monocrystalline Cuprous Oxide," *J. Chem. Phys.*, vol. 35, no. 4, p. 1324, 1961.

[260] M. G. Hutchins, O. Abu-Alkhair, M. M. El-Nahass, and K. Abdel-Hady, "Electrical conductivity and dielectric relaxation in non-crystalline films of tungsten trioxide," *J. Non. Cryst. Solids*, vol. 353, no. 44–46, pp. 4137–4142, 2007.

[261] S. K. Ganapathi, D. M. Owen, and A. H. Chokshi, "The Kinetics of Grain Growth In Nanocrystalline Copper," *Scr. Metall. Mater.*, vol. 25, no. c, pp. 2–5, 1991.

[262] S. Simoes, R. Calinas, M. T. Vieira, M. F. Vieira, and P. J. Ferreira, "In situ TEM study of grain growth in nanocrystalline copper thin films," *Nanotechnology*, vol. 21, no. 14, 2010.

[263] S.-K. Lee, H.-C. Hsu, and W.-H. Tuan, "Oxidation Behavior of Copper at a Temperature below 300 °C and the Methodology for Passivation," *Mater. Res.*, vol. 19, no. 1, pp. 51–56, 2016.

[264] S. Rehman, J. H. Hur, and D. K. Kim, "Resistive Switching in Solution-Processed Copper Oxide (CuxO) by Stoichiometry Tuning," *J. Phys. Chem. C*, vol. 122, no. 20, pp. 11076–11085, 2018.

[265] S. Yu and H. S. P. Wong, "Modeling the switching dynamics of Programmable-Metallization-Cell (PMC) memory and its application as synapse device for a neuromorphic computation system," *Tech. Dig. - Int. Electron Devices Meet. IEDM*, no. 6, pp. 22.1.1-22.1.4, 2010.

[266] S. S. Hwang, S. Y. Jung, and Y. C. Joo, "The electric field dependence of Cu migration induced dielectric failure in interlayer dielectric for integrated circuits," *J. Appl. Phys.*, vol. 101, no. 7, 2007.

APPENDIX A

IMAGEJ SCRIPT FOR PARTICLE SIZE ANALYSIS OF AFM IMAGES

```
// SET SCALE FIRST
run("Duplicate...", " ");
setBatchMode(true);
run("Convolve...", "text1=[-1 -1 -1 -1 -1\n-1 -1 -1 -1 -1\n-1 -1 25 -1 -1\n-1 -1 -1 -1 -1\n-1
-1 -1 -1 -1\n] normalize");
// filter coefficient is mostly 25, 30 for sample 23
run("Enhance Contrast", "saturated=0.3")
run("8-bit");
run("Smooth");
run("Auto Local Threshold", "method=Mean radius=15 parameter_1=0 parameter_2=0
white");
// radius can be 26 or 30; 15 for sample 5
run("Median...", "radius=2");
run("Median...", "radius=2");
run("Median...", "radius=2");
//run("Median...", "radius=2");
//run("Median...", "radius=2");
//The number of median filters used depends on how good the
// post-processed image is.
run("Analyze Particles...", "size=500-Infinity display exclude clear add");
run("Summarize");
MeanArea=getResult("Area",nResults-4);
MeanDiameter=sqrt(MeanArea*4/PI);
print("Average grain area is " + MeanArea + "nm2");
print("Assuming circular grain, then");
print("Average grain size is " + MeanDiameter + " nm.");
```

APPENDIX B

MATLAB CODE OF OXIDATION AND DIFFUSION MODEL FOR Cu-WO_3 SYSTEM

```
function CuWO3(deposited,temp,time,WO3th,pO2)
%% If no pO2 input
if ~exist('pO2','var')
    pO2=760*0.21;
end
%% If no WO3 thickness input
if ~exist('WO3th','var')
    WO3th=80;
end
%% Initiate variables
EaWO3=0.742; %0.742
D0=2.7333e-6;
R=8.617e-5;
Eacuox=0.697; %Activation energy of Cu in Cu20
k0=20.6972;
p0=760*0.21;
NAvog=6.022e23; %atoms/mole
CuDens=8.85; %g/cm3
CuMolMass=63.5; %g/mole
Cu2oDens=6; %g/cm3
Cu2oMolMass=143.0; %g/mole
CuConv=NAvog*CuDens/CuMolMass;
Cu2oConv=NAvog*Cu2oDens/Cu2oMolMass;
CuSSwo3=0.56;
annT=273+temp; % conversion to Kelvin
t=time*60; % annealing time in seconds
y=deposited*1e-7; % conversion to cm
k=k0*(pO2/p0)^0.5*exp(-Eacuox/R/annT);
D=D0*exp(-EaWO3/R/annT);
doxfinal=k*sqrt(t); %parabolic law
doxnm=doxfinal*1e7; %CuOx thickness in nm if no diffusion
xx=0:1e-7:(deposited+WO3th)*1e-7;
n=1;
C=ones(1,length(xx)).*CuConv;
C(deposited+1:length(xx))=0;
C1=ones(1,length(xx));
C1(deposited+1:length(xx))=0;
CuinCu2o=0.67; %Cu at% in Cu2O
flag=0;
%% If time is zero
if time<=0
        plot(xx,C,'LineWidth',6)
        return
end
%% Start time for Diffusion and Oxidation
for tt=1:time
    if tt<=1
        dox=k*sqrt(tt*60);
        doxnmm=dox*1e7;
        usedCu=dox/1.65;
        z=round(doxnmm);
        zz=round(usedCu*1e7);
        for x=0:1e-7:xx(length(xx))
            if x<=usedCu
                C(n)=CuinCu2o*Cu2oConv;
                C1(n)=CuinCu2o;
                n=n+1;
```

```
            end
            if x>usedCu && x<y
                C(n)=1*CuConv;
                C1(n)=1;
                n=n+1;
            end
            if x>usedCu && x>=y
                C1(n)=CuSSwo3*(1-erf((x-y)/sqrt(4*D*tt*60)));
                C(n)=CuSSwo3*CuConv*(1-erf((x-y)/sqrt(4*D*tt*60)));
                n=n+1;
            end
        end
        diffused=round(sum(C1(deposited+1:length(C1))));
        C1(1:diffused+zz+1)=0;
        if diffused+zz+1-z<1
            mm=0-(diffused+zz+1-z);
            C1(1:z-mm)=CuinCu2o;
            C(1:z-mm)=CuinCu2o*Cu2oConv;
        else
            C1(diffused+zz+1-z:diffused+zz+1)=CuinCu2o;
            C(diffused+zz+1-z:diffused+zz+1)=CuinCu2o*Cu2oConv;
            if z<deposited && diffused+zz-z>0
                C1(1:diffused+zz-z)=0;
                C(1:diffused+zz-z)=1;
            end

        end
    else
        if C1(deposited)==CuinCu2o
            if flag==0
                %Q1=diffused*1e-7*CuConv
                Q=((deposited*1e-7)-usedCu)*CuConv
                diffCu=((deposited*1e-7)-usedCu)*1e7;
                tt;
                oxiCu=usedCu*1e7;
                CuConcEq=Q/WO3th/1e-7;
                ttime=tt*60;
                flag=1;
            end
            for v=deposited+1:length(xx)
            r=v*1e-7;
            C(v)=Q/sqrt(pi*D*tt*60)*exp(-r^2/(4*D*tt*60));
            end
        else
            dox=k*sqrt(tt*60);
            doxnmm=dox*1e7;
            usedCu=dox/1.65;
            z=round(doxnmm);
            zz=round(usedCu*1e7);
            for x=0:1e-7:xx(length(xx))
                if x<=usedCu
                    C1(n)=CuinCu2o;
                    C(n)=CuinCu2o*Cu2oConv;
                    n=n+1;
                end
                if x>usedCu && x<y
                    C1(n)=1;
```

```
                    C(n)=1*CuConv;
                    n=n+1;
                end
                if x>usedCu && x>=y
                    C1(n)=CuSSwo3*(1-erf((x-y)/sqrt(4*D*tt*60)));
                    C(n)=CuSSwo3*CuConv*(1-erf((x-y)/sqrt(4*D*tt*60)));
                    n=n+1;
                end
            end
        diffused=round(sum(C1(deposited+1:length(C1))));
        C1(1:diffused+zz+1)=0;
        if diffused+zz+1-z<1
            mm=0-(diffused+zz+1-z);
            C1(1:z-mm)=CuinCu2o;
            C(1:z-mm)=CuinCu2o*Cu2oConv;
        else
            C1(diffused+zz+1-z:diffused+zz+1)=CuinCu2o;
            C(diffused+zz+1-z:diffused+zz+1)=CuinCu2o*Cu2oConv;
            if z<deposited && diffused+zz-z>0
                C1(1:diffused+zz-z)=0;
                C(1:diffused+zz-z)=1;
            end

        end
        end
    end
    n=1;
    semilogy(xx,C,'LineWidth',6)
    axis([0 (deposited+WO3th)*1e-7 1e20 1e23])
    set(gca,'FontSize',16)
    xlabel('Depth (cm)','FontSize',16)
    ylabel('Cu concentration (atoms/cm^3)','FontSize',16)
    title('Depth Profile of Cu (atoms/cm^3)','FontSize',16)
    box=annotation('textbox', [0.6, 0.7, 0.3, 0.2], 'String', "Cu_2O is
" + doxnmm + " nm       Time elapsed: "+ tt + " min");
    box.FontSize = 16;
    M(tt)=getframe;
    hold off
    delete(findall(gcf,'type','annotation'))
end
%% Movie plot of the concentration
if time>0
    movie(M,1,5)
end
%% Interactive Cu Concentration Plot
CuConcAtWO3Surface=C(deposited+1);
semilogy(xx,C,'LineWidth',6)
axis([0 (deposited+WO3th)*1e-7 1e20 1e23])
set(gca,'FontSize',16)
xlabel('Depth (cm)','FontSize',16)
ylabel('Cu concentration (atoms/cm^3)','FontSize',16)
title('Depth Profile of Cu (atoms/cm^3)','FontSize',16)
title('Depth Profile of Cu (atoms/cm^3)','FontSize',16)
box=annotation('textbox', [0.6, 0.7, 0.3, 0.2], 'String', "Cu_2O is " +
doxnmm + " nm       Time elapsed: "+ tt + " min");
box.FontSize = 16;
end
```

APPENDIX C

MATLAB CODE OF LATERAL PMC DEVICE SIMULATION

```
function play(number,L,V,Ni)
if ~exist('V','var')
    V=60; %applied bias
end
if ~exist('Ni','var')
   Ni=5.5e21; %cation concentration
end
if ~exist('L','var')
   L=14e-4; %channel length
end
E0=0.6;
D=1e-12;
CuDens=8.85;
NAvog=6.022e23;
CuMolMass=63.5;
Nf=NAvog*CuDens/CuMolMass;
a=1.12e-7; %2.4e-7
v=1e12;
uth=2.8e4;
kT=0.0259;
z=2;
q=1.6e-19;
We=50e-4;
tox=80e-7;
Aox=tox*We;
resCu=1.7e-6;
resox=3e7;
resSemi=10e4;
tSemi=8e-7;
Dfil=50e-7;
Afil=pi*Dfil*Dfil/4;
tt=0:1:3e4;
dh=1e-7;
h=0:dh:L;
Start=Ni*Aox*L*1.25;
Cmin=1e18;
%resox*(L)/Aox
if number==1
    f=1;
    for ii=1:L/dh
        cons(ii)=1/2*Dfil*We/1*h(ii)*1*Nf;
        x0(ii)=cons(ii)/(Ni-Cmin)/Aox;
        if x0(ii)+h(ii)<=L
            min(ii)=Cmin*Aox*x0(ii);
            added(ii)=cons(ii);
            left(ii)=Ni*Aox*1.2*(L-h(ii)-x0(ii))-cons(ii);
            x0f=x0(ii);
        else
            x0(ii)=x0f-f*dh;
            min(ii)=Cmin*Aox*x0(ii);
            added(ii)=cons(ii);
            left(ii)=Ni*Aox*1.2*(L-h(ii)-x0(ii))-cons(ii);
            f=f+1;
        end
        if left(ii)>cons(ii)
            tot(ii)=left(ii)+min(ii);
            meh=left(ii);
```

```
        else
            tot(ii)=added(ii)+min(ii);
        end
        Nif(ii)=tot(ii)/Aox/(L)/1.2;
    end
    for n=1:L/dh
        rate(n)=(2*Nif(n)*uth/Nf*exp(-E0/kT))*sinh((a*z*V/2/kT)/(L-
h(n)));
        invrate(n)=1/rate(n);
        ts(n)=invrate(n)*dh;
    end
    time(1)=ts(1);
    for i=2:length(ts)
        time(i)=ts(i)+time(i-1);
    end
    for n=1:L/dh
        Jmg(n)=2*z*Nif(n)*q*uth*exp(-E0/kT)*sinh((a*z*V/2/kT)/(L-
h(n)));
        Img(n)=Jmg(n)*Aox;
        Rion(n)=resCu*h(n)/Afil+resox/(time(n)^0.8)*(L-h(n))/Aox;
        Iion(n)=V/Rion(n);%/Aox;
        Isemi(n)=1/resSemi*V/(L-h(n))*tSemi*We;
        Iint(n)=1/(resox/time(n)^0.8)*V/(L-h(n))*Aox;
        Itot(n)=Isemi(n)+Img(n)+Iint(n);
    end
    semilogy(time,Jmg*Aox,'LineWidth',2)
    hold on
    semilogy(time,Isemi,'LineWidth',2)
    hold on
    semilogy(time,Iint,'LineWidth',2)
    hold on
    semilogy(time,Itot,'LineWidth',2)
    %plot(x0*1e4,h(1:length(h)-1)*1e4,'LineWidth',2)
    %hold on
    %plot(time,x0(1:length(x0)-1))
    %plot(time,h(1:length(h)-1)*1e4)
    %semilogy(h(1:length(h)-1)*1e4,cons,'LineWidth',2)
    %hold on
    %semilogy(h(1:length(h)-1)*1e4,left,'LineWidth',2)
    %hold on
    %semilogy(h(1:length(h)-1)*1e4,tot,'LineWidth',2)
    %semilogy(h(1:length(h)-1)*1e4,Nif,'LineWidth',2)
    %semilogy(time,Nif,'LineWidth',2)
    t=sum(ts)
    set(gca,'FontSize',18)
    set(gca, 'FontName', 'Times New Roman')
    set(gca,'fontweight','bold')
    ylabel('I (A)')
    xlabel('Time (s)')
    ylim([0 1e-4])
end
```